



**Università degli Studi di Roma
"Tor Vergata"**

XXIV Cycle- Geoinformation Doctorate

**WEARABLE AND IMPLANTABLE
RFID TECHNOLOGY
FOR
PERVASIVE HEALTHCARE:**

*Human
Identification
and Sensing*



Cecilia Occhiuzzi

December 2011

Universita' di Roma "Tor Vergata"

School of Engineering

DISP. Dipartimento di Informatica, Sistemi e
Produzione

XXIV-Cycle Geoinformation Doctorate



WEARABLE AND IMPLANTABLE RFID
TECHNOLOGY FOR PERVASIVE
HEALTHCARE:

Human Identification and Sensing

CECILIA OCCHIUZZI

ADVISOR: Prof. Gaetano Marrocco

COORDINATOR: Prof. Domenico Solimini

ROME December 2011

To my Family

to Mirco

SUMMARY

Among the several challenges that the OECD (Organization for Economic Co-operation and Development) countries are asked to face in the next future, Health is surely a priority. The demographic development, the progressive increase of the percentage of elderly people, the growth of chronic degenerative diseases following the current lifestyles (smoking, obesity, and inactivity) contribute toward the need of innovative healthcare solutions, based on decentralized, pervasive and patient-centric approaches. Engineering and Medical technologies have the opportunity to share expertise and efforts to effectively realize the concept of *Pervasive Healthcare*, a multidisciplinary system where environment, persons, their internal organs and even their implanted medical devices are continuously and remotely monitored in order to have every time and everywhere information about their condition and state. Typical scenarios include implantable, wearable and hand-held devices able to sense one or more vital signs and transmit alert messages to hospital, ambulance and healthcare providers for getting emergency services. The main challenge is to design and develop reliable yet non-intrusive sensors, as well as robust and highly efficient wireless communication infrastructures.

Promising solutions could come from the new progresses of Radio Frequency Identification (RFID) passive technology. Together with its ID code widely used for logistics, an RFID tag is in fact able to carry information about the tagged object such as its physical state and its evolution along with time, without any specific embedded sensor, thus realizing an innovative paradigm of short-range sensing. Furthermore RFID tag can be equipped with a large variety of passive sensors, such as discrete mechanical components or distributed chemical materials, able to affect the reader-tag communications and thus perform the sensing activity without any local power supply. This kind of “transparent” and non-intrusive devices could offer great advantages in pervasive

healthcare: one or more battery-less RFID sensor tag could be permanently integrated into everyday objects, clothes or into implanted medical devices such to monitor the subject from two different perspectives, from *outside* and from *inside*. In both approaches the data transmitted by each sensor-tag can be processed individually or together with those from the other distributed nodes in order to extract information in the most comprehensive way.

The application of the RFID technology to the Pervasive Healthcare is a rather new topic. The subject of this Ph.D thesis deals with the study of its feasibility through of a multidisciplinary vision, which merges together Electromagnetics, Wireless Communication, Electronics, Sensors as well as Anatomy and Physio-pathology.

PHYSICAL RATIONALE AND THEORETICAL INVESTIGATIONS

The first part of the thesis will be devoted to the detailed analysis of the issues related to the wireless monitoring of human subjects, the requirements, the challenges, the available solutions and the possible improvements given by the RFID technology. To address this last issue, a realistic vision of pervasive RFID healthcare will be presented by means of true applications and real scenarios. The basic sensing mechanisms and paradigms achievable by low-cost, passive, RFID sensor devices will be then described, by analyzing with a deep theoretical approach the physics of the phenomena up to introduce and investigate two sensing strategies: the *sensor-less* sensing and the *loaded-tag* sensing. General guidelines will be proposed to assist the design of process-specific sensor-less and loaded tags, with the aim to control, enhance and optimize both sensing and communication performances.

SENSING FROM OUTSIDE

The second part of the thesis is focused on the identification and monitoring of people *from outside*, e.g. all the information

achievable by means of sensors opportunely placed onto the human body or in the surrounding environment.

At this purpose a wearable RFID tag, suitable to be embedded into clothes and garments and to host passive sensors, is described, fabricated and experimentally characterized in real scenario. As in more mature active bodycentric systems, interesting RFID communication modalities can involve *on-body* and *off-body* links. The off-body communication could be useful for example to locate and monitor people inside buildings by means of fixed readers placed in different rooms or by a wearable reader and ambient-disseminated tags. A possible application is the access control in dangerous or restricted areas. The on-body communication is instead typical of unusual scenarios where a fixed communication infrastructure is missing. It could be the case of a sportsman, a soldier or a fireman equipped with different RFID sensors (inside his garment) interrogated by his hand-held standard communicator in harsh environments.

One of the most important parameters to be monitored is the human activity. Unexpected falls, inactivity or hyperactivity, movements during sleep, breath rhythm and posture can be, for example, easily related to physiological and pathological conditions and give essential information about the state of the subject. At this purpose two different strategies will be introduced, discussed and experimentally tested. The first one consist in using passive accelerometers properly integrated into the wearable tag, while the second one requires a proper processing of the power backscattered by the tag toward the reader, thus without specific sensors.

Strictly related to the human activity is then the possibility to monitor deformations and variations of shape (for example elongation and contraction) of muscles or body segments, during movements and breaths. The field of application are countless, from the sport to the rehabilitation and the monitoring of physical activity for patients who have suffered a stroke, multiple sclerosis, joint replacements, or reconstructions, amputation, brain, and spinal cord injury, or some motor function disability resulting from Parkinson's disease. A preliminary passive strain sensor is presented, suitable to be used also in civil applications such as the structural monitoring of buildings and vehicles.

For fulfilling the vision of an efficient pervasive healthcare system, the environmental variables, such as temperature, humidity and air quality, must be also taken into account in both usual and unusual scenario. Three kinds of passive sensors will be thus introduced: a temperature sensor integrating shape memory alloy materials, a humidity sensor integrating sensitive polymers and a gas sensor integrating carbon nanotubes. Each device will be described from a theoretical and an experimental point of view, demonstrating the possibility to fully master their response and their effectiveness. The proposed devices can be distributed within the environment as well as worn by the subject, for example to monitor the environmental conditions in hazardous and extreme situations, like during Firemen's activity.

SENSING FROM INSIDE

The third part of the work is devoted to a much more challenging and ambitious topic: the monitoring *from inside*, e.g. all the information achievable by means of sensors opportunely placed into the human body.

A strategic role in the present and future healthcare will be in charge of implanted medical devices. Their widespread diffusion and their importance in restoring physiological functions and, definitely, in saving lives, actually prompt the need of a continuous monitoring of their functionality and their effectiveness. Such an observation could be useful to the clinicians to evaluate the effectiveness of their action and accordingly to update the medical treatment, or more drastically to prevent severe drawbacks for the patients in case of complications and failure. Some partial solutions have been proposed just in the very last years but they are generally subjected to the presence of complex electronics components: one or more active sensors, power supply, transceiver and antenna. The resulting devices are not completely bio-compatible, may suffer from local failure and, not least, they provide limited lifetime or need power recharge. All these limitations leave the problem unsolved. According to the mentioned constraints, the sensor-less approach could be considered: one or more battery-less RFID IC could be integrated into implanted medical devices

provided with conductive elements (prosthesis, sutures, stents or orthopedic fixings) such to transform them into RFID radio-sensors suitable to be interrogated by an external reader and able to “sense” themselves and the close surrounding environment. By data acquisition at different times, it will be possible to collect the history of geometrical or chemical features of tissues and devices, thus observing in an indirect way the functioning, the healing process and possible complications.

Starting from suggestions and opinions of medical doctors and surgeons, a feasibility study has been carried on, pointing out all the possibilities and the limitations of the proposed technology. The physical rationale of this approach, for which the RFID tag acts as a self-sensing device, lies in the dependence of the tag’s input impedance and of its radar cross section on the physical and geometrical features of the labeled object or, more in general, of the close surrounding environment. When the object where the tag is attached on undergoes changes in time (many physiologic and pathological biological processes involve variations of the dielectric properties of the tissues), the tag’s electrical features accordingly change, and these variations can be remotely detected by the RFID reader.

The dissertation makes use of numerical electromagnetic simulations to study some realistic pathological processes, such as liver cancer and brain edema evolution, corroborated by preliminary laboratory experiments with a tag prototype placed inside a liquid body phantom and subjected to a controlled local permittivity variation.

Particular attention is devoted to the very hot topic of the wireless monitoring of the status of a vascular duct. In particular, it will be investigated the feasibility of transforming an implanted medical device, e.g. a vascular stent, into a radio-sensor equipped with an RFID IC and able to sense and communicate its status and the conditions of the vessel after the implant. The promise of such a device is an easy and non-invasive monitoring of the human vessels, useful for regular follow-up and early alerts of possible complications. A first realistic proof of concept of the idea has been fabricated and tested by means of electromagnetic

liquid phantoms able to emulate the human neck's tissues and the variations connected with the restenosis process.

CONTENTS

1	PERVASIVE HEALTHCARE	1
1.1	What	2
1.1.1	Possible operative scenarios	3
1.2	How	7
1.3	RFID Approach	9
2	RFID TECHNOLOGY AND SENSING PARADIGMS	13
2.1	RFID-Sensing Equations	14
2.1.1	Sensing Metrics	16
2.2	Sensing Paradigms	19
2.2.1	Sensor- less Tag	19
2.2.2	Loaded Tag	20
2.3	Optimization strategies	21
2.3.1	Method	22
2.4	Engineering the data inversion curves	27
2.5	Numerical study	30
2.5.1	Low dielectric process	30
2.5.2	High dielectric process	31
I	SENSING FROM OUTSIDE	39
3	REQUIREMENTS AND FEASIBILITY: A CLINICAL CASE	41
3.1	System Analysis	43
3.1.1	The Restless sleep key-parameters	44
3.1.2	Tag sensitivity and useful read region	45
3.1.3	Timing	47
3.2	Communication performances in real configurations	47
3.3	Estimated Biophysical signals by using a radio-mechanical model	49
3.4	Conclusion	54
4	RFID WEARABLE TAG AND BODY CENTRIC COMMUNICATION	57
4.1	Antenna Layout and Design Procedures	59
4.1.1	Circuit model	61

4.1.2	Parametric Analysis	64
4.2	Prototypes and performances in real configurations	65
4.2.1	PTFE tags	68
4.2.2	Flexible tags	74
4.3	Bodycentric Communication	77
4.3.1	Off-body communications	77
4.3.2	On-body communications	84
4.3.3	Safety Issue	89
4.4	Conclusion	91
5	MONITORING OF BODY ACTIVITY: MOTION AND DEFORMATION	93
5.1	Monitoring of Motion by means of loaded tag	95
5.1.1	Omnidirectional motion sensor	95
5.1.2	RFID Motion Sensor prototype	97
5.1.3	Experimentation and Results	98
5.2	Monitoring of activity by means of sensor-less approach	100
5.3	Monitoring of Deformation	105
5.3.1	Mechanical model	105
5.3.2	Electromagnetic model	106
5.3.3	Design Metodology	109
5.3.4	An Experimental Example	113
5.4	Conclusion	115
6	MONITORING OF THE ENVIRONMENT: TEMPERATURE THRESHOLD	119
6.1	The Nitinol Thermal Switch	122
6.1.1	Switch geometry	122
6.1.2	Prototype and characterization	123
6.2	Two-chip Tag antenna design	125
6.3	Prototype	128
6.4	thermal characterization of the tag	130
6.5	Conclusions	132
7	MONITORING OF THE ENVIRONMENT: QUALITY OF THE AIR	135
7.1	Humidity Sensor	139
7.1.1	Prototype and Characterization	142
7.1.2	Operative characterization	146

7.1.3	Cyclic Exposure	150
7.2	Gas Sensor	155
7.2.1	SWCNT Material Preparation and Characterization	155
7.2.2	RFID Gas Sensor: design and prototype	160
7.2.3	Sensing Characterization	167
7.3	Conclusions	174
II SENSING FROM INSIDE 177		
8	REQUIREMENTS AND FEASIBILITY	179
8.1	Case Study: Liver Cancer and Brain Edema	181
8.1.1	Liver Cancer Monitoring	182
8.1.2	Brain Edema Monitoring	186
8.2	Experiments with Liquid Body Phantom	193
8.3	Conclusions	195
9	CASE STUDY: THE STENTAG	199
9.1	Design Procedures	200
9.2	Prototypes and experimentation	205
9.3	Conclusions	212
10	CONCLUSIONS AND FUTURE PERSPECTIVES	213
Bibliography 217		
Publications 233		
Acknowledgments 237		

PERVASIVE HEALTHCARE

Pervasive Healthcare can be defined as the possibility to provide healthcare to anyone, anytime and everywhere. It is a natural application of the emerging concepts of pervasive and ubiquitous computing, whose primary aim and vision are the possibility of making technology transparent and embedded in everyday life, such to create small smart objects, robustly networked and co-operant with smart ambients and contexts. In the last 20 years many researchers tried to define operative scenarios and technological objectives, facing common issues as how to provide better healthcare services to an increasing number of people by using limited financial and human resources or how to reduce informational errors such to allow rapid and effective access to treatment and care services or finally how to personalize the medical practice such to assist each patient in the most appropriate place and by the most appropriate actions. Although the technology is nowadays available, the main limitation of the proposed solutions remains the lack of a widespread diffusion, mainly due to their cost, their complexity and last but not least their complete absence of transparency.

From an operative perspective, it is possible to define different meanings of pervasive healthcare, from the health monitoring in usual and unusual scenario, to the telemedicine and the intelligent emergency management systems. Each particular declination of the main concept adds or reduces requirements to the system, in each case the subject becomes an hub of primary acquisition of information from himself and the surrounding environment [1].

Generally, a pervasive healthcare system involves multiple sensor nodes able to sense clinical and behavioral parameters of the patients, as well as the most significant environmental ones; such nodes can be fixed or portable, placed off the body, e.g. disseminated in the surrounding environment, or worn by the subject, e.g. embedded in clothes and garments [2]. Each node comprise one or more cooperant sensors, a power supply, a DSP and a radio front-end to wireless transmit the recorded data. Emerging solutions envisages also implantable nodes, such as biocompatible devices able to monitor “from inside” the state of the subjects and of its prosthesis and other medical implants.

The nodes can communicate with each other such to form a network, which can be defined, according to its location and size, Body Area Network (BAN), Personal Area Network (PAN) and Local Area Network (LAN). Several solutions have been proposed for the communication within BAN and PAN, since they involve distances less than 1m, Bluetooth and ZigBee are two of the mostly-used standards. Finally, the bidirectional communication to/from the medical server can be achieved by conventional communication infrastructures, e.g. Internet, mobile telephone or even satellite solutions.

1.1 WHAT

Despite the thousand of different applications and solutions envisaged or experimented in the last years, the common denominator of each pervasive healthcare system is a decentralized and patient-centric approach, resulting in a redefinition of the most important welfare paradigms. Oppositely to typical hospital and clinical procedures, pervasive healthcare technologies tend to support continuous treatment and care of people rather than focus on technologies for acute events. This first concept necessary lives with the aim to move the assistance from the hospital to the home or the workplace. The environment, instead of the clinician, is invested with the responsibility of continuously “sampling” the state of the patients by means of specific and non specific devices: the diagnosis becomes preventive and the early detection one of its most important features [3].

There are a number of personal and environmental parameters to monitor in order to realize an efficient body-centric systems. A first group involves the basic vital signs, e.g. blood pressure, pulse rate, blood glucose level, electrocardiograph patterns, respiration rate, oxygen saturations and temperature; they are direct indicator of the health state of the subject and are generally monitored by means of active sensors opportunely placed in specific positions on the body. To improve the “transparency” of such sensors, often they are grouped together such to have multi-parameter sensing devices. e.g. bracelets, smart T-shirt, whose thresholds, sensitivities and interrogation rates can be set according to the individual characteristics of the subject [2].

In addition to vital signs other behavioral parameters can give information about the state of the patients; e.g. the activity rate, the ambient temperature and the quality of the air. The activity is a clear indicator of the wellness of the person: accidental falls or fainting may results in absence of movements for long periods and their early detection can give rise to proper and rapid rescue activities. The environmental temperature, as well as the quality of the air, gives instead information about the context of the patients. They are particularly important when the subject to be monitored resides in hazardous environment, e.g. a fireman or a factory worker, or when physical and mental pathologies corrupt the subject’s capabilities of discerning and solve common dangerous situations, e.g ingestion of perished food or uncontrolled gas leakage.

Context and personal data, together with historical records must be finally fused to lead a complete and efficient pervasive healthcare system (Fig.1).

1.1.1 *Possible operative scenarios*

In pervasive healthcare vision, the patient is a central hub of primary data acquisition and elaboration. Following, some usual and unusual operative scenarios are described, such to underline the most important key issues, e.g. the monitoring strategies, the parameter to be sensed and the communication network.

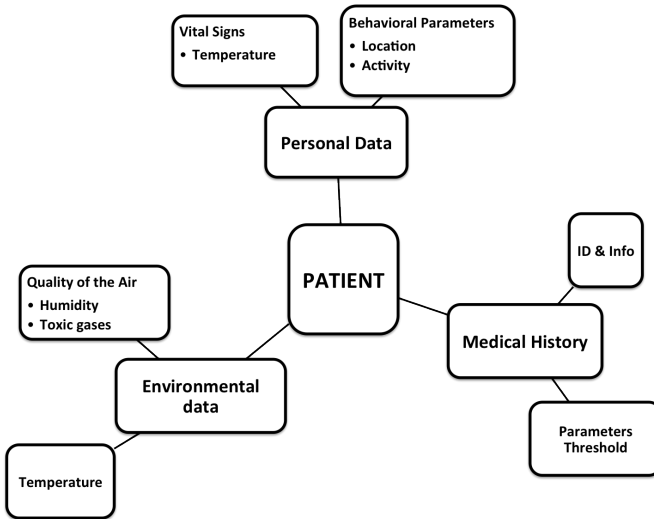


Figure 1: Pervasive Healthcare: patient's and context's parameters

1. Fireman and Soldier: There is a severe need of a wearable system able to monitor the activity and the state of firemen and soldiers during their activity in harsh environment. The wearable/implantable sensing system should be able to continuously record ambient, body and physiological indicators and transfer this information wirelessly to a central unit. Such a monitoring must be performed without limiting the performance of the subject or adding weight to his gear. The most sensitive parameters to be monitored could be grouped in four categories: physical (vital signs and activity), physiological (stress conditions), environmental (temperature and quality of the air) and for localization (where the subject is and with who) (Fig. 2). The primary hub of data acquisition could be their radio-communicator.
1. Elderly people, Children and Disabled subjects. It is necessary to have a system able to monitor elderly, disabled and young people in their daily life, such to support them and

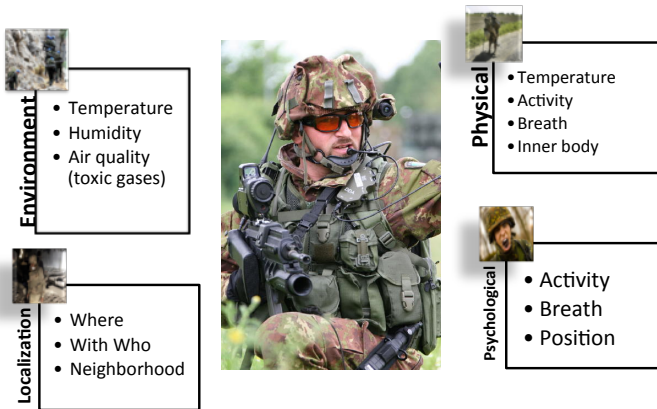


Figure 2: Pervasive Healthcare: patient's and context's parameters

provide quick help if necessary. At a first level the most important parameters to monitor are the activity and the quality of the air: the subject could be fallen or confused and be in danger if he doesn't receive adequate help, for example because he left the gas pipe open. The monitoring system should be completely user-transparent and embedded in the home's infrastructure. More sophisticated sensing platform could involve the record and the recognition of specific pattern of daily movements, e.g cooking, eating, bathing and taking medicine.

2. Domiciliary Diagnosis and Follow up: The diagnosis of some pathologies, e.g sleep disorders, alimentary diseases and neuromuscular disabilities, are sensibly affected by the way they are performed. The use of invasive equipment and the necessity to refer to high specialized diagnostic centers, could in fact alter the normal predisposition of the patients, leading to a not accurate analysis. The problem is even more challenging in case of children. The possibility to benefits of portable and wearable devices could sensibly improve the quality of the medical assistance, furthermore reducing costs and waiting lists. The monitoring system must be high

personalized and easy to use. If the monitoring period is long, e.g. days or weeks, it is necessary to have an extremely efficient platform for the transmission of the data, as well as an efficient system for power supplying to wearable and portable devices.

3. Access control and Safety: Many scenarios necessitate of systems able to perform access control, e.g. the monitoring of people present in a restricted area and in what circumstances. This actions could have different purposes, from the protection of sensitive and valuable informations and objects, to the safeguard of people that might accidentally come in contact with dangerous substances and events. Typical example are miners, speleologist and again rescue professionals, e.g. Anesthetists and Firemen. If the environment to be monitored is fixed, e.g. a surgery room, the environmental sensor could be placed in the most sensitive and populated areas, otherwise they should be integrated on the subject's garments such to make the worker itself an "environmental probe" of the visited area.
4. Logistics: Among the different aspects concurring to the complete definition of healthcare, one of the most interesting and pervasive is surely the possibility to monitor the quality and the state of medicines and food, as well as their correct assumption. Medicine and food could easily deteriorate if not correctly stored and managed, e.g. if they are exposed to wrong environmental conditions such as high temperature and humidity, and cause serious health problems if unconsciously assumed. It thus necessary to monitor their quality and state everywhere, from the producer to the final users, passing uninterruptedly through the distributor. Same considerations can be done for blood units. Parallel to the monitoring of the food/medicine state, it is important to monitor also their assumption in order to prevent under/over dosage and to help subjects in following healthy diets compliant with their medical state. The monitoring strategies could involve sensors embedded in

the goods and able to directly transmit their data to a global server, as well as to the users's mobile devices.

5. Implanted device: A strategic role in the present and future healthcare will be in charge of implanted medical devices. Their widespread diffusion and their importance in restoring physiological functions and, definitely, in saving lives, actually prompt the need of a continuous monitoring of their functionality and their effectiveness. Such an observation could be useful to the clinicians to evaluate the effectiveness of their action and accordingly to update the medical treatment, or more drastically to prevent severe drawbacks for the patients in case of complications and failure. Ideally the implanted sensor should be able to locally transmit their data to the patient's PDA; from there the informations should finally arrive to the general medical server.

1.2 HOW

The requirements for an efficient healthcare system concern both communication network and devices. The system should be autonomous, highly personalized and almost transparent: it should be shaped around the patients and work without disturbing the activity under monitoring. An interesting review of the most important constraints for a wearable monitoring system can be found in [4] and summarized as:

1. Wearability: The system must have the features of low weight and small size to be easily carried or worn. The most bulky component of such a kind of system, e.g. the battery and the antenna, must be miniaturized without excessive degradation of their properties;
2. Localization: The system has to be noninvasive, comfortable and unobtrusive (or even aesthetic) without or with very little hindrance to user activity and appearance;
3. Usability: The user interface of the system should meet the principles of simplicity and friendliness. The number of user

operations to achieve desirable goals should be as small as possible. And the result display has to be intuitive to understand;

4. Confidentiality and Security: The transmission and storage of personal medical data have to be protected, e.g. encryption and controlled access;
5. Reliability: The results produced by the system should be trustable for the professional;
6. On-board processing: The ability of processing data on-board can facilitate the user (see the results display instantly) and enable emergencies to be handled in time. But this enhancement of computational power will increase the complexity of the system at the same time;
7. Communication and interconnection: The communication between on-body electronics and home/remote computers, and the interconnection among on-body electronics should also be weighed carefully. The communication infrastructure should work in usual and unusual scenarios, in the former case it could be fixed in the building, in the latter, instead, a personal portable device, e.g. a radio transmitter, a PDA or a mobile phone, should be act as local interrogator and hub.
8. Power supply: Lower power consumption can support longer work of the system;
9. Decision support: The system should have a certain intelligence to make decisions or diagnosis without the human intervention. In first approximation, this issue could be faced by setting only the most useful data to transmit, e.g. the ones exceeding a dangerous threshold level;
10. Scalability: The ability of adding and removing components (e.g. sensors) can increase the flexibility and applicability of the system;
11. Validation: The system should be tested enough in real situations to demonstrate the validity and practicability.

12. Cost: The system's long term cost should be contained in order to allow a widespread diffusion.

Despite the keen interest of a large part of the research community, these challenges are not fully addressed especially those related to the diffusion. In many cases, the proposed solutions are far from real applications due to their useless complexity: many physiological and pathological conditions, in fact, could be diagnosed by only inferencing indicators and low level information, without the need of elaborate platforms [5].

1.3 RFID APPROACH

Pervasive Healthcare system can benefits by RFID technology at various degree and with different aims. Most solutions propose the use of RFID tags opportunely placed on objects and people for merely identification purposes: access control and inventory are typical activities of such systems and if, properly integrated with traditional wireless sensor network, they can sensibly improve the monitoring strategies. Considering logistic applications, healthcare systems could benefit from RFID technology in reducing medical mistakes related to wrong patient/drugs/blood association, reducing costs of the information system, reducing theft loss by tracking medical devices, especially expensive assets, avoid drug counterfeiting and optimize inefficient workflow [6].

Behavioral parameters, such as the assumption of medicine or food, are interesting application of RFID platform, demonstrating how it is possible to recognize activity and motion patterns of patients by analyzing only their interaction with the objects [7, 8]. In this perspective, an innovative paradigm for RFID passive technology, involving direct interaction between tags, has been recently proposed for healthcare systems [9], promising improved scalability of the entire system and a better decision support.

The possibility to integrate sensors has been instead investigated mainly for active devices, in which an on-board battery enables both communication and sensing functions. In this acceptance they are not dissimilar from traditional active sensors.

A completely different approach is the use of passive UHF RFID tags, integrating or not passive sensors, as wireless sensor nodes for pervasive healthcare systems. The benefits of such an approach reside in the possibility to have very low cost (few euro or even less) devices, disposable, that do not need to be recharged and that may be manufactured in low-profile technology making feasible their permanent integration within clothes and everyday devices. Even if much less performing than the active sensing devices, the RFID sensors are expected to give useful information about the subjects: it is possible to envisage more RFID devices opportunely placed inside and outside the body, that give independent data, such to monitor the patients from different perspectives. The pervasive nature of RFID technology could improve the transparency and the scalability of the platforms, making the system highly personalized.

The most challenging issues for passive RFID-sensor are:

- the design of tag antennas suited to application over (or even inside) the human body (or any other high-dielectric object). It generally produces a strong pattern distortion and reduces the tag efficiency due to energy dissipation and scattering
- the extraction of the sensed data out of the backscattering response of a passive tag without the use of any dedicated microcontroller.

The first goal requires the tag design to directly include the presence of a human body model. Data extraction may be accomplished by consideration that the RFID tag acts as a digital device which, when interrogated and energized by a reader, send back its own ID. Moreover, the tag may be also considered as an analog component whose strength of received and backscattered power is sensibly affected by the electrical feature of the antenna, which is in turn dependent on the tagged object change. Different kind of sensors able to properly influence the reader-tag communication according to their state may be easily integrated with the RFID wearable device, such as inertial switches to monitor human body motion, thermal fuse for its temperature and sensitive paints for chemical detection.

Within this scenario, this thesis is aimed is to investigate the feasibility of a Pervasive Healthcare System entirely based on passive UHF RFID Technology, a kind of Internet of Body, a scenario where persons and even their internal organs are tagged whith the aim to continuously and remotely have information about their condition and state (Fig.3). By means of theoretical studies and experimental analysis all the key issues characterizing traditional Pervasive Healthcare System will be translated into the RFID context, working toward the solutions of the most severe and limiting problems.

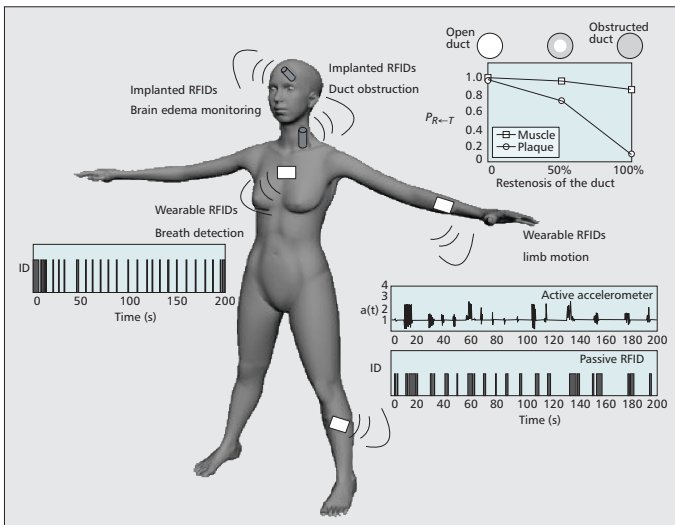


Figure 3: Internet of Body: persons and even their internal organs are tagged whith the aim to continuously and remotely have information about their condition and state.

2

RFID TECHNOLOGY AND SENSING PARADIGMS

In this chapter the theory of RFID Technology and the related sensing approaches will be described, as well as the strategies to control and optimize the sensing activity in both scenario, from outside and from inside.

An RFID system comprises two components: the remote transponder or *tag*, including an antenna and a microchip transmitter, located on the object to be identified and the local querying system or *reader*, which can read and elaborate the data transmitted from the tag. Various kinds of data and first of all a unique identification code (ID) can be wireless transferred to the reader by means of radio-frequency electromagnetic signals.

The tags could be *passive*, harvesting energy from the interrogating system, *semi-active* when a battery is included only to feed the sensors, or *fully active* where a local source directly feeds a microcontroller as well as the transmitting radio. This thesis is focused on passive systems, which may have a near unlimited life and very low cost. Among the actual solutions, the most attractive standard is the UHF (860-960MHz), which in principle promises significative activation ranges.

In *passive* technology, at the beginning of the reader-to-tag communication protocol, the reader first activates the tag, placed over a target object, by sending a continuous wave, which, by charging an internal capacitor, provides the required energy to perform actions. During this *listening mode*, the microchip exhibits an input impedance $Z_{\text{chip}} = R_{\text{chip}} + jX_{\text{chip}}$, with X_{chip} being capacitive.

The antenna impedance $Z_A = R_A + jX_A$ has to be matched to Z_{chip} ($Z_A = Z_{\text{chip}}^*$) for maximum power transfer. During the next steps of the communication, the tag receives the command coming from the reader and finally sends back the data through a *backscattered modulation* of the continuous wave coming from the reader itself. In this case, the tag's IC acts as a programmable switching device between a low impedance and a high impedance, thus modifying the reflectivity of the responding tag, and hence the strength of the reflected power.

While the most assessed use of RFID passive technology is the item labeling, there is a growing interest in new applications devoted to sense the variation of the tagged objects as well as of the nearby environment [10]. A new frontier in this area is the wireless monitoring of people within mobile healthcare services [11], [8] by tags equipped with passive sensors or acting as sensors without any additional component.

This Chapter explores by means of theoretical considerations the sensing paradigm of the RFID technology, providing innovative design guidelines and useful sensing metrics. Since an RFID sensor tag must contemporarily satisfies communications and sensing constraints, the typical design procedures and objectives must be revisited or even rethought.

2.1 RFID-SENSING EQUATIONS

It is assumed to denote with $\Psi(t)$ a local physical, chemical or geometrical parameter of the environment surrounding the tag which has to be monitored by the RFID platform. According to the specific applications, Ψ could be the presence in the air of gases and chemical species able to react with the sensitive materials integrated into the antenna, a physical stimulus, e.g. an acceleration, able to affect a discrete sensor loading the RFID tag, a shape factor of a biological process or, more generally, the local effective permittivity "sensed" by the tag's antenna.

The well known [12] two-way reader-tag link may be rewritten making explicit the dependence on the variation of local parameters with the purpose to obtain some sensing indicators which can be derived by the reader's measurements [13]. The power

collected at the microchip (2.1) and the power backscattered by the tag toward the reader (2.2) and collected by it are:

$$P_{R \rightarrow T}[\Psi] = \left(\frac{\lambda_0}{4\pi d} \right)^2 P_{in} G_R(\theta, \phi) G_T[\theta, \phi, \Psi(t)] \tau([\Psi(t)] \eta_p) \quad (2.1)$$

$$P_{R \leftarrow T}[\Psi] = \frac{1}{4\pi} \left(\frac{\lambda_0}{4\pi d^2} \right)^2 P_{in} G_R^2(\theta, \phi) \eta_p^2 rcs_T[\theta, \phi, \Psi(t)] \quad (2.2)$$

where d is the reader-tag distance, $G_R(\theta, \phi)$ is the gain of the reader antenna, $G_T[\theta, \phi, \Psi(t)]$ is the gain of the tag's antenna. P_{in} is the power entering the reader's antenna, η_p is the polarization mismatch between the reader and the tag, and $\tau[\Psi(t)]$ is the power transmission coefficient of the tag :

$$\tau[\Psi] = \frac{4R_{chip} R_a[\Psi]}{|Z_{chip} + Z_a[\Psi]|^2} \quad (2.3)$$

with Z_{chip} input impedance of the RFID integrated circuit (IC) and Z_a input impedance of the antenna. rcs_T is the tag's radar cross-section, related to the modulation impedance Z_{mod} of the microchip to encode the low and high digital state:

$$rcs_T[\Psi] = \frac{\lambda_0^2}{4\pi} G_T^2[\theta, \phi, \Psi(t)] \left(\frac{2R_a[\Psi]}{|Z_{mod} + Z_a[\Psi]|} \right)^2 \quad (2.4)$$

The backscattered power $P_{R \leftarrow T}$ is directly measurable by the reader in terms of the Received Signal Strength Indicator (RSSI), here assumed to correspond [12], [14] to the binary modulating state having $Z_{mod} = Z_{chip}$.

Another parameter that can be measured by the reader is the *turn-on power* $P_{in}^{to}[\Psi]$, e.g. the minimum input power P_{in} through the reader's antenna forcing the tag to respond. It can be derived from (2.1), considering $P_{R \rightarrow T} = P_{chip}$ that is the microchip sensitivity.

$$P_{\text{in}}^{\text{to}}[\Psi] = \left(\frac{\lambda_0}{4\pi d}\right)^{-2} \frac{P_{\text{chip}}}{G_{\text{R}}(\theta, \phi)\eta_{\text{p}}G_{\text{T}}[\theta, \phi, \Psi]\tau[\Psi]} \quad (2.5)$$

From turn-on measurement it is possible to extract the *realized gain* of the tag $G_{\tau}[\Psi]$, e.g. the gain of the tag scaled by the mismatch to the IC, strictly correlated to the physical variation of the local environment:

$$G_{\tau}[\Psi] = \left(\frac{4\pi d}{\lambda_0}\right) \frac{P_{\text{chip}}}{G_{\text{R}}(\theta_{\text{R}}, \phi_{\text{R}})P_{\text{in}}^{\text{to}}} \quad (2.6)$$

Finally, forward (2.1) and backward (2.2) powers may be combined at turn-on with the purpose to drop out the influence of the distance and of the reader and tag gains and orientation [15, 16]. A non-dimensional indicator, denoted as *Analog Identifier* (AID), can be hence introduced:

$$\text{AID}[\Psi] = \frac{P_{\text{chip}}}{\sqrt{P_{\text{R}\leftarrow\text{T}}[\Psi]P_{\text{in}}^{\text{to}}[\Psi]}} = 2R_{\text{chip}} |Z_{\text{chip}} + Z_{\text{a}}[\Psi]|^{-1} \quad (2.7)$$

and it is very useful when the interrogation set-up changes (position and orientation) in successive measurements. The AID, in fact, just depends on the impedance mismatch and is immune to the interrogation modalities.

2.1.1 Sensing Metrics

The indicators in (2.5), (2.2) and (2.7), may be used as *data inversion curves* $p[\Psi(t)]$ between the measured data and the evolution $\Psi(t)$ of the process. Only two of them are independent, since the tag undergoes change in gain and impedance mismatch. They can be discretely evaluated, e.g by considering the single values at one or more significative frequencies or analyzed in the entire frequency band, such to have macroscopic metrics. In both cases it could

be useful to normalize each indicator to its value in a particular reference state, say Ψ_0 , for instance collected at the time of the tag placement into the environment to be monitored.

Due to the normal fluctuations of signals, especially of the backscatterd power, particular shrewdnesses should be considered in order to decrease the uncertainties of the measurements. A statistical analysis of the phenomena in term of mean and standard deviation and based on a significative number of samples can sensibly reduce the random errors of the measurements, while a correct calibration of the instruments and their accuracy can obviously reduce the systematic errors. The latter issue becomes even more challenging because the actual RFID commercial readers are mostly devoted to logistic and inventory applications and thus do not offer great performances and robustness in sensing employments.

By considering the local value at a particular frequency it is possible to determine sensing profiles similar to the ones shown in Fig.4. The curves refer to an RFID radio sensor loaded with carbon nanotubes sensitive to gases. More precisely, as it will detailed in Chapter 7, the figure represents the variation of realized gain and analog identifier along with time, during the exposure of the sensor to ammonia, NH_3 , for two fixed frequencies.

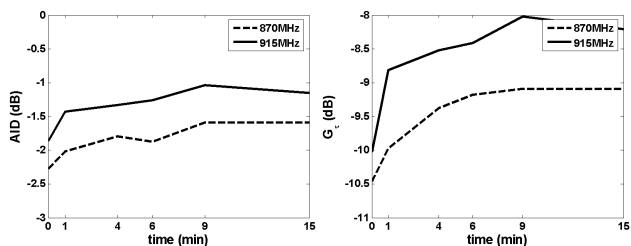


Figure 4: G_τ and AID for an RFID sensor tag loaded with carbon nanotubes and exposed to NH_3 in the air.

Two useful indicators for such a kind of curves could be the *Dynamic Range*:

$$\Delta\xi(\Psi_i) = \frac{\xi(\Psi_i) - \xi(\Psi_0)}{\xi(\Psi_0)} \cdot 100 \quad (2.8)$$

and the *Sensitivity* of the sensor, defined in the linear range of the response as

$$s [\%] = \frac{\xi(\Psi_{\max}) - \xi(\Psi_0)}{\Psi_{\max} - \Psi_0} \quad (2.9)$$

which gives the percentage variation (increase or decrease) of the collected data, with respect to the initial condition, in the time unit. In both cases ξ is the generic sensing indicator.

Fig. 5 shows typical multi-frequency profiles of measured turn-on powers of a sensor-less radio sensor during a process in which the complex permittivity of the environment surrounding the tag progressively changes. It is clearly visible a monotonic amplitude scaling in the entire band: as the permittivity decreases, the communication links becomes more robust and the radio sensor results readable also at higher frequency. However, due to the oscillating behavior of the signals, a monochromatic analysis, e.g considering only the local variation at a fixed frequency, could produce uncertainties and distortion of the information.

To overcome this effect, it could be useful to introduce aggregated indicators by performing averaging in the whole frequency band, such as the *Normalized Scale Factor*:

$$\gamma_\xi = \frac{\langle \xi(\Psi) - \xi(\Psi_0) \rangle}{\langle \xi(\Psi_0) \rangle} \quad (2.10)$$

where the “ $\langle \rangle$ ” brackets indicate the average over frequency samples.

In the most general case the evolving process could produce also a frequency shift (Fig. 6), e.g a variation of the peak (minimum)

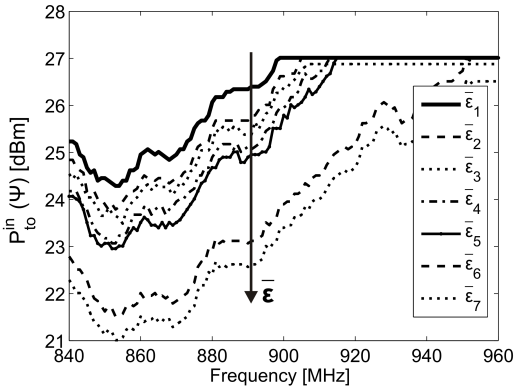


Figure 5: A typical sensing profile of the measured turn on power in the UHF (World- Wide) Band

value of the sensing indicator. In such a cases correlations between the different signals can be used to better discriminate the events.

2.2 SENSING PARADIGMS

Most of passive RFID tags for human body sensing can be grouped according to the fact that they make use or not of integrated specific sensors to detect the variation of the tagged object and of the environment.

2.2.1 *Sensor-less Tag*

Any tag may be considered as a sensor of the effective permittivity of the object where it is attached on. Like any antenna placed onto a real medium, the electrical properties of an RFID tag, such as the input impedance and the radiation gain, are strongly correlated with the physics of the nearby environment. A change of the tagged object is globally seen by the tag's antenna as a change of equivalent permittivity which will in turn produce a change of the tag's antenna features and hence of the received and backscattered

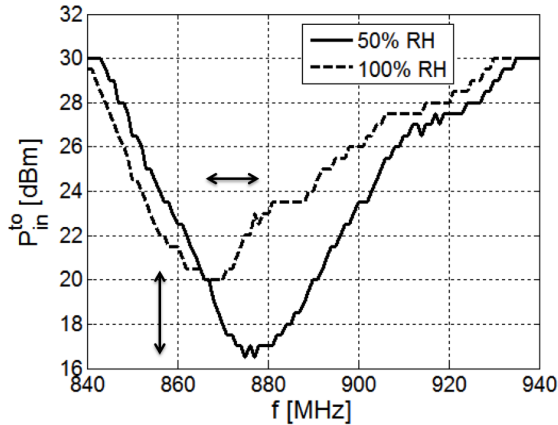


Figure 6: Turn-on power in the UHF (World- Wide) Band for an RFID tag doped with sensitive polymers and exposed to relative humidity RH in the air.

signals. So a *self-sensing*, completely sensor-less, passive device [17] is obtained wherein the sensor is the antenna and the antenna is the sensor. However this sensing mechanism is non-specific, since the sensed data may be only indirectly related to a physical phenomenon to monitor. The sensing hence requires inversion curves, or lookup tables, produced by off-line experimentation or computer simulations according to a training procedure relating the signals received by the reader, to the phenomenon's state.

2.2.2 Loaded Tag

The tag is equipped with a real sensor which could be either lumped into a device, connected in some part of the tag's antenna, or instead distributed all over the antenna surface as a chemical receptor painting. Such a sensing mechanism may be hence considered as a lumped or distributed impedance loading $Z_S(\Psi)$ on the tag's antenna. The variation of $Z_S(\Psi)$, caused by the change of the environment, will produce a change of the tag's

radiation performances, e.g its radar cross-section and hence the backscattered power modulation as in the case of sensor-less tags or the turn-on power. Moreover, these kinds of devices are suited to include specific and direct sensing mechanism, rather than macroscopic ones as in case of self-sensing RFIDs.

2.3 OPTIMIZATION STRATEGIES

In either approaches, sensor-less and loaded tag, the sensing activity can involve a contemporary variation of both input impedance and gain or of only one of them. In any case, the RFID passive sensor tag should be able to properly follow the dynamics of the phenomena under monitoring, being for example monotonic, single valued and sensitive enough at least in the most critical ranges.

Denoting with $R = [\Psi_{\min}, \Psi_{\max}]$ the range of the process to be sensed, it is required that the inversion curve (say $p(\Psi)$ in general) is monotonic in R and with a given variation, s , e.g.

$$\Delta p(R) = |p(\Psi_{\max}) - p(\Psi_{\min})| \rightarrow s \quad (2.11)$$

Moreover the radio-sensor has to be subjected to constraints over the maximum interrogation power $P_{\text{EIRP}}^{\text{to}} = P_{\text{in}}^{\text{to}} G_R$ to permit a suitable communication, at a given tag-reader distance, for the whole process's range R and in agreement with power regulations or with the expected capabilities of the reader:

$$P_{\text{EIRP}}^{\text{to}}(\Psi) \leq P_{\text{Max}}, \quad \Psi_{\min} \leq \Psi \leq \Psi_{\max} \quad (2.12)$$

It is worth noticing that the parameter Ψ and the corresponding variation of $p(\Psi)$ can be either continuous, such as in most biological processes, or discrete, such as when the tag integrates passive sensors able to reply only if the stimulus exceeds a threshold value. This last case could be eventually characterized by only two value of Ψ , e.g on/off state, like conventional digital communications.

It is easily inferable that the narrower is the variation range of the phenomena under monitoring, the more challenging will be the sensing activity and thus the design of a radio-sensor able to comply with (2.11) and (2.12). More precisely, the sensitivity and the dynamic range of the system are strictly connected to the antenna's features, in particular to its quality factor, and definitely to its bandwidth (related in the RFID contest to the tag's realized gain G_τ [18]): the narrower the antenna bandwidth, the higher is its sensitivity to the variation of nearby environment and thus the better its sensing capabilities are.

Communication and sensing features demand for opposite requirements, since the sensitivity of the tag-as-sensor to the variation of the process under observation is usually paid in terms of a worsening of the power scavenging capabilities and in particular of the read distance. Seeing that there is no decoupling from the operative and structural point of view between antenna and sensor, the traditional design procedures have to be revisited or even rethought in order to handle at the same time both sensing and communication needs.

2.3.1 Method

RFID platform exploits a two-way communication link, a direct one, wherein the key-issue is the scavenging of power at the chip's port so that the tag may activate and perform actions, and a reverse link wherein the tag transmits its data to the reader by changing its reflectivity through impedance modulation. Generally, the direct link imposes the bottleneck of the whole tag-reader communication and it limits the maximum read range. The parameter that represents the tag's scavenging features is the realized gain $G_\tau = G_T\tau$, e.g the gain of the tag's antenna scaled by the mismatch to the RFID IC. A trade-off solution to the sensing-communication problem is to observe the state of the object Ψ (chemical/physical process in evolution) through a measurable quantity whose variation is not necessarily associated to a worsening of the communication performance. Such an indicator should be optimally a parameter of the reverse-link such as the backscattered power which is however orientation-

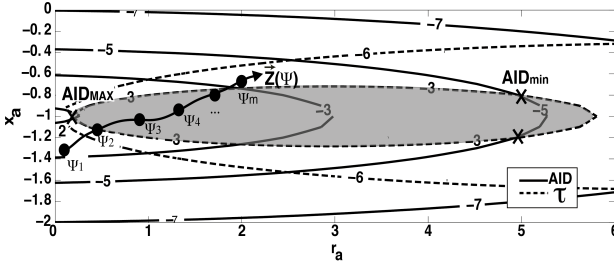


Figure 7: Iso-line of constant AID and τ on normalized antenna impedance plane. In grey the area corresponding to $\tau_{\min} = -3\text{dB}$. The curve $\bar{Z}[\Psi] = r_a(\Psi)\hat{i} + x_a(\Psi)\hat{j}$ indicates a possible variation of the antenna's impedance all along the process in evolution.

and position-dependent. If some degradation can be accepted, the Analog Identifier (AID) [13] is also a convenient metrics since combines both the direct and the reverse links to provide a sensing information independently on the reader-tag position and orientation as well as on the interaction with the surrounding environment.

Due to the small size of the UHF tag's antenna, there are very few degrees of freedom in shaping the gain: the direct and reverse links could be therefore analyzed in term of the only input impedance by considering the power transmission coefficient $\tau(\Psi)$ and the AID(Ψ). These are usefully expressed in terms of normalized input impedance [19] $r_a = R_A/R_{\text{chip}}$, $x_a = X_A/X_{\text{chip}}$, with $Z_{\text{chip}} = R_{\text{chip}} + jX_{\text{chip}}$ the RFID chip's impedance and $Q = |X_{\text{chip}}|/R_{\text{chip}}$:

$$\tau[\Psi] = \frac{4r_a}{|1 + r_a + jQ(1 + x_a)|^2} \quad (2.13)$$

$$\text{AID}[\Psi] = \sqrt{\tau[\Psi] \frac{R_{\text{chip}}}{R_a}} = \frac{2}{|1 + r_a + jQ(1 + x_a)|} \quad (2.14)$$

A chart of $\{AID, \tau\}$ isolines can be produced so that the communication and the sensing characteristics of the tag are together expressed (Fig.7).

The point $(1,-1)$ corresponds to the perfect matching condition between antenna and IC, for which $AID = \tau = 0\text{dB}$: the state of the process Ψ , real or virtual, for which the radio sensor shows the best matching to the IC is denoted *matched state*, Ψ_m . The eccentricity of the ellipses depends on the quality factor Q of the microchip.

The AID - τ diagram can be considered as a kind of *Sensing Smith Chart*, in which the role of the frequency is replaced by the process Ψ . Each process in evolution from an initial to a final state, involving a modification of input impedance, can be traced over such a plane by a sequence of couplets $(r_a(\Psi_n), x_a(\Psi_n))$ describing an oriented curve $\vec{Z}[\Psi] = r_a(\Psi)\hat{i} + x_a(\Psi)\hat{j} \in \mathbb{R}^2$. Along the process, $\vec{Z}(\Psi)$ can move from or to the matched state $(1,-1)$; to be general, if the RFID sensor is designed to be matched in a fictitious realization of the process, i.e. Ψ_m doesn't belong to Ψ , only part of $\vec{Z}(\Psi)$ represents the range of the process R . In order to have monotonic profile in R , Ψ_m should be the end or the beginning of the process: since τ has almost everywhere opposite values around the matching point $(1,-1)$, intermediate values of Ψ_m give non monotonic trends and could be useful to enhance the variation of the sensing parameters in specific sub regions of R . The amplitude of the sensing response is mainly determined by the impedance evolution: the wider is the range of the input impedance variation, the longer is the path of $\vec{Z}(\Psi)$. Similar considerations can be done about its direction: in the most general case $\vec{Z}(\Psi)$ has a certain slope α respect to the r_a -axis, if the process produces predominantly variation of real part, the sensor response tends to be parallel to the x_a axis ($\alpha = 0^\circ$), oppositely in case the variation is mostly on the imaginary part ($\alpha = 90^\circ$). The slope of the curve \vec{Z} with respect to the r_a -axis will affect the sensitivity of the tag's response to the process' evolution.

If the process in evolution is not linear, e.g the variation of input impedance is not progressive and monotonic, the different

realizations $(r_a(\Psi_n), x_a(\Psi_n))$ will describe broken lines, in whose each parts the previous considerations apply.

To preserve a stable read-range of the tag during the whole evolution of the process, it is required that $\tau[\Psi] > \tau_{\min}$. For instance the choice $\tau_{\min} = -3\text{dB}$ will permit not to degrade the read range below the 30% of its maximum value corresponding for example to the initial (or final) state of the process. Above constraint enforces the vector $\vec{Z}(r_a, x_a)$ to belong to the shadowed elliptical region in Fig.7. Moreover, the same condition will fix the maximum variation of AID, in the specific: $-5\text{dB} < \text{AID}[\Psi] < 2\text{dB}$ as observed by the intersections between the isocurves. In general, the path $\vec{Z}(r_a, x_a)$ can totally, partially or even not belong to such an area: only the dynamics of Ψ inside the shadowed ellipse will be observed by the radio sensor.

Another possibility is to explore the direct and reverse links by means of the realized gain $G_\tau[\Psi]$. Reverse link depends on G_τ through the rcs_τ (2.4), which can be rewritten as:

$$\text{rcs}_\tau[\Psi] = \frac{\lambda_0^2}{4\pi} G_\tau^2(\theta, \phi, \Psi(t)) \frac{R_\tau}{R_{\text{chip}}} \tau(\Psi) \quad (2.15)$$

In order to drop out the influence of gain from both indicators, it is possible to consider the $\sqrt{\text{rcs}_\tau}$, such to have a chart of $\{\sqrt{r_a\tau}, \tau\}$ isolines (Fig.8). Similarly to the $\{\text{AID}, \tau\}$ chart, also in this case it is possible to define a constraint on τ_{\min} to preserve a stable read-range all along the process; e.g for $\tau_{\min} = -3\text{dB}$ (gray ellipses in Fig.8) $-5\text{dB} < \sqrt{\text{rcs}_\tau} < 2\text{dB}$.

It is interesting to notice, by comparing Fig.7 and Fig.8, that to maximize the sensing link in is necessary to place $\vec{Z}[\Psi]$ approximately in the same manner on the plane (r_a, x_a) : by designing a tag in such a area it is thus possible to optimize the variation of both analog identifier and backscattering variation without extreme degradation of the communication performances, i.e. avoiding strong variation of the power transmission coefficient τ .

The issue of maximizing the power transmission coefficient and the rcs_τ in the design phase has been recently discussed in [20] by considering only the communication functionality of the tag: thanks to $\{\sqrt{r_a\tau}, \tau\}$ chart, instead, it is possible to demonstrate

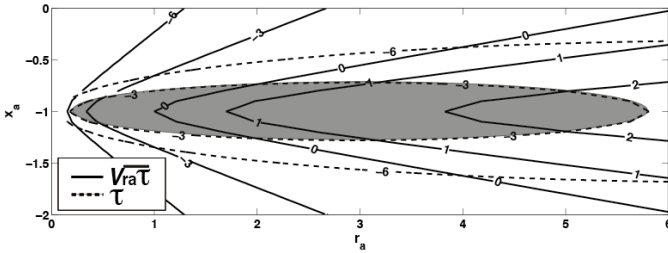


Figure 8: Iso-line of constant $r_{cs\tau}$ and τ on normalized antenna impedance plane. In grey the area corresponding to $\tau_{min} = -3\text{dB}$.

that, although it is not possible to contemporarily maximize in the same tag the power scavenging, i.e τ , and the backscattered power, i.e $r_{cs\tau}$, it is however possible to dynamically optimize their coexistence for sensing purposes.

Tag's gain

Like for conventional small antenna design, also for the RFID radio-sensor the gain of the antenna is particularly difficult to shape according to the variation of the surrounding environment. In general gain depends on the shape of the antenna, on the currents distribution and on the way the electric and magnetic fields behave in the close reactive region. In particular, these latter effects are extremely difficult to be analytically described and predicted, especially for small antennas.

However, some considerations could be done for example about RFID radio-sensors loaded by sensitive materials with, for example, variable conductivity. The sensitive material could be considered as a part of the antenna's radiating structure, e.g. an antenna totally or partially made of conductive carbon nanotubes, or instead as a doping component of the tag, e.g. a variable load properly placed in close proximity of the radiating elements [21]. By considering the material as a radiating element, it is possible to maximize the sensitivity of the device, however lowering

the antenna efficiency and the activation distance of the RFID tag. These two parameters, together with the cost, are essential in RFID systems. The other solution, on the contrary, offers better communication and cost performances but could provide a weaker sensitivity to the analytes. Both solutions thus offer advantages and drawbacks; the best trade-off must be finally adopted in order to fully respect (2.11) and (2.12).

2.4 ENGINEERING THE DATA INVERSION CURVES

The design procedures has to confine $\vec{Z}(r_a, x_a)$ inside the $\tau[\Psi] > \tau_{\min}$ region. There are at least three degrees of freedom available to master the communication and sensing performances of such an RFID radio sensor in term of input impedance, e.g. the shape of the antenna, the family of microchips and, not least, the state Ψ_m (real or virtual) of the process where forcing the antenna to have the best impedance matching to the RFID IC.

To account for all these issues the reference model of Fig.9 is here adopted, where an antenna of shape S_k is connected to a microchip of impedance $Z_{\text{chip},n}$ through an Antenna Adapter AA_m . In the most general model the antenna can be loaded by means of localized and distributed sensors, describable as a lumped or distributed impedance $Z_S(\Psi)$ on the tag's antenna. The antenna adapter virtually applies to the global antenna impedance $Z_C(\Psi)$ (comprising the antenna's input impedance Z_a and the sensor's impedance Z_s whatever connected) and yields a transformed impedance Z_T which is matched to the specific microchip such to get the best response profile $\vec{Z}(\Psi)$ all along the process.

The key parameters of the sensor tag are hence related by the following matching equation:

$$Z_T [S_k, Z_s, AA_m] (\Psi_m) = Z_{\text{chip},n}^* \quad (2.16)$$

where the asterisk denotes the complex conjugate, the $[..]$ indicates the design conditions and $(..)$ the specific state of the process where the antenna's impedance is evaluated.

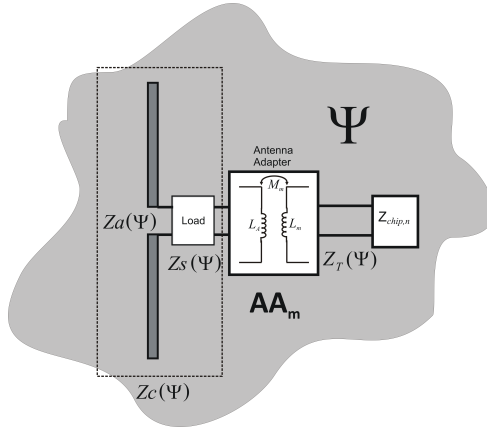


Figure 9: Reference model to investigate the key issues in the design of sensor tags. In the most general case, given a radiating structure and a sensor, an antenna adapter is used to match such an antenna with specific matching profile according to the process to be observed.

The parameter Ψ can alternatively affect the antenna's input impedance in case of the sensor-less approach or the sensor's impedance in case of loaded tags. More complex devices, involving both sensing strategies, could be obviously envisaged.

The matched state Ψ_m fixes a point of $\vec{Z}(\Psi)$, e.g. its origin, end or an intermediate value and its verse, e.g. to, from or through $(1, -1)$; Z_{chip} determines instead the global position of $\vec{Z}(\Psi)$, e.g. the half-planes $r_a \leq 1$ and the shape of the AID - τ chart by the ellipses axial-ratio Q ; finally, the AA shapes the overall $\vec{Z}(\Psi)$.

The effect of the Antenna Adapter could be obtained [18], for instance, by an inductively coupled loop placed in close proximity of the radiating structure, a T-match or, more simply, by adding discrete inductors/capacitors. Generally, the AA can be considered as a filter with geometrical or electrical parameters to be found by any kind of optimization method.

An easy and practical realization of design procedure could work as follows:

i) select the antenna shape S_k together with the topology of the antenna adapter (a T-match, a coupled loop, or even discrete inductors/capacitors). These choices will follow the specific medical application to monitor, the position inside/outside the body and the available space;

ii) Fix the constraints in (2.11) and (2.12). The latter condition will define τ_{\min} , thus the region where confine $\vec{Z}(r_a, \chi_a)$ and the maximum achievable variation of the sensing indicators, e.g. AID or backscattered power:

iii) evaluate by means of numerical analysis or experimentation on realistic phantoms the effects of the process Ψ on the tag's input impedance (increase/decrease of R_A and/or X_A);

iv) select the microchip family (Z_{chip}) such to localize the response $\vec{Z}(\Psi)$ on the sensing chart. The curve can be positioned on the plane by selecting a guess value for the matched state Ψ_m , belonging or not to the process evolution R . For instance the first guess for Ψ_m could be that corresponding to the initial or final condition;

v) estimate from (2.16) the parameters ΛA_m of the antenna adapter so that the transformed impedance Z_T of the antenna is matched to the IC and the other points of the process belonging to $\vec{Z}(\Psi)$ are positioned in the best way;

vi) Plot $\vec{Z}(\Psi)$ on sensing charts and verify the sensing and communication constraints in (2.11) and (2.12);

vii) if such conditions are respected then the parameters of the antenna adapter found in *v)* will give the final design

viii) if the check in *vi)* is instead unsuccessful, then modify the matched state Ψ_m and/or select a different microchip and go back to step *iii)*.

Thus the shaping of the radio-sensor's response is mainly reduced to an iterative search for the most appropriate microchip and mostly for the matching state.

It is finally possible to appreciate the flexibility of the matching procedure which permits to adapt a same shape of tag to different processes in evolution by just changing the antenna adapter.

Realistic examples are given in the first and second part of the Thesis for very simple realizations of the Adapter.

2.5 NUMERICAL STUDY

The previous analysis can be obviously applied to the design of all passive RFID sensors, regardless the physics of the phenomena (discrete or continuous) or the location of the radio-sensor (wearable, implantable, environmental). Two numerical examples will be presented, concerning a dipole-like tag used to monitor a low-dielectric process and an implanted tag used to monitor a biological lossy phenomenon.

2.5.1 Low dielectric process

It now designed an optimized tag for the wireless monitoring of the filling level ($\Psi = h$) of a perspex box containing sugar (FDTD model in Fig.10) [22]. The first guess for the tag-as-sensor is a simple half-wave dipole @870MHz. The considered RFID IC has impedance $Z_{IC} = 17 - j190\Omega$ and the corresponding AID – τ chart is shown in Fig. 11(top). The communication performances are preserved by enforcing the constrain $\tau_{min} = -1\text{dB}$ (less than 10% reduction in the read range). Accordingly, the maximum variation of the AID could be at most $\Delta\text{AID} = 1 - (-2\text{dB}) = 3\text{dB}$ (Fig.11 top), while $\Delta\sqrt{rcs\tau} = -2 - (1.5\text{dB}) = 3.5\text{dB}$ (Fig.11 middle). The response, say $\vec{Z}_A[\Psi]$, of the monopole lies outside the useful area, it exhibits a non monotonic profile and hence it is not suited to sensing and neither to communication; an impedance adapter is thus added to reshape the curve (Fig.10). The form factor (a, b) of the T-match is optimized with the aim to move the tag's response (now denoted as \vec{Z}_B in Fig.11 top) inside the shadowed region $\tau > -1\text{dB}$ and to achieve a monotonic profile. In this case, \vec{Z}_B has been anchored to the point (1-1) by choosing a matched state $\Psi_m = 2\text{cm}$.

Fig.11 bottom shows the corresponding AID , \sqrt{rcs} and τ parameters versus the sugar's height for the optimized tag with $a=13\text{mm}$, $b=20\text{mm}$. As expected the power transfer coefficient is

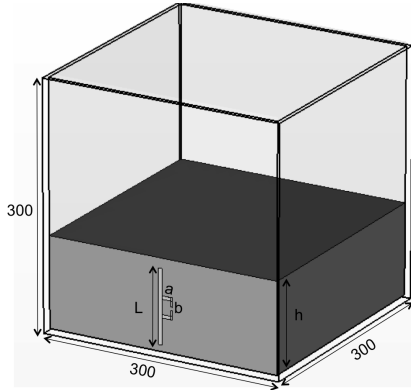


Figure 10: Passive T-matched tag to sense the level of sugar powder within a perspex box. Size after optimization in mm are $L=90$, $a=13$, $b=20$.

nearly unchanged around the matching condition which means that the reader will be able to monitor the level of the sugar with 0.3dB/cm sensitivity of the AID and $\sqrt{r_{csT}}$ and with negligible variation of the read range.

From Fig. 11 middle, it is then interesting to notice that it should be possible to further translate the response curve \bar{Z}_B by choosing a different Ψ_m , e.g $h = 4\text{cm}$ without affecting the overall communication and sensing profiles.

2.5.2 High dielectric process

The most challenging case is however the design of implantable devices. The design of an implanted radio-sensor must be strictly connected to the medical application it is going to monitor, especially regarding the inversion curve. However, as proved in [17], the electrical parameters of an RFID tag (impedance and gain) in these conditions are expected to be very little sensitive to the variation of the dielectric properties, because of the smoothing effect induced by the losses. Nevertheless, the tag has to primarily communicate with the reader and hence its embedded RFID

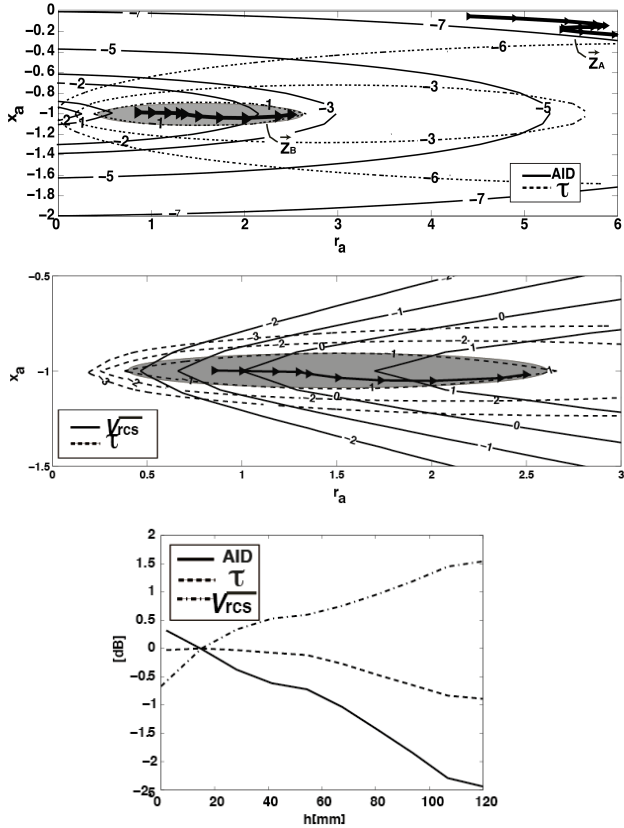


Figure 11: Top) AID – τ chart. Middle) $\sqrt{r_{csT}}$ – τ chart. In grey the area corresponding to $\tau_{\min} = -1$ dB. Z_A is the response curve of the dipole, transformed by the T-match in Z_B . Bottom) AID, τ and $\sqrt{r_{csT}}$ profile versus the filling level h [mm].

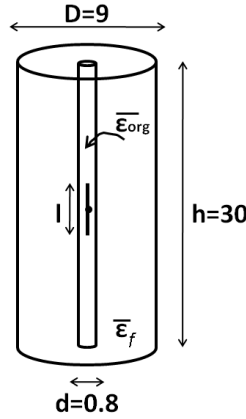


Figure 12: Cylindrical model of a body district of size comparable with an arm, the head or the neck. The inner cylinder represents an organ where there is a process in evolution. Sizes in (cm). The reference antenna is a $l = 2.2$ cm-long dipole.

microchip needs to harvest the minimum required power in all the considered process states.

To investigate the role of the various degrees of freedom on the profile of the inversion curves a canonical geometry (Fig.12) is here considered, simulating an implanted antenna into the human body. A cylinder of diameter $D = 9$ cm and height $h = 30$ cm filled by a uniform tissue-like dielectric $\bar{\epsilon}_f$ is assumed to simulate a generic human district, such as an arm or the neck. A smaller 0.8 cm-diameter cylinder, concentric to the first one filled by another uniform tissue-like dielectric $\bar{\epsilon}_{org}$, simulates instead a biological process in evolution involving a localized modification of the geometry and/or of the dielectric properties of an organ or of part of it. The complex permittivity $\bar{\epsilon}_{org}(t)$ of the smaller cylinder gradually changes along with time from a very low value up to a high value.

For the sake of simplicity, the reference antenna implanted inside the smaller cylinder is a 2.2 cm-length dipole. In a feasible application the shape of the antenna will be adapted to the specific

Table 1: Body Tissue Properties at 870MHz

Tissue	Complex Permittivity
Brain White Matter	$\bar{\epsilon}_1 = 38.9 - j12$
Liver	$\bar{\epsilon}_2 = 46.9 - j17.4$
Muscle	$\bar{\epsilon}_3 = 55 - j19.2$
Blood	$\bar{\epsilon}_4 = 61.45 - j31.5$
Edema	$\bar{\epsilon}_{org} = 50.2 - j20.78$

district or to the already existing implanted device, as shown later in the Implanted Section. The size of the antenna is approximately $\lambda/2$ in the body and may be comparable with that of vascular stents, orthopedic implants (screws, pins) or surgical nails.

Having fixed the antenna shape, the control of self-sensing performances are demanded to the reminder parameters $Z_{chip,n}$ and AA_m . Without loss of generality, the antenna adapter is here accounted as an impedance transformer (see again Fig.9) of parameters $AA_m = \{M_m, L_m\}$, which may model some of the mostly used UHF RFID layouts. Accordingly, the transformed impedance will be

$$Z_T = j\omega L_m + (\omega M_m)^2 / Z_A \quad (2.17)$$

The body model is analyzed by a Finite-Difference Time-Domain (FDTD) tool with the purpose to predict the antenna impedance in remarkable conditions. The overall tag's responses for various choices of the remaining free parameters are instead estimated in post-processing by direct manipulation of the circuit model in Fig.9.

Microchip choice

Five different ICs with increasing phase angles $|Q|_n(Z_{chip,n}) = \{0.2, 5, 10, 15, 20\}$ are here considered. The lowest $|Q|_1 = 0.2$ refers to a fictitious microchip with impedance $Z_{chip,1} = 16 + j0.4$, and the highest $|Q|_5 = 20$ corresponds to typical commercial RFID

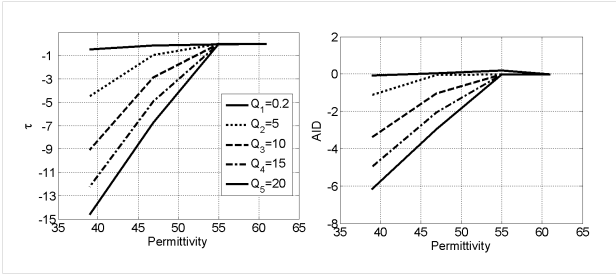


Figure 13: Simulated power transmission coefficient τ and AID (@870 MHz) of a 2.2cm-dipole placed into the small cylinder in Fig.12 when varying the dielectric properties of the internal cylinder, for five different RFID microchips. The simulated data are ordered according to the real part of the considered complex permittivity.

microchips (for instance $Z_{\text{chip},5} = 24 - j485$ [23]). The Antenna Adapter's parameters are derived, case by case, by inversion of (2.16) to achieve the best impedance matching in a same matched state $\Psi_m = \bar{\epsilon}_4$, e.g. for the permittivity of the blood at 870 MHz.

Fig.13 shows the variation of the power transmission coefficient τ in (2.3) and AID in (2.7) with respect to the change of permittivity of the smaller cylinder, for the five considered microchips. The dependence on the microchip phase angle is clearly visible: the higher the $|Q|$, the steeper will be the slope of the inversion curve.

Matching profile

The role of shape and position of the response curve $\vec{Z}(\Psi)$ is instead addressed having fixed the microchip phase angle to $Q = 10$. The considered matched state in (2.16) is taken in successive experiments as $\Psi_m = \{\bar{\epsilon}_1, \bar{\epsilon}_2, \bar{\epsilon}_4\}$, corresponding to the complex permittivity of brain, liver and blood, respectively. From Fig.14 it is evident that by varying Ψ_m it is possible to shift the curve of both indicators vs. the permittivity change. In case of τ the shift occurs without modifying its overall dynamic range, while in case

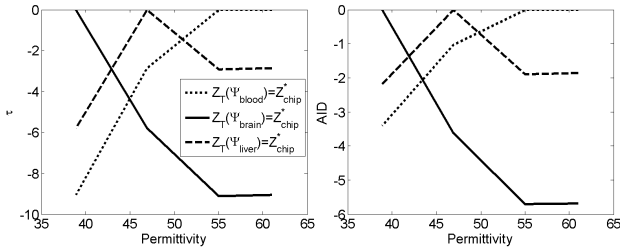


Figure 14: Power transmission coefficient τ and AID on varying the permittivity of the medium filling the inner cylinder in Fig.12, for three different choices of the matched state. In each case $Q = 10$.

of AID the dynamics is sensibly increased if the best matching is achieved for Ψ_{brain} .

The reason of such a difference of dynamics can be related to the different $\bar{Z}(\Psi)$ in Fig.15. It is easy to see that although the isolines intercepted by the τ are equal in the two conditions, the values intercepted by the AID are quite different. By considering a variation of τ of -3dB , the maximum variation of AID are -1dB for $\Psi_m = \bar{\epsilon}_4$ and -2.5dB for $\Psi_m = \bar{\epsilon}_1$. It is interesting to notice that, opposite to AID, the τ profiles are specular for the two matching conditions.

To complete the analysis is necessary to consider also the communication constraints. Let's assume a typical scenario, e.g a maximum reader's transmitted power $P_{\text{max}} = 3.2\text{W}$ EIRP which is the limit of the EU regulations for UHF RFID link, an IC sensitivity $P_{\text{chip}} = -15\text{dBm}$ and a body-reader link distance 20cm. The profiles are visible in Fig.16. Although the case $\Psi_m = \bar{\epsilon}_1$ offers a high sensitivity in the range $(\bar{\epsilon}_1, \bar{\epsilon}_2)$, most of the process's dynamic range will be detected only for a transmitted power $P_{\text{EIRP}}^{\text{to}}$ exceeding the limit, e.g. the whole range of interest $(\bar{\epsilon}_2, \bar{\epsilon}_4)$ is not practically observable. Instead, both the $\Psi_m = \bar{\epsilon}_3$ and $\Psi_m = \bar{\epsilon}_2$ options satisfy the sensing condition giving more reliable links. For instance in case $\Psi_m = \bar{\epsilon}_2$, which gives the highest slope of the AID(Ψ) curve, the corresponding parameters of the antenna adapter are $L_m = 77\text{ nH}$, $M_m = 3.7\text{ nH}$.

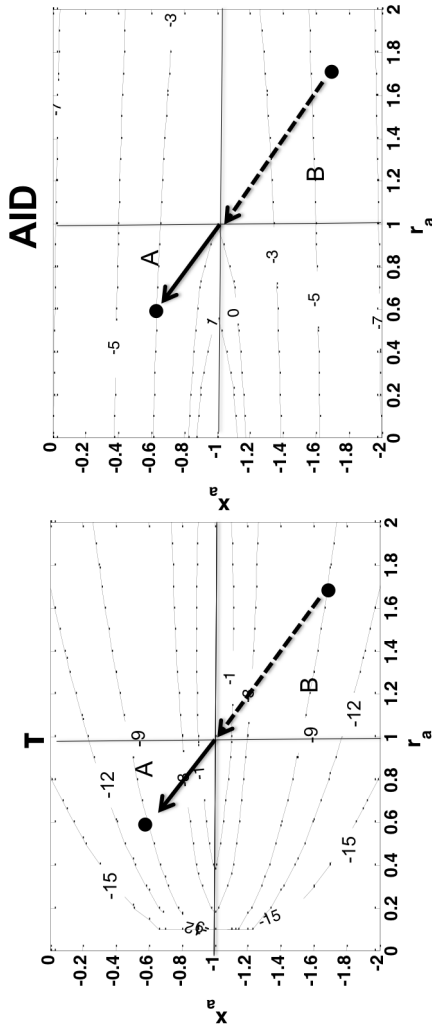


Figure 15: Power transmission coefficient τ and AID on varying the permittivity of the medium filling the inner cylinder in Fig.12, for three different choices of the matched state. In each case $Q = 10$.

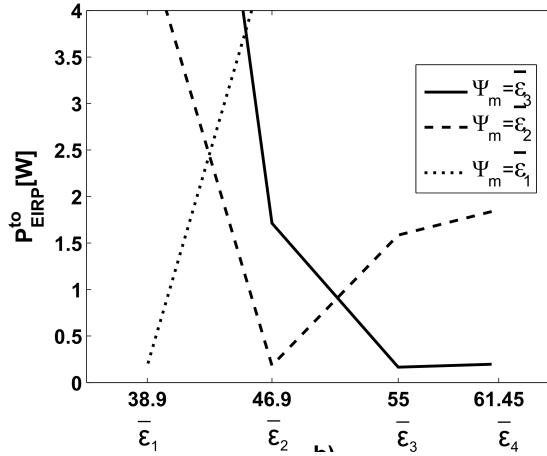


Figure 16: Simulated Turn-on transmitted powers of the implanted dipole of Fig.12 for a 20cm-link and a -15dBm microchip sensitivity for different choices of the matched state $\Psi_m = \{\bar{\epsilon}_1, \bar{\epsilon}_2, \bar{\epsilon}_3\}$. Data are normalized with respect to the response at $\Psi_0 = \bar{\epsilon}_4$ (blood).

Part I

SENSING FROM OUTSIDE

3

REQUIREMENTS AND FEASIBILITY: A CLINICAL CASE

This Chapter presents a feasibility study of a *passive body-centric system* for the wireless monitoring of human body movements in some common sleep disorders by means of passive tags equipped with inertial switches. Although the presented clinical case is rather specific and it is expected that each monitoring application requires its own parameters, some useful guidelines can be generally defined with the aim to provide a first-level reference for the design of future passive body-centric networks.

The monitoring of human subjects by means of passive RFID technology is a challenging problem from both medical and communication perspectives. Those issues must be faced by considering a systemic approach, in which all the requirements are together analyzed and fulfilled, eventually pointing out the weakness and the limitations. Innovative monitoring scenarios can be introduced, denoted as *passive body-centric systems*, whose feasibility is however questionable due to the poor robustness of the communication and the modest accuracy of the available passive sensors.

Interesting medical cases that could benefit of an RFID monitoring platform are the Restless Legs Syndrome (RLS) and the Periodic Limb Movements (PLM), common disorders affecting the sleep [24]. RLS is clinically characterized by a compelling urge to move the limbs, accompanied by uncomfortable and unpleasant sensations in the extremities, especially during periods of rest or

inactivity such as lying or sitting. Symptoms of RLS show a characteristic circadian evolution with a nocturnal worsening leading to insomnia and consequently daytime sleepiness and reduced quality of life.

During the sleep, RLS is often associated with repetitive unilateral or bilateral limbs movements referred to as PLM, defined in terms of duration, number and interval between movements. The movement is highly stereotyped and in its complete form resembles the so called triple response: extension of the great toe followed by a partial flexion of the ankle, knee and sometimes hip.

RLS is generally diagnosed by medical history while periodic limb movements must be diagnosed by polysomnography (PSG) or movement recording [25]. The analysis requires the establishment of the number of leg movements that meet PLM criteria occurring during sleep and during wakefulness, the number of events leading to arousal, the duration of the intervals between successive movements, the duration of the movements themselves and their occurrence.

At present [5], the most versatile diagnosis tool is the actigraph which embeds miniaturized accelerometers, a local memory and a processing unit within a bracelet- or watch-like packaging. This device is usually placed on the ankle or foot and monitors local acceleration. In spite of it only provides motion information, and cannot tell which muscle is generating the movement, the recorded data are useful for clinical purpose, with the great advantage to conduct the analysis in the patients' home environment.

This chapter discusses the feasibility of a completely new approach to monitor sleep disease, also suited to different motion analysis. The method is based on the emerging Radio Frequency Identification (RFID) technology and passive motion-detecting sensors. The purpose is to obtain very low-cost wireless devices, eventually single-usage, able to be attached onto the body segments to be controlled and to produce high-level aggregated data just ready for the clinical analysis.

The application of the RFID technology to the monitoring of limb movements (see a possible set-up in Fig.17) during the sleep is a rather new topic. It requires the integration of passive inertial

switches over the tag antenna, as in the enhanced passive UHF RFID proposed in [26], [27], but also presents the great challenge to design passive UHF tags suited to the human body. Here, the feasibility analysis considers the power sensitivity of the microchip transponder, the tag antenna design, the sensitivity and the time response of the inertial switch, the emitted electromagnetic power from the reader and the interrogation rate with respect to the read distance and the retrievable information about motion.

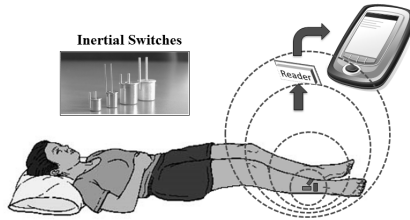


Figure 17: A possible set-up for the wireless monitoring of limbs' motion by RFID technology equipped with passive motion detecting sensors.

In order to fulfill both sensing and communication requirements, the study is here carried on by means of numerical simulations, based on both electromagnetic and mechanical tools and preliminary experimental validations.

3.1 SYSTEM ANALYSIS

The proposed monitoring method requires one or more UHF RFID tags equipped with inertial switches to be attached onto the patient's limbs or onto other body regions. As proposed in [26], [27], the switches react to the verse of the applied acceleration by changing their internal impedance from low (ideal short circuit) to high (ideally open circuit) impedance. A wireless one-axis sensor may be then achieved by means of a tag embedding two reverse-oriented inertial accelerometers (for instance see the scheme in Fig.20) which turn between two RFID microchip transponder so that only one of the two possible IDs is emitted. Such an ID may be

related to the acceleration's verse according to an ID modulation paradigm, as described later more in detail.

The tags are interrogated, according to a proper repetition rate, by an RFID reader placed somewhere in the patient's rooms, for instance on the side walls or, better, on the ceiling. The feasibility of this configuration is strictly correlated to the correct interrogation of the tags from a given distance, in accordance with the safety exposure regulations.

In this perspective it is important to define *i)* the key parameters of the Restless Sleep monitoring, *ii)* the minimum features required to the body-antenna design, *iii)* the number and the position of the tags, *iv)* the sensibility of the inertial switches and *v)* the energetic and safety constraints. These issues are now detailed analyzed in the following paragraphs.

3.1.1 *The Restless sleep key-parameters*

PLM are well defined in terms of duration, number and interval between movements. According to the operational definition of periodic limb movements given by the *World Association of Sleep Medicine* [28], the duration of a typical PLM event is about 0.5-5s and the time-elapsed between two consecutive events to be considered as PLM must be at least 5s and no more than 90s. Movements must occur in a sequence of required length and the number of consecutive candidate events matching the period criteria must be four in number or more. As suggested in [28] the most relevant parameters to monitor are the time duration of each PLM and their repetition rate all along the night. Fig.18 shows an example of actigraphic data during an episode of sleep disorder. It has been experimentally found that the quiet-state (normal sleep) acceleration is about 5mg (with $g=9.81 \text{ m/s}^2$), while during a PLM the acceleration may reach an average value of 0.2g. The WASM standards indicate the dynamics requested to the acceleration sensors to be [0.01-8g]. The same recommendation suggests a sampling rate of the motion capturing of $f_c \geq 10\text{Hz}$ and, typically, the conventional actigraphs consider two data sampling rate, at 1Hz and at 16 Hz, respectively.

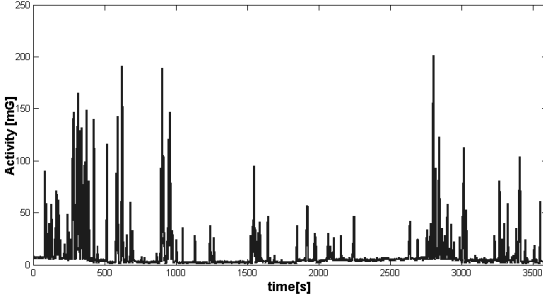


Figure 18: A typical actigraphic trace for PLM reporting the amplitude of the acceleration during 1h time interval and sampled at $f_C=1\text{Hz}$. Courtesy Neuroscience Lab, University General Hospital of Roma "Tor Vergata".

3.1.2 Tag sensitivity and useful read region

Being a passive device arvesting energy from the reader, an RFID tag is activated when the absorbed power exceeds the tag's microchip sensitivity threshold P_{chip} : $P_{R \rightarrow T} > P_{\text{chip}}$. From (2.1) the activation region of the reader, e.g. the places Ω_R where a tag collects enough energy to be activated, is

$$\Omega_R = \left\{ \underline{d} : \frac{P_{R \rightarrow T}}{P_{\text{chip}}} > 1 \right\} \quad (3.1)$$

and the maximum activation distance d_R for the tag is computed from (2.1) by enforcing $P_{R \rightarrow T} = P_{\text{chip}}$:

$$d_R = \max_{\theta, \phi} \left\{ \frac{\lambda_0}{4\pi} \sqrt{G_R(\theta, \phi) G_\tau(\theta, \phi) \frac{P_{\text{in}}}{P_{\text{chip}}} \eta_p} \right\} \quad (3.2)$$

The limb-worn tags have to be read within a typical hospital or domestic room under the constrain that the emitted field is compliant with the specific exposure limits. It is hence useful to introduce the concept of *forbidden region*, corresponding to a particular reader emission, as the place where the r.m.s. electric

field (averaged over a prescribed time interval T_{av}) is higher than the maximum r.m.s. value E_0 allowed by the local safety regulations. In general, the reader can interrogate the environment according to a given repetition period T_0 . Denoted with T_{com} the time duration of a typical reader-tag communication, the duty-cycle is $d_T = T_{com}/T_0$. The forbidden region is therefore

$$\Omega_F = \left\{ \underline{d} : \frac{\langle E(r) \rangle_{T_{av}}}{E_0} > 1 \right\} \quad (3.3)$$

where $\langle E(r) \rangle_{T_{av}} = \sqrt{d_T} E(r)_{r.m.s.}$ is the r.m.s. time-averaged reader's field.

The boundary $d_F(\theta, \phi)$ of Ω_F can be predicted with good accuracy just assuming free-space propagation e.g.

$$d_F(\theta, \phi) = \sqrt{30P_{in} G_R(\theta, \phi) d_T} / E_0 \quad (3.4)$$

with E_0 in r.m.s. unit, for instance $E_0 = 1.375\sqrt{f} = 41.3V/m$ according to the European Recommendation [29]. Even more restrictive constraints may be found in some Countries, as in the case of Italy where $E_0 = 6V/m$.

The electric parameters are therefore fixed so that the useful region for the patient is the hollow volume $\Omega_U = \Omega_R - \Omega_F$. Restrictive exposure limits imposes the use of a reduced emitted power (small forbidden region) and rather sensitive microchips (large read region). For instance, by designing tags with realized gain $G_{rT} = 0dB$ and sensitivity $P_{chip} = 30\mu W$ (-15dBm) and by using a reader emitting 3.2W EIRP (emission limit in Europe) in continuous mode ($d_T = 1$) hence $d_R = 6m$ and $d_F = 0.2m$ ($E_0 = 41.3V/m$). The useful region will have therefore maximum extension $d_R - d_F = 5.8m$, (4.5m for the more restrictive limit $E_0 = 6V/m$), which is reasonable to include a sleeping room. A worse performing tag's antenna, as expected for body-tags, needs to be compensated by a more sensitive chip.

3.1.3 Timing

On considering that the limb's motion is required to be sampled at rate f_c , the number of RFID microchips which may be interrogated are given by

$$N_C = \frac{d_T}{f_c T_{com}} \quad (3.5)$$

Under the assumptions: $f_c = 10\text{MHz}$, a typical duration of a reader-tag interrogation $T_{com} = 30\text{ms}$, and finally a duty cycle $d_T = 1$, then $N_C = 3.3$. Since only one of the two microchips placed in the tag will be responding (depending on the acceleration verse), the system timing will therefore permit to acquire the information of three tags which could be placed either onto a same limb, to collect the three-axis motion pattern, or onto different body segments such as the other limb and the thorax. Some realistic simulated examples will demonstrate later on that even a single axis monitoring will still provide useful overall data for medical considerations.

An inertial switch changes its impedance state, in reply to a motion stimulus, after a delay time t_{switch} which has to be smaller than the interrogation period $1/f_c=0.1\text{s}$. Typical commercial devices [30] show values $t_{switch} \simeq 0.01\text{s}$ which are hence compatible with the considered application.

3.2 COMMUNICATION PERFORMANCES IN REAL CONFIGURATIONS

Since the tag antenna has to guarantee the correct reader-tag communication during the whole sleep, when the body pose may change many times, it is important to analyze the communication performances in real configurations. Among typical sleep positions [31], the most threatening ones are those with joined legs since the tag could be subjected to higher losses and pattern distortion. The worst condition arises when the tag is sandwiched by the two arms and it may reasonably occur only if the tag is

placed in the inner part of the leg. Therefore it is opportune to place the tag onto the front or external surface.

The effective communication properties of the proposed system have been evaluated by using the set-up in Fig.19, comprising a long-range, remotely controlled reader CAEN A948, and a circular polarized patch antenna with 8dBi maximum gain. The measurement setup reproduces a typical medical scenario: a bed and a properly spaced RFID reader, e.g. placed on the ceiling. The wearable tag is a half-length slotted patch, detailed later in Chapter 4. To better understand the antenna performance, independently on the particular embedded sensor, the tag has been experimented without inertial switches, whose full characterization and integration will be described in Chapter 5. In successive measurements, the tag is placed on the middle of the left leg (in frontal position) and on the center of the thorax of a volunteer, and has been interrogated under typical sleep positions [31]. For each body pose the reader records the minimum Effective Isotropically Radiated Power ($EIRP=P_{in}G_R$) required to activate the tag and to collect a stable response. This is a useful indicator to discuss the feasibility of this system and to get an idea about the power margin to increase the read-distance in larger environments.

Tab.2 summarizes the activation EIRP and the estimated Effective Electric Field $\langle E(r)_{r.m.s.} \rangle_{T_{av}}$ from (3.4) in correspondence of the patient. The tag is efficiently readable in each case, even in the back position (B) and in presence of the second leg (C-D). The required activation powers and the relating fields are perfectly in accordance with the European Recommendations clarified in Sec.I, and even with the more penalizing Italian one. The minimum required EIRP corresponds to the tag placed on the torso, while the maximum power, as expected, is referred to the tagged leg partially covered by the other one. This pose is however not so common during the PLM episode since movements can be monolateral or bilateral, and the patient generally moves the legs separately. In a typical medical scenario a 3.2W EIRP would be more than enough to monitor the patient during all along the sleep, regardless his positions and his movements.

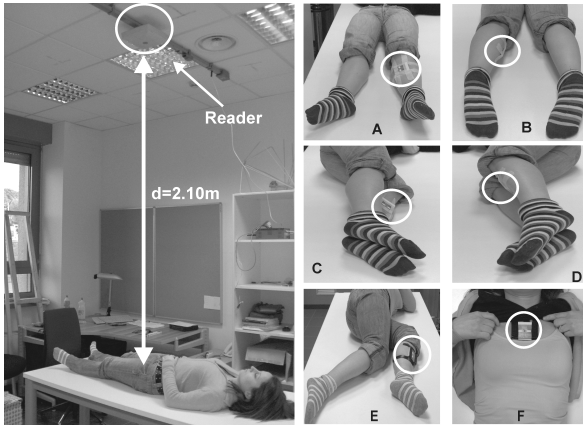


Figure 19: Top) Measurement setup comprising the long-range reader, the table and the patients. Bottom) Typical sleep positions (A-F). The antenna is placed in front of the left leg (A-E) and on the thorax (F).

It is important to report that simulations and tests have demonstrated that the antenna performances are adequate to the position of the tag on different body segments, thanks to the conductor folding which decouples the radiating part of the antenna from the tagged body. Such a tag is therefore a good candidate to the monitoring of other body motion patterns.

A possible packaging of the wearable tag with the inertial switches is sketched in Fig.20, where the arrows indicate the activation verse of the switch.

3.3 ESTIMATED BIOPHYSICAL SIGNALS BY USING A RADIO-MECHANICAL MODEL

Assuming now that the reader-tags links may be reliable during all along the sleep, a *radio-mechanical* model is here introduced to simulate the biophysical signals collected by the reader during the legs motion, and to discuss the effect of other system

Table 2: Effective Isotropically Radiated Power (EIRP) of the reader and Effective Electric Field in correspondence of the patient

Position	EIRP [W]	$\langle E(r) \rangle_{r.m.s}$ [V/m]
A	2.34	3.99
B	1.97	3.66
C	3.20	4.67
D	3.02	4.53
E	3.20	4.67
F	1.24	2.90

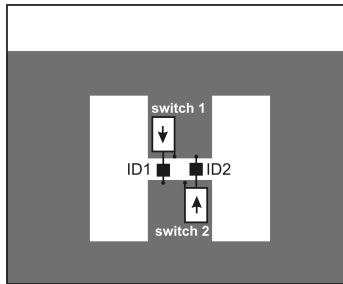


Figure 20: Example of integration between the wearable Antenna (front view), the inertial switches (white boxes) and two microchips (black boxes). The arrows indicate the preferred direction of the switches

parameters such as the inertial switch's threshold and the interrogation rate. The model includes a simplified human phantom having individually controllable 18 moving parts. By a preliminary analysis of maximum articular flexion and extension of the legs' segments, some typical motion patterns in PLM episodes have been reconstructed by enforcing the trajectory of hip, knee and foot. The movement has been computed by a multi-body cinematic simulation solver [32].

The numerical computation produces the vectorial acceleration at any part of the body. A four-events PLM episode (Fig.21),

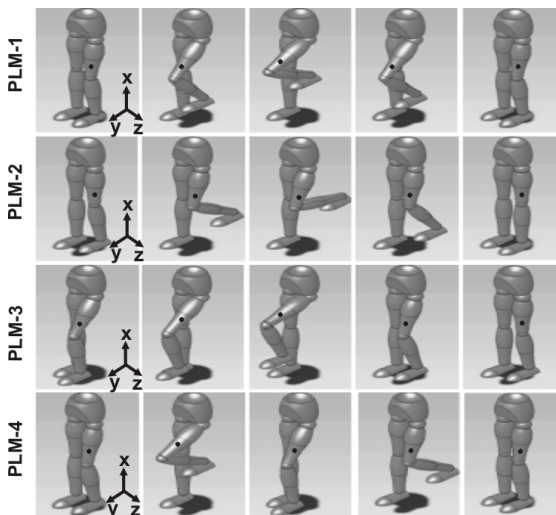


Figure 21: Motion patterns for four PLM episodes. To speed-up the cinematic computations, only the lower part of the phantom has been considered.

occurring within an interval of 50s, has been simulated. Since the considered events are flexions and extensions of ankle and knee around the transversal axis (z-axis), the motions take place only on x - y plane and hence only two tags are supposed to be used. Fig.22a gives the predicted acceleration of the leg at tags positions.

The one-axis accelerometer is simply modeled as an ideal switch, changing between a short circuit and a high impedance Z_{OC} , (ideally an open circuit), depending on the applied acceleration. The instantaneous transfer function of the switch included in the model is hence

$$Z_S^\mp(a_\xi) = Z_H U(a_S \pm a_\xi) \quad (3.6)$$

where ξ indicates a component of the applied acceleration, Z_S^\mp is the impedance of the switch oriented toward ξ^- or ξ^+ , $U(\cdot)$ is the Heaviside function and a_S the threshold acceleration. This

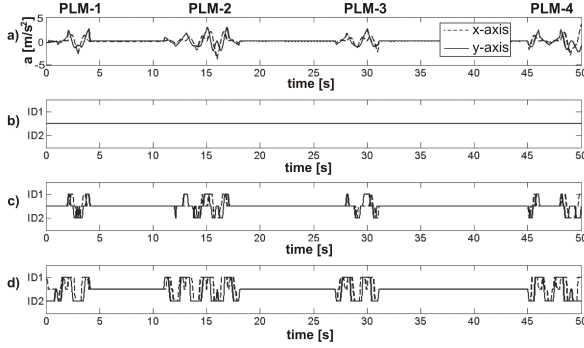


Figure 22: a) Leg's acceleration and ID-modulated received data for sampling rate $f_C=10\text{Hz}$ and three different of acceleration thresholds: b) $a_s=0.5g$; c) $a_s=0.1g$; d) $a_s=0.01g$.

model does not account for the switch's inertial delay since typical values of commercial device, as discussed in Section III.B, are much smaller than the duration of PLM episodes. The presence of the tag is accounted such that, when the leg is moving toward the positive ξ^+ ($a_\xi > a_s$), the switch 2 will be "closed", connecting the microchip 2 to the antenna port, while the switch 1 will be open and hence the reader will collect the only ID2 code. The converse holds in case of $a_\xi < -a_s$.

The ID-modulated data received by the reader are shown in Fig.22 and Fig.23 for different choices of the acceleration threshold a_s and of the interrogation frequency f_C . The particular choice of the parameter a_s affects the detection of low movements.

Interrogation at frequency $f_C = 1\text{Hz}$ can't correctly reproduce PLM movements (Fig.23), while having chosen $f_C = 5\text{Hz}$ it is instead possible to collect useful data about the number of PLM, their duration and the time elapsed between two consecutive events. At this frequency it is also possible, from (3.5), to interrogate up to $N_C = 6$ tags and hence to earn three-axis information in two distinct body regions.

To better discuss these results, a temporal index for the PLM, e.g. the time duration of each PLM, has been computed as the

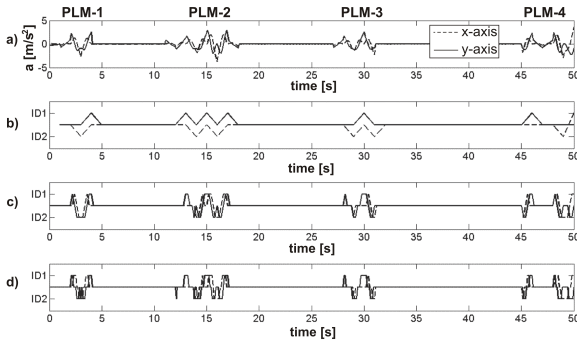


Figure 23: a) Leg's acceleration and ID-modulated received data for switch's acceleration threshold $a_s=0.1g$ and some interrogation frequency: b) $f_C=1\text{Hz}$; c) $f_C=5\text{Hz}$; d) $f_C=10\text{Hz}$

time-interval between the first and the last ID transition of each PLM. With reference to Tab.3 it can be observed that:

- i)* each tag is able to correctly capture the dynamics in term of number of predicted PML frequency and approximate duration
- ii)* a simple one-axis tag seems to be enough to capture the relevant features of the physical phenomenon.
- iii)* an acceleration threshold $a_s = 0.1g$ is enough to give an approximate estimation of the event duration.

Some commercial devices [33] show values $a_s = 0.1g$ which are hence compatible with the considered application.

Alternatively, in order to detect just the motion of the legs without information about its pattern, it is possible to consider a single tag equipped with an omnidirectional accelerometer instead of three tags with a couple of reverse-oriented unidirectional switches. In this case the sensor activates the tag response for any movement, and the two events collected by the reader will be: null ID (motionless leg) and tag's ID (leg in motion) or vice-versa. This is a simplified and a much less costly version of the proposed system, useful for the diagnosis of all the neuromuscular diseases that require the detection of the movement more than its evolution.

Table 3: Estimated PLM duration for different switch threshold and interrogation rate

PLM	T_{PLM}	$f_c = 5\text{Hz}$		$f_c = 10\text{Hz}$	
		0.1G	0.01G	0.1G	0.01G
1	4.1 s	$T_x=2.4$	4.0	2.5	4.0
		$T_y=3.0$	4.2	3.0	4.0
2	7.0	4.0	6.8	4.0	6.8
		5.2	7.0	6.0	7.0
3	4.0	3.2	4.0	2.5	3.8
		3.8	4.0	3.8	4.0
4	5.5	5.0	5.0	4.7	5.0
		5.0	5.0	5.0	5.1

A realization of such a motion sensor will be shown in Chapter 5.

3.4 CONCLUSION

This study theoretically demonstrates that the RFID monitoring of human motion, and in particular of the legs in sleep diseases, seems to be feasible within the actual technology and regulation constraints. As it will be later on detailed, the proposed wearable antenna permits to host the motion sensors and seems to be a good candidate to the monitoring of people in conventional indoor area.

Using only passive components it possible to obtain very low-cost wireless devices, eventually single-usage. The tag could be printed on flexible substrates and attached onto the body segments by standard band-aids.

Moreover the proposed monitoring strategy has various degrees of freedom which may be used to collect further information about the patient's state during the night, such as position and complex movements, by using additional tags equipped with inertial sensors placed on his torso or shoulder. This is a supplementary

feature of the proposed system that can help clinicians making differential diagnosis of the disease.

4

RFID WEARABLE TAG AND BODY CENTRIC COMMUNICATION

This Chapter introduces and discusses a new tag geometry suitable to be worn on the human body through numerical analysis and extensive experimentation. Several realizations will be presented with different sizes and materials, suitable to be placed on any part of the body. Extensive experimentation demonstrate that both on-body and off-body links are affordable with a power budget fully compliant with the available technology. The experiments permits to identify the most efficient tag placements and to propose some quantitative and general guidelines useful to characterize and design this kind of new systems.

The requirements of wearable RFID tags are small dimensions and light-weight as well as high immunity to the human body interaction which may otherwise sensibly change the radiation diagram and degrade the antenna efficiency. Some of these issues are also common to the design of tags for metal objects whose presence strongly affects the radiation diagrams of the attached antenna and prevents the use of dipole like layouts.

In active and semi-active architectures, as in the case of body-centric communication systems [34], the overall radiation performance is enhanced by additional battery-assisted electronics. In case of passive tags instead, where the energy to produce the response comes from a remote query unit, the antenna design is much more challenging.

Several solutions have been recently investigated for the design of passive tags over metals, mainly based on the use of high permittivity slabs and of metallic shields, integrated in the antennas as ground planes. Typical antennas are the patch-like family comprising PIFA and IFA layouts, [35] (maximum gain up to 6dB using the parasitic constructive effect of the surrounding objects), [36] (gain max: -2dB) [37] (gain max: -6.4dB).

The design of wearable passive UHF tags has up to now received much less attention. In [23] the family of slot antennas over a suspended patch, partly decoupled from the body by a silicone slab is considered. The study was mostly oriented to define tuning mechanisms for the required conjugate impedance matching to a great variety of microchip impedances and to understand the dependence of the antennas's bandwidth on the body placement. The antenna layout was intended to host additional electronics and contacting or non-contacting sensors. The maximum size of these antennas was of the order of 4-6cm and the typical gain was rather poor (gain max: -7dB) due to the bidirectional radiation of the slot. The expected activation ranges were therefore modest, even if it was demonstrated that the gain may be improved by enlarging the overall size. In [38] the use of automatically optimized slot-line transformers was further investigated for miniaturization and multi-band purposes.

The rich study in [39] considers some solutions partly decoupled from the body such as multi-folded dipole antennas over a shielding plate and regular patch and PIFA configurations. These devices are specifically designed for wearable applications and experimentally evaluated for what concerns the monitoring of runners in open areas and of personnel inside buildings. Some interesting effects are characterized, such as the influence of the tilt of the transmitting and received antennas and the mutual shadowing among people in the same area. The various antennas are not intended to host sensors but only to identify the person. The dominant size in all the cases was around 15cm and the measured on-body gain ranges between 0dB and 5dB in the largest configurations.

Very recently, new magnetic materials have been considered as shielding plates for RFID tags [40]. The innovative ferrite-silicone

(*BaCo*) composite promises to achieve very low-profile miniaturized and flexible structures potentially useful for wearable applications. The measured maximum gain in air is of the order of $-7\text{dB} \div -4\text{dB}$.

In this thesis a planar layout which combines the tuning agility of the shaped-slot based tags and the decoupling from the body achieved by grounded antennas has been considered. The basic configuration comprises a folded patch sourced by an embedded H-slot whose main features are: on-body gain higher than previous examples in [23] and comparable with that of tags over metal, approximately constant radiation performances regardless of the different body positions, reduced sizes and the predisposition to host passive sensors. A general design procedure is here described to apply the proposed antenna configuration to RFID microchips of given input impedance by the help of an equivalent circuit model useful to better understand the electromagnetic role of the antenna's geometrical parameters and to provide a starting guess in the final tag design. Four different prototypes will be realized and experimentally characterized in real scenario in term of input impedance and read-region characterization when the antenna plus the RFID microchip is attached onto the human body. Finally, an articulated experimental campaign is aimed to understand the achievable read ranges, the minimum number of required tags and their most suitable positions over the body for reliable *on-body* and *off-body* links. Human activity and shadowing effects will be also taken into account in order to understand the possibility to establish robust and safe communications.

Even if the results are expected to be strictly dependent on the specific environment and on the power consumption of the RFID microchip transponder, some useful normalizations are introduced with the aim to provide first-level guidelines for the design of future passive *Body centric* networks.

4.1 ANTENNA LAYOUT AND DESIGN PROCEDURES

A rectangular plate is folded (Fig.24) around a dielectric slab of height h_5 and the longest face is placed over the body through an optional dielectric insulator slab of thickness h_1 . Unlike the

shunt-fed conventional PIFA, this geometry can be viewed as a series-fed "L"-patch. An optional strategy to further improve the decoupling with the body, could be the design of a lower plate slightly wider than the upper one ($W_g > W$ and $L_g > L$). The RFID microchip will be attached in the middle of the slot's central gap.

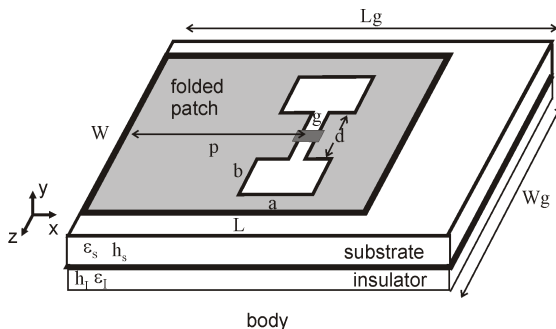


Figure 24: Layout of the proposed tag family. The H-slot acts as tuning impedance. The sensors may be allocated over the top conductor.

The radiation (Fig.25) is produced mostly by the slot and the patch's open edge. Assuming that the thickness h_s of the inner dielectric is small compared with the wavelength, the radiation from the folding may be considered negligible and the gain and matching features of the antenna are mainly related to the slot and to the transmission line truncation. The polarization is linear, parallel to the antenna main-direction (x axis in the figure).

As for conventional patches, the increase in the horizontal size W produces a gain enhancement. Depending on the position of the tag on the body, and on the available space, it is possible to increase that dimension in order to achieve better radiation performance. The length L of the patch is chosen approximately equal to $\lambda/4$, where λ is the effective wavelength in the dielectric substrate. While the size of the slot's central gap is mainly fixed by the microchip packaging and by the eventual sensing electronics,

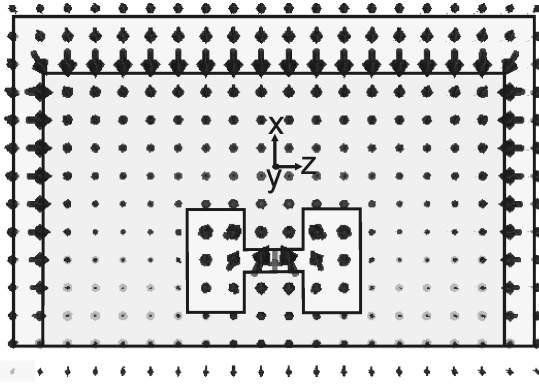


Figure 25: Near field distribution of the proposed wearable antenna. The radiation is maximum in correspondence of the central slot and the open edge (in opposite phase) and minimum close to the folding. As for conventional patches the fields along the external vertical sides (x axis in the figure) are in opposite phase, thus do not greatly contribute to the radiation.

different shape-factors and positions may be instead considered for the matching slot.

The maximization of the read distance requires the antenna impedance Z_A to match the conjugate microchip impedance Z_{chip}^* . To understand the role of the many geometrical variables on the antenna impedance and to achieve a starting guess for the design, an equivalent circuit and a parametric study are here presented.

4.1.1 Circuit model

Under the hypothesis that the antenna's lower plate is considered as an ideal infinite ground plane the input impedance of the wearable antenna can be predicted by the equivalent circuit in Fig.26. The above assumption is reasonable if the lower plate is a little larger than the upper antenna face hosting the microchip transponder. It is worth anticipating that both simulative and experimental considerations, to be presented later on, will demon-

strate that the antenna's performance is very little sensitive to the placement on different parts of the body thanks to the previously discussed decoupling mechanisms.

The structure is therefore analyzed as a microstrip transmission line truncated by a non-ideal open circuit at the first termination, by a short circuit at the other one and loaded in series by a complex-impedance element: the H-slot. A transformer's turn ratio n_p accounts for the coupling of the H-slot to the rectangular plate.

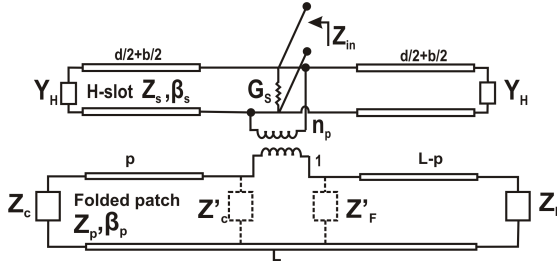


Figure 26: Equivalent transmission line model of folded patch loaded by the H-slot. Each part of the antenna is modeled as an equivalent impedance/admittance: Z_C for the short circuit, Z_F for the non ideal open circuit, Y_H and G_S for the slot, coupled by the transformer's turn ratio n_p .

The non ideal open circuit produces fringing field, as in conventional patch antennas and can be accounted for by an open-ended slot with equivalent parallel admittance $Y_F = G_F + jB_F$ [41] given by

$$G_F = \frac{W}{120\lambda_0} \left[1 - \frac{1}{24} (k_0 \cdot h_s)^2 \right] \quad (4.1)$$

$$B_F = \frac{W}{120\lambda_0} [1 - 0.636 \ln(k_0 \cdot h_s)]$$

The other short-circuit truncation of the antenna can be roughly modeled as an inductance [42]

$$L_c = h_s \cdot \left(0.2 \left[\log \left(\frac{2h_s}{W+t} \right) + 0.2235 \left(\frac{W+t}{h_s} \right) + 0.5 \right] \right) \quad (4.2)$$

where t is the thickness of the conductive sheet.

The H-slot could be viewed as the combination of three portions of slot-lines. The horizontal $(d + 2\frac{b}{2}) \times g$ slot is mainly associated with the coupling and the radiation through a conductance [41]

$$G_S = \frac{d}{120\lambda_0} \left[1 - \frac{1}{24} (k_0 \cdot g)^2 \right] \quad (4.3)$$

The two identical vertical longitudinal short-circuit slot-lines of width b and length a , as described in [43], host phase-reversal aperture fields, and hence they mainly store reactive energy. The effect of each vertical $b \times a$ slot is accounted for by the series admittance Y_H of two short-circuit stubs of length $a/2$, e.g.

$$Y_H = -\frac{1}{2} j Y_S \cot(\beta_s a/2) \quad (4.4)$$

where Y_S and β_S are the characteristic impedance and the wave number of the slot-line with width a calculated as in [43].

Denoting with Y'_c and Y'_f the admittance of the microstrip's shorted- and open-ended termination, after transfer up to the microchip connection, and Y'_H the vertical-slot admittance (Y_H) again transferred at the center of the slot, the total input impedance of the antenna is finally given by

$$Z_{in} = \frac{n_p^2 (Z'_c + Z'_f)}{1 + n_p^2 (Y'_H + G_S)(Z'_c + Z'_f)} \quad (4.5)$$

with $Z'_c = (Y'_c)^{-1}$, $Z'_f = (Y'_f)^{-1}$. The transformer's turn ratio n_p is related to various antenna's parameters such as the slot size and its position along the upper patch. n_p is roughly equal to the fraction of the current intercepted by the aperture to the total

antenna current and can be calculated numerically, for instance as described in [44], or by means of best fitting of the numerically computed input impedance to the circuital expression in (4.5). Just for example, Fig.27 shows the dependence $n_p(a, p)$ in the case of PTFE inner dielectric ($\epsilon_1 = 2.08$, $\tan\delta = 4 \cdot 10^{-4}$) and having fixed the other sizes deduced by an FDTD-simulation [45] of the whole structure.

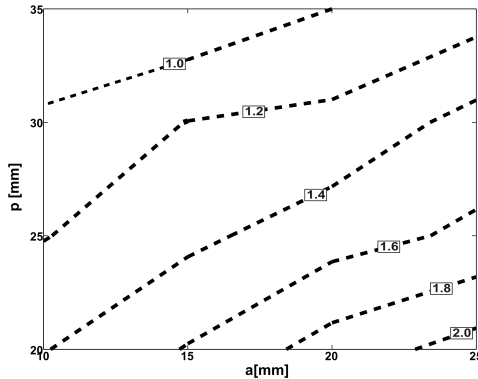


Figure 27: Variation of the transformer's turn ratio n_p of the circuit model with respect to the slot dimension a and its position p , having fixed (size in [mm]) $L = 46.5$, $W = 80$, $b = 3$, $d = 10$, $g = 2$.

As expected, the amount of current intercepted by the H-slot, and thus the n_p ratio, increase for large slots; moreover it is maximum when the slot is close to the left folding ($p = 20\text{mm}$) and minimum in proximity of the metal plate's open-circuit truncation ($p = 35\text{mm}$). The variation of the turn ratio is well approximated by a bilinear polynomial fitting (with respect to a and p [mm])

$$n_p \approx 2.184 + 0.0328a - 0.0530p \quad (4.6)$$

4.1.2 Parametric Analysis

Fig.28 and Fig.29 show the variation of the tag's input impedance versus the position p and versus the shape factor of the matching

slot (modified by acting only on the parameter a) when the inner dielectric is again the PTFE with the same thickness as before. The antenna reactance is inductive before the first resonance and hence this configuration is suited to achieve conjugate matching to the capacitive impedance of the microchip. Moreover, the resistance and reactance change in an opposite way with respect to p and a , e.g. the antenna impedance increases (the resonance moves to the lower frequencies) as the slot moves closer to the folding (p reduces) while it reduces (the resonance moves to the higher frequencies) as the H-slot becomes narrower (parameter a reduces). The tag design may therefore concentrate on the optimization of the only $\{a, p\}$ parameters having fixed the remaining ones.

The insets of Fig.28 and Fig.29 show the good agreement in the European RFID band of the impedance estimations from circuit model with fullwave FDTD simulation of the planar antenna. The expression in (4.5) can be therefore used to give a first approximation for slot's sizes and position such to achieve the impedance matching with the microchip, in view of using a fullwave electromagnetic solver to refine the geometrical parameters.

4.2 PROTOTYPES AND PERFORMANCES IN REAL CONFIGURATIONS

Four different prototypes of this class of tags have been designed, fabricated and tested in real conditions. In every case, the antennas' matching is referred to a low impedance NXP microchip transponder with impedance $Z_{\text{chip}} = 15 - j135\Omega$ and power sensitivity $P_{\text{chip}} = -15\text{dBm}$. The final antenna design has been refined by including into the FDTD simulation also a stratified rough model of human body segment, such a limb or torso (parameters in Tab.4 for the limb). The prototypes differ for sizes and materials: in two of them the inner dielectric is PTFE, the other two are instead flexible and build on felt.

Two different experimental characterizations of the tags' performances are here presented. The antenna design is first checked in *chipless* modality by the measurement of input impedance Z_A used to calculate the power transmission coefficient τ in (2.3). The RFID link performance is instead fully analyzed having attached

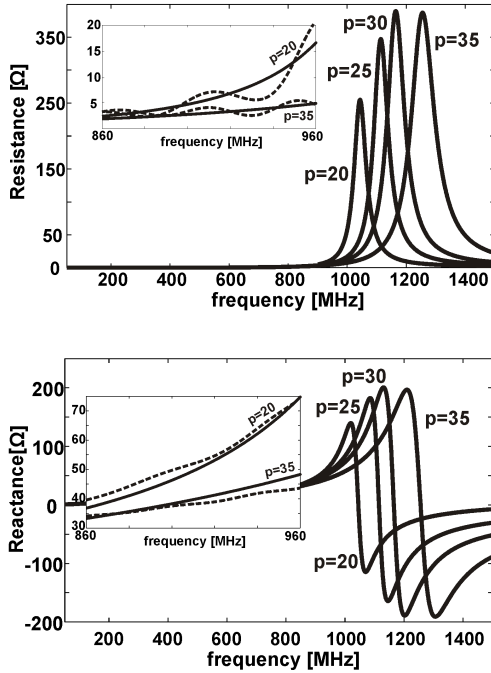


Figure 28: Parametric exploration of input impedance for various slot positions in x direction (Fig.24), having fixed (size in [mm]) $L = 46.5$, $W = 80$, $a = 20$, $b = 3$, $d = 10$, $g = 2$. Continuous lines tag the circuit data while the dashed lines indicate the fullwave results.

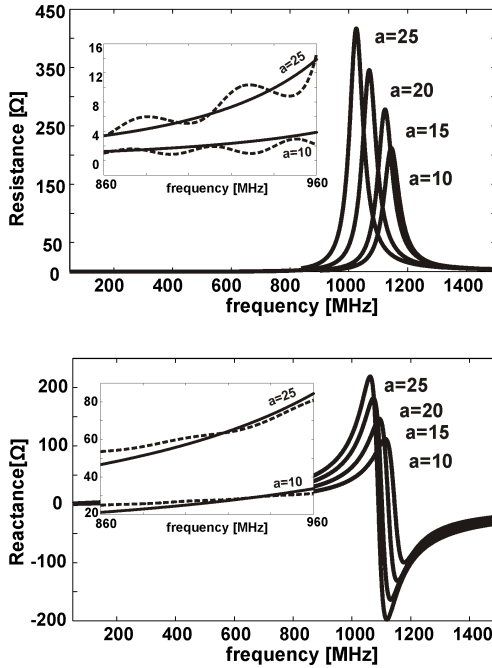


Figure 29: Parametric exploration of the input impedance for various slot form factors (selected by the parameter a), having fixed (size in [mm]) $L = 46.5$, $W = 80$, $p = 25$, $b = 3$, $d = 10$, $g = 2$. Continuous lines tag the circuit data while the dashed lines indicate the fullwave results.

the microchip at the antenna port and by estimating the maximum read-distance in controlled conditions, i.e by measuring the realized gain G_{τ} in (2.6)

Table 4: Parameters of the simplified limb model at 870 MHz

Layer	ϵ_r	σ [S/m]	Cross section [cm]
skin + fat	14.5	0.25	12×11
muscle	55.1	0.33	10×9
bone	20.8	0.33	4×2

4.2.1 PTFE tags

The resulting fabricated prototypes, of overall size 6×6 cm (TAG-1) and 6×9 cm (TAG-2), (other parameters in Tab.5) are shown in Fig.30. The insulating dielectric, contacting the body, is a thin adhesive PVC film.

Table 5: Parameters of the tag prototypes in [mm]

Parameter	TAG-1	TAG-2
W_g	60	90
W	60	80
L_g	49	60
L	49	49
p	$L/2$	15
a	8	18
b	10	9
d	10	10
g	3	4
h_s	4	4

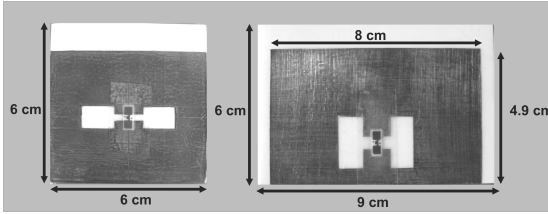


Figure 30: Fabricated TAG-1 (left) and TAG-2 (right) prototypes of body-worn antenna matched to $Z_{in} = 15 - j135 \Omega$ microchip.

TAG-2 is expected to have a higher gain in comparison with TAG-1 ($G_{2,max} = 0\text{dB}$ v.s. $G_{1,max} = -3\text{dB}$, as estimated by FDTD) thanks to the larger W , and to the wider ground plane which prevents the antenna radiation to be absorbed into the highly-dissipative human body.

The tags' impedance has been measured by means of a Vector Network Analyzer, VNA (Anritsu MS2024A) probe connected to the slot mid-point through a bazoooka balun having the purpose to prevent unbalanced currents from the probe to flow on the outer surface of the coaxial cable. [41]. An approximately $\lambda/4$ metal sleeve, shorted at one termination encapsulates the coaxial probe (Fig.31). The input impedance measured by the VNA will be hence the tag impedance itself without artifacts. As a proof, Fig.32, shows a comparison between the simulated tag without cable and balun, and the also simulated impedance in the measurement condition. As visible the input impedance of the tag plus the balun, estimated by FDTD, is practically unchanged, at least in the RFID band, with respect to the stand-alone antenna.

The antenna has been attached over the leg of a volunteer and the measurement of impedance, after de-embedding of the coaxial connector, gives a power transmission coefficient (at 869MHz) of the order of $\tau \simeq 0.7$ (TAG-1) and $\tau \simeq 0.85$ (TAG-2) (Fig.33). It is worth mentioning that nearly identical results are obtained when the tags are placed onto different body segments, such as the torso and the arm, as shown in the next paragraph concerning the measurement of the realized gain.

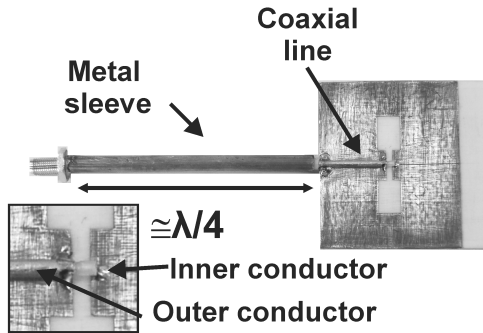


Figure 31: Antenna plus balun connection. The external conductor of the coaxial line, coming out of the balun, is soldered to the antenna face up to the slot, while the internal conductor is soldered to the other slot's edge.

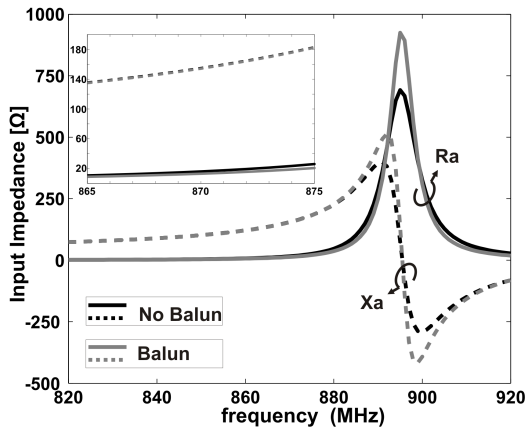


Figure 32: FDTD simulated input impedance of TAG-1 with and without the presence of the balun

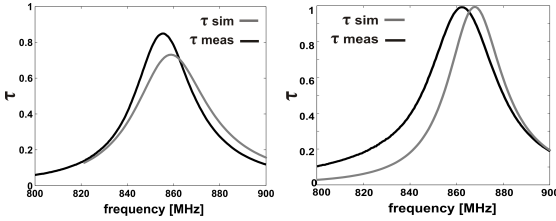


Figure 33: Simulated and measured power transmission coefficient τ for the two antennas matched to $Z_{\text{chip}} = 15 - j135$. Left) TAG-1. Right) TAG-2.

The realized gain of the tags, e.g. the radiation gain of the antenna reduced by the impedance mismatch, has been indirectly estimated for TAG-1 and TAG-2 by using the set-up in Fig.34 comprising a short-range, remotely controlled reader CAEN A528, and a quarter-lambda patch (PIFA) with maximum gain 3.3dB, as reader's antenna. The realized gain is measured by means of the turn-on method [22] starting from the knowledge of the reader gain G_R , the reader-tag distance d , the polarization mismatch η_p between the reader and the tag (here set to $1/2$) and finally the turn-on power $P_{\text{in}}^{\text{to}}$. In this case by increasing the reader's power until the tag starts to respond, the collected power at turn-on equals the chip sensitivity, $P_{R \rightarrow T} = P_{\text{chip}}$, and hence the realized gain can be estimated by inverting (2.1), when all the other parameters are known.

Equation (2.1) has been verified to hold also in a real environment if the measurement set-up is far from the side walls, the distance d is small enough ($d < 1\text{m}$) and absorbing panels are placed on the ground to reduce multipath.

The measured G_τ is shown in Fig.35 and Fig.36 for the tags placed onto two different body regions, the torso and the left arm. The tags are attached onto the body such that the antenna polarization (x axis in Fig.24) is parallel to the body's longitudinal axis. G_τ has been evaluated along the two principals directions (y - and z -axis in the figures) by body rotation of 90° , 180° and 270° . As expected, the realized gain is maximum in front of the antenna while it is minimum in the rear side, due to the human

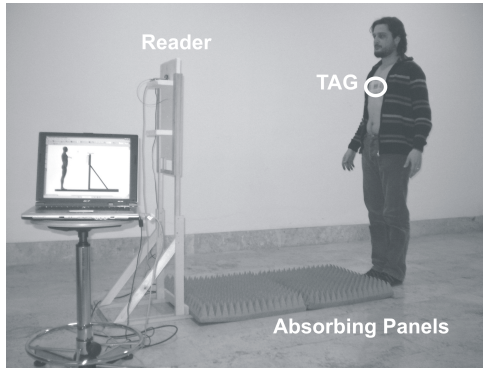


Figure 34: Measurement setup comprising the short-range reader, the measurement trick and the absorbing panels. The antenna is here placed in the center of the human torso.

body absorption. However both tags are readable in the back direction when placed on the arms.

The maximum effective gain for the TAG-1 ranges between -4dB and -3dB depending on the body positions, while better performances are achieved by TAG-2, thanks to its larger size, with maximum realized gain ranging between -2dB and -1dB . These results are in full agreement with the design data. The radiation performance is hence nearly the same for the two positions, confirming that the antenna is very little sensitive to the body position. It is worth mentioning that the tags still retain similar performance in free space conditions.

The experienced maximum read distance, by using the short-range reader (emitting not more than 0.5W EIRP), and tags' microchip with typical $P_{\text{chip}} = -30\text{dBm}$, was 1.5m for the TAG-1 and 2.1m for the TAG-2. However, by using a long-range reader (emitting up to 3.2W EIRP) the maximum read distance estimated from (2.1) could reach 4m for the smaller design and 5.5m for the larger one.

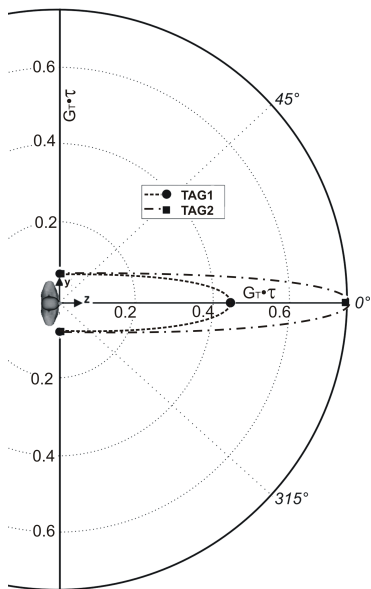


Figure 35: Measured G_τ for the antenna placed on the torso of the volunteer (top view schematically represented in the origin of the polar graph).

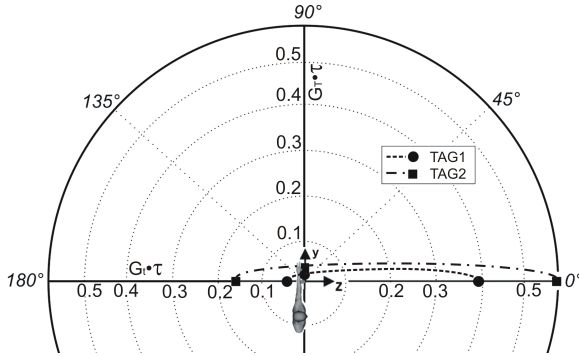


Figure 36: Measured G_{τ} for the antenna placed on the left arm of the volunteer (top view schematically represented in the origin of the polar graph).

4.2.2 Flexible tags

Two textile versions of the wearable tag has been developed. The teflon substrate is replaced by a 3mm-thick synthetic felt (Fig.37) and the conductors are made by carved adhesive copper. Due to the variability of manufacturing processes, the dielectric properties of the felt are not really assessed in the UHF band ([34], [46], [47]), and hence the electromagnetic features of our felt sample have been experimentally evaluated by means of a specific parameter-identification technique using numerical models and measurements on planar antennas. The resulting permittivity and conductivity at the European RFID frequency 870MHz are $\epsilon = 1.17$ and $\sigma = 2 \cdot 10^{-4} \text{S/m}$, to be compared with the published values $\{\epsilon = 1.1\}$ in [47] and $\{\epsilon = 1.38, \tan\delta = 0.0023\text{S/m}\}$ in [48], both at 2.45GHz. The resulting fabricated prototypes have 7×9 cm (7.5 g weight) and 5×5 (3 g weight) cm overall sizes.

Also the flexible tags have been characterized in term of realized gain. Tag A is placed on the torso of a volunteer while Tag B on the wrist. In both cases they are in the front of the reader's antenna, at 1.3m from ground. Ground reflections are minimized by using absorbing panels (Fig.38).

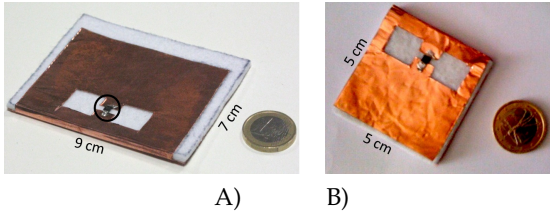


Figure 37: Textile wearable tag prototypes made by felt and adhesive copper. Size in [mm]: A) $L=59$, $W=80$; $a=15$, $b=15$, $p=14$, $d=10$; $L_g=70$, $g=3$, $h_s=3$, $W_g=90$, B) $L=48$, $W=48$; $a=13$, $b=13$, $p=12$, $d=10$; $L_g=50$, $g=3$, $h_s=3$, $W_g=50$.

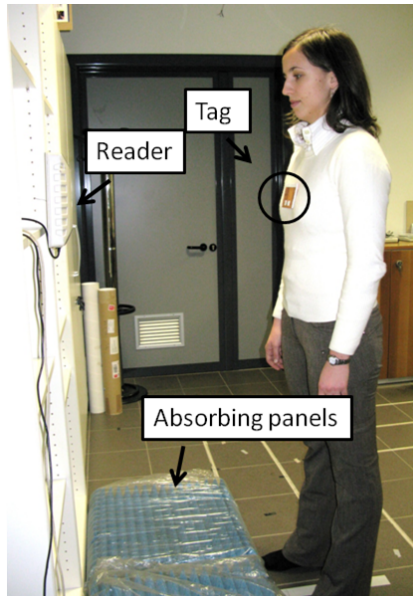


Figure 38: Measurement setup for tag's realized gain comprising the reader, the volunteer and the absorbing panels. The antenna is here placed in the center of the human torso (Tag A) or on the wrist (Tag B).

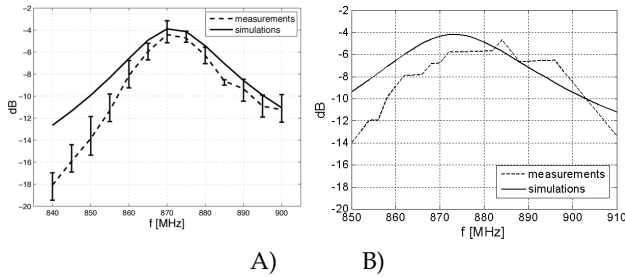


Figure 39: Maximum realized gain for the wearable tag placed on the human torso (A) and on the wrist (B), as measured along the tag boresight. The vertical segments give the data variability in repeated measurements.

The frequency-dependent measured realized gain referred to the frontal direction is shown in Fig.39 (tags and reader's antenna are aligned).

The maximum gain, at the European frequency 869MHz, ranges between -5dB and -4dB and is hence fully comparable with the previous teflon prototype ($-4\text{dB} < G_{\tau} < -3\text{dB}$). It is interesting to notice that, although the smaller size, the radiation performances of TAG B are similar to the ones of TAG A. This effect could be explained with the different interaction of the field radiated by the slot and the patch's open edge, since, as previously described, they are in opposite phase and thus tend to reduce the overall antenna radiation. In TAG B the ratio L/L_g is smaller compared to TAG A, the fringe field lines tend to flow into the human body and thus the radiation is expected to be lower. In such a way the radiation reduction, due to the opposite phase of the radiating elements, is limited.

It is worth mentioning that nearly identical results are obtained when the tag is placed onto different body segments, as the back and the arm.

4.3 BODYCENTRIC COMMUNICATION

As in more mature active bodycentric systems, interesting RFID communication modalities can involve *on-body* and *off-body* links. The off-body communication could be useful for example to locate and monitor people inside buildings by means of fixed readers placed in different rooms or by a wearable reader and ambient-disseminated tags [49]. A possible application is the access control in dangerous or restricted areas. The on-body communication is instead typical of unusual scenarios where a fixed communication infrastructure is missing. It could be the case of a sportsman, a soldier or a fireman equipped with different RFID sensors (inside his garment) interrogated by his hand-held standard communicator in harsh environments [50], [51]. In both types of link the presence of the human body must be taken into account in order to understand and reduce the phenomena of scattering and power absorption and evaluate the compliance with the International Regulations on the electromagnetic exposure and Specific Absorption Rate (SAR) limits [52], [53].

4.3.1 *Off-body communications*

In the off-body communications the most relevant parameters to study are the reading range of the tag in a real environment, depending on its position over the body, and the minimum number of tags and readers to achieve a reliable interrogation of the subject.

The read range of the wearable tag will be measured according to the following bodycentric procedure. Definitely, it is of interest to discriminate the region surrounding the tagged human body wherein, anyway placed a reader, at least a tag is successfully interrogated. It is expected that such a region will depend on the position of the tag over the body and on the reader-emitted power as well as on the reader antenna's pattern. Like the previous Teflon prototype, also the textile tag, thanks to the presence of the ground plane, revealed very little sensitive to the body position in term of impedance matching and maximum gain. Nevertheless, the shape of the read region may be dependent on such a position

due to the specific shadowing caused by body segments themselves and by absorption modality. Hence to discuss this issue, three different tag placements are considered (front torso, arm and back) each in horizontal and vertical orientation as shown in Fig.42. All the measurement have been conducted with the flexible tag A.

For the sake of simplicity, the read region is measured in a reciprocal way, e.g. the reader is fixed in some place of the room, while the tagged person walks away from the reader along the boresight of the reader's antenna (see Fig.40). The actual reader-body distance is considered as belonging to the read region of the tag if this one is able to correctly reply to the reader's interrogation. The procedure is repeated for rotations of $\{0, 90, 180, 270\}$ degrees of the body with respect to the reader's antenna.

The measurements are performed into a $5.5\text{m} \times 5.5\text{m} \times 3\text{m}$ of-office room, having removed the inner furnitures. The same reader's antenna and long-range reader as before, are placed at the middle of a side wall, 1.3m from the floor. The reader emits a fixed power 3.2W EIRP which is the maximum value allowed by the European Regulation. The space sampling rate is 30cm.

In general, the read-range in real environments is affected by the presence of walls and furniture in a way which is also dependent on the reader's power and microchip sensitivity. All these issues have been extensively addressed in [49] but it is useful to recall that in case of low-gain tags, as for the wearable textile patch, the effect of the side walls of the room here considered can be neglected. Hence, the results in the following Sections may be extended to different environments by introducing the two-rays correction terms as in [49].

An example of measurement is given in Fig.41, where the solid dots indicate a successful interrogation of the tag when the person stands at that point. The empty circles, instead, represent a reading failure. By considering that the transition between the read region and the unreachable region is not sharp, due to the formation of diffraction fringes [49], the following metrics is assumed to define the maximum read distance $d_{\text{max}}(\phi_n)$ in a given direction $\phi = \phi_n$. The distance $d_{\text{max}}(\phi_n)$ is calculated from the human body to the first point of fault interrogation (empty circle) followed

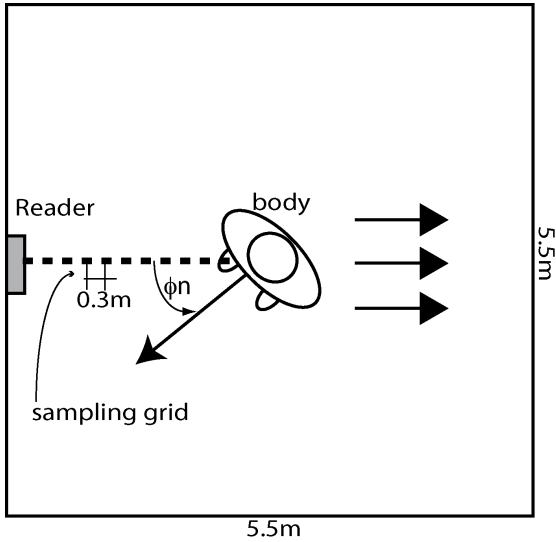


Figure 40: Reader-tag mutual orientations during measurements to evaluate the extension of the bodycentric reading region. The volunteer equipped with a wearable tag walks away from the reader's antenna which is placed onto the middle of a wall inside a $5.5\text{m} \times 5.5\text{m} \times 3\text{m}$ room, at 1.3 m from the floor. The tag is interrogated when the volunteer is standing at the dotted positions, by 30cm steps. Each point is said to be accessible by the RFID system if the tag is able to answer the reader. The experiment is repeated for four orientations of the body with respect to the reader's antenna, e.g. for $\phi_n = 0, 90, 180, 270$ degrees to collect the 2D reading range.

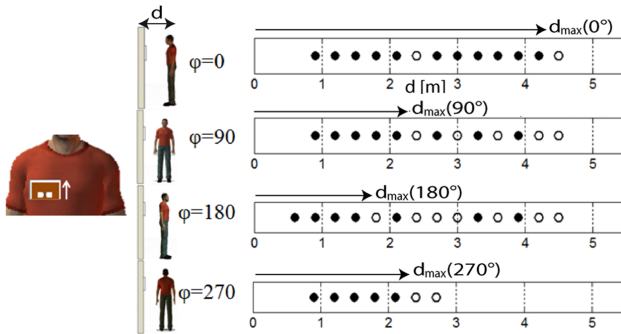


Figure 41: Example of read region measurements when the tag is placed over the torso with vertical polarization. For each reader-body orientation, the filled circle indicates a successful reading of the tag in that point while the empty circle indicates a reading failure. The maximum read distance d_{\max} along each direction is calculated from the human body to the first point of fault interrogation followed by less than two consecutive points of successful interrogation.

by less than two consecutive points of successful interrogation (filled circles). In other words we positively value even the very isolated failure points, in consideration that the subject could be moving and so he could still be statistically detected with an overall continuity.

The results of the measurement campaign are represented in a compact form in Fig.42. The overall maximum read distance is about 5m, arising in the case E (tag over arms with horizontal orientation). In most of the considered configurations the maximum distance is about 4.5m, confirming that the maximum gain of the antenna is very little sensitive to the position over the body. The read distances out of the antenna's boresight are instead dependent on the dielectric losses of the human body that produce significant absorption and shadowing, especially in the case of shoulder-placed tags. The polarization of the tag, e.g. the orientation of the radiating edge of the patch, seems to play a significant role in the achievable read ranges, even if the physical reasons are not immediately clear. Vertical polarization is far better per-

forming in the case of placement over chest, while horizontal polarization appears more suitable for placement over shoulders and arms.

In none of the considered tag placements it is however possible to achieve a nearly uniform coverage with just a single tag. By a combined use of tags it is however expected to achieve a reliable RFID link, for instance by placing one tag over the torso and the other over the back (A+H) or a single tag for each arm (F(right) + F(left)). The combined results are shown in Fig.43 where nearly circular bodycentric interrogation regions are visible. These diagrams represent the area in which, wherever is placed a reader emitting 3.2W EIRP in front of the person, it is possible to monitor the subject independently from his position and orientation. Even better results may be achieved by using three tags: two of them over both the arms and one over the chest.

In conclusion, a single reader permits to establish a reliable RFID link with a person equipped with a two- or three-tags within a room of size 4m by 4m. Four readers, each placed onto each side wall, would instead enable the continuous interrogation within a four-times larger (9m by 9m) room.

The above results have been obtained for a particular choice of the reader's power and of the family of microchips. However, such data can be also useful in case of different choices of power parameters by introducing the *effective microchip's sensitivity* [49], an aggregate performance indicator for the tag defined as:

$$p_{\text{chip}} = \frac{P_{\text{chip}}}{G_{\tau}} \quad (4.7)$$

which gives the minimum radiofrequency power that the tag has to collect to exhibit the same averaged free-space read distance as a perfectly-matched tag placed over a lossless object (averaged $G_{\tau} = 1$). In our particular case $p_{\text{chip}} = 90\mu\text{W}$. Since from (2.6) the maximum read distance is linearly dependent on the ratio $\sqrt{\text{EIRP}/p_{\text{chip}}}$, where $\text{EIRP} = G_{\text{R}}P_{\text{in}}$, an estimation of the read range $d_{\text{max}} \left(\frac{\text{EIRP}}{p_{\text{chip}}} \right)$ with a different choice of power and microchip's sensitivity may be roughly deduced from the values of

Position				
	$\phi=0^\circ$	$\phi=90^\circ$	$\phi=180^\circ$	$\phi=270^\circ$
A	4.2	2.1	1.5	2.1
B	1.8	3.3	0.6	1.5
C	2.1	2.1	2.1	1.5
D	4.2	3.6	1.2	0.6
E	5.1	2.7	2.4	0.6
F	4.5	4.5	3.3	-
G	-	4.5	4.8	2.1
H	-	4.5	4.5	3.6

Figure 42: Read distances (in meter) measured at four different angles from the torax's normal axis, for several positions and orientation of the body-worn tag.

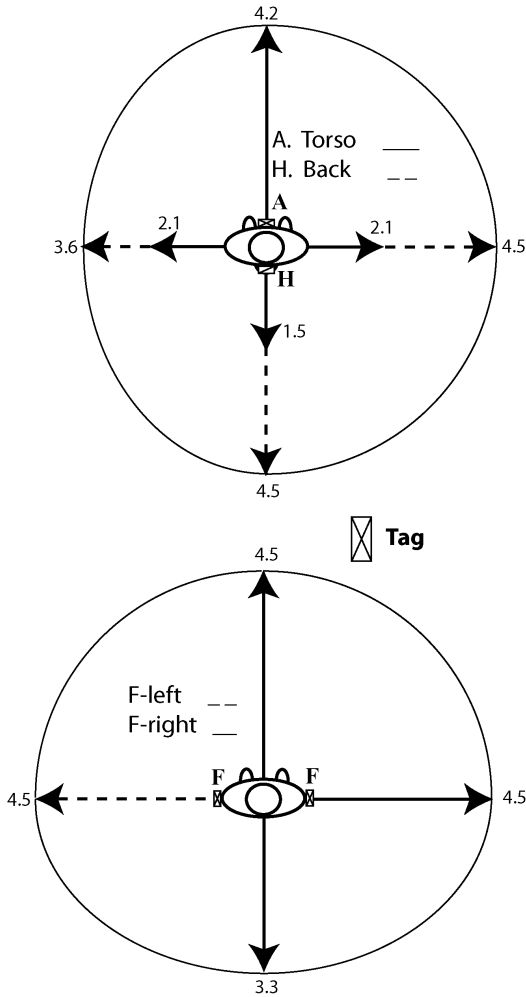


Figure 43: Bodycentric reading regions for two couplets of tags placed on the human body. Up) tags over front torso and shoulders (case A and H in Fig.42). Down) tags over both the arms (case F in Fig.42). Continuous and dashed arrows indicate the maximum read distance $d_{max}(\phi_n)$ of the two tags in the specific direction and the ellipse-like regions gives the estimate of the overall resulting bodycentric reading region for the combined two-tags system.

the read distances given here (now denoted as $d_{\max,0}(\hat{r}_n)$) by means of the following formula

$$d_{\max} \left(\frac{\text{EIRP}}{P_{\text{chip}}} \right) = 5.6 \cdot 10^{-3} d_{\max,0} \sqrt{\frac{\text{EIRP}}{P_{\text{chip}}}} \quad (4.8)$$

4.3.2 On-body communications

In case of on-body communication it is of interest to analyze, in addition to the tag placements, also the effects of body posture and activity on the link shadowing. Depending on the reader-tag position, different propagation phenomena are excited [54]: creeping waves can be predominant for communications between adjacent body segments (waist-torso, arm-forearm) while diffracted and reflected free-space waves could be considered responsible for the communication between distant regions, such as arm-leg, head-waist etc. In both cases it is not appropriate to consider the typical far-field approximation. The quality of the established links can be hence characterized according to the turn-on power $P_{\text{in}}^{\text{to}}$ enabling the activation of the tag in the specific position, and according to the percentage of successfully interrogations. In order to provide a general performance indicator like (4.7), the turn-on power is here normalized by the microchip effective sensitivity P_{chip} :

$$p^{\text{to}} = 10^{-3} \frac{P_{\text{in}}^{\text{to}}}{P_{\text{chip}}} \quad (4.9)$$

Such a parameter could be hence considered as a kind of “transfer function” of the system: the lower is p^{to} , the more efficient and reliable is the link.

In this second measurement campaign, the reader’s antenna is a smaller linear polarized quarter-lambda patch (PIFA) with maximum 3.3dB gain, that is suited for placement onto the volunteer’s body, close to the waist. Also the reader unit is attached onto the body (Fig.44).

The PIFA interrogates five wearable tags attached on the torso, arm, head, leg and wrist, respectively. To improve polarization matching, the PIFA is oriented so that its polarization vector is always parallel to that of the tags in all the experiments.

During the measurements the volunteer takes twenty different "static" (1-14) and "moving" (15-16) postures, illustrated in Fig.45. The last four positions correspond to the subject lying on the ground and could be representative of particularly dangerous situations, such as faintings or accidents.

Measurement results are reported in Tab.6. In our specific case, by considering the same microchip sensitivity as before, the turn-on power ranges between 8dBm (corresponding to $p^{to} = 0.07$) for the link A and 29dBm ($p^{to} = 9.24$) for the link C. As expected, thanks to the smallest and stable distance, the most efficient link is that involving the tag over the front torso (Link A). Independently on the different postures and movements, it requires the minimum activation power and it is little sensitive to the shadowing effects of the body. The link E (waist-wrist) is instead the most sensitive to the mismatch polarization and to the shadowing produced by body movements: in postures 9 and 12 the tag placed on the wrist results even un-readable. Among lying positions, recumbent posture (18) is the most challenging one to establish an RFID link due to the close presence of the ground within the reader-tag link. In this case the required turn-on power is two-orders of magnitude higher than the standing positions. It is moreover worth observing that the two side-lying postures (19 and 20) yield completely different turn-on powers due to the asymmetric position of reader/tags over the body and to the combined shadowing effects of floor and arms.

Some statistics are then presented having performed N_R interrogations of tag A and D in the 20 postures with a fixed reader's power of $P_{in}=20dBm$ such that at least the links A, D are fully active.

The parameter of interest is here the percentage of answer α , defined as

$$\alpha = \frac{N_T}{N_R} \times 100 \quad (4.10)$$

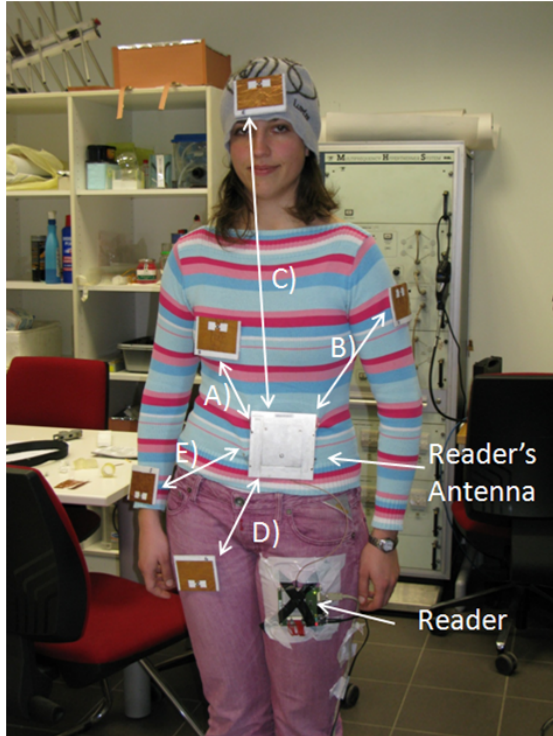


Figure 44: Antenna positions on the body. Five different links are here considered. The short-range reader is placed in the waist slightly on the left.

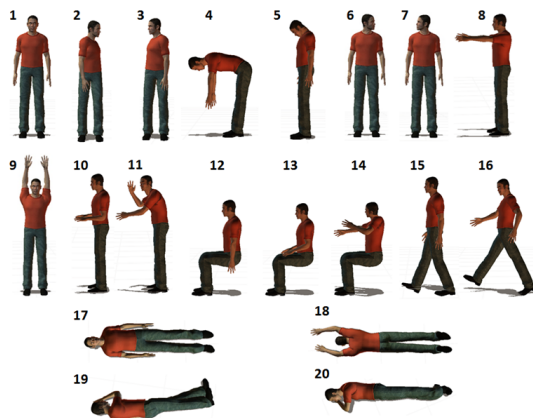


Figure 45: Postures assumed by the subject during the measurements. In the first fourteen the subject stands or sits in different positions according to typical human activities. Two postures (15 and 16) are in motions while in the last four the subjects lies on the floor simulating healthy and pathological conditions, such as the later safety position (LSP)



Figure 46: Channel reliability α for several postures, expressed in term of percentage of answer with the antennas in vertical polarization.

The reader is set to perform 9 polls per second, each interrogation period is 10s and hence $N_R = 90$, while N_T is the count of responses to those polls. Both vertical and horizontal tags' orientations are considered and, as above, the PIFA is properly rotated to preserve the polarization matching. The results are shown in Fig.46 and Fig.47 for the vertical and horizontal orientations of the antennas.

The link A is rather robust, with a percentage of correct answer exceeding 70% almost in each case. The link D is instead much more sensitive to the human activity, with lower percentage of answer sometimes close to zero. Mutual orientation between reader's antenna and wearable tags affects the reliability of the links. It is apparent that the link A exhibits best performance in case of vertical-polarization set-up since both reader's antenna and tag are oriented along the directions of maximum radiation, e.g. the radiating edges of the two patches are mutually facing. Link D instead, for the same effect as before, appears better performing in case of horizontal polarization. In any case the lying positions are the most reliable due to the high variability of the body segments' position. Except for the supine posture, the statistics of the readings can be very unstable in the other configurations,

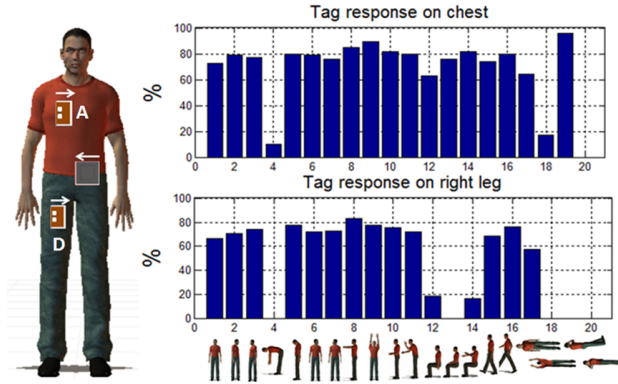


Figure 47: As in Fig.46 but with the antennas in horizontal orientation.

regardless of the required activation power. Also in these cases the torso-waist channels results the most efficient.

4.3.3 Safety Issue

In order to discuss the compliance of the wearable system with the exposure limits, some issues concerning the Specific Absorption Rate (SAR) and the radiated electromagnetic field, are here discussed for the on-body and the off-body setups, by the help of numeric electromagnetic simulations. In the first case, the same FDTD torso model previously adopted for the design of the wearable antenna is now applied to estimate the resulting SAR distribution at 870MHz, averaged over 10g of tissue. The reader's PIFA antenna is placed on the middle of the external surface of the cylinder and radiates a fixed 0.5W power, as in the on-body experiments. The diagrams in Fig.48, for both vertical and horizontal placements of the PIFA, have to be compared with the considered SAR limit of 2W/Kg [55]. As expected, the maximum SAR occurs underneath the antenna, in correspondence of the muscular tissue, but it is one order of magnitude smaller than the absorption limit. This means that the cohabitation of the reader's PIFA with the body is safe even in case of the maximum emitted

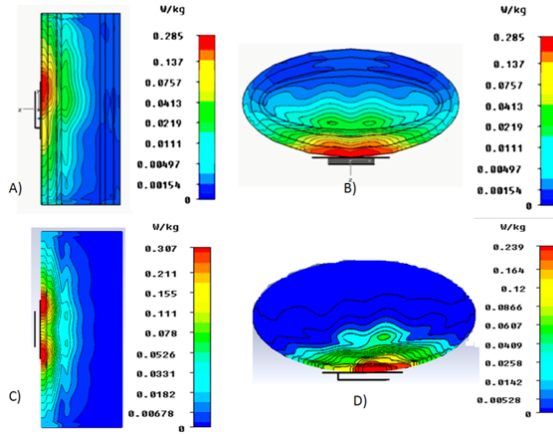


Figure 48: Specific Absorption Rate (SAR) [W/Kg] of the human torso model wearing the reader's PIFA antenna in vertical polarization (case A and B) and horizontal polarization (case C and D).

power allowed by European (3.2W EIRP) and US (4.0W EIRP) regulations. For what concerns the off-body communication, the experimented read distance is simply discussed with respect to the maximum limit E_0 imposed to the field radiated by the reader. The study in [49] addressed this topic by introducing a forbidden region all around the reader, wherein the emitted field strength exceeds the allowed limit and hence no person should be present inside for more than a given time specific for the local regulation. In particular, the simulations in [49] show that even in case the reader radiates 3.2W EIRP, the extension of the forbidden region is less than 50cm for $E_0 \leq 20\text{V/m}$. Moreover, such a distance is practically further reduced in case of duty cycles $d < 1$. For instance, assuming a typical inventory communication between reader and tag with ten interrogations per second, the resulting forbidden distance will be halved with respect to the case of continuous interrogation. Therefore, the off-body link is fully compatible with local regulation for body-tag distances larger than a small fraction of meter.

4.4 CONCLUSION

The analytic model and the detailed experimentations have demonstrated that the proposed family of wearable tags is a good candidate to the monitoring of people in conventional indoor and outdoor area. Thanks to the particular folded geometry, the structure is not much influenced by the detuning and by the absorbing effects produced by the human body. Thanks to the slot, it offers some degree of freedom in the impedance matching, useful to integrate passive sensors.

The presented tests demonstrate that passive bodycentric RFID links are feasible within a regular indoor room with the today available technology. Actually, the on-body link may be established using a query power of the order of just 10dBm in case of the tag is placed over the torso and the reader's antenna on the waist. This power requirement is compatible with pico-readers as well as with conventional hand-held radios and even with smartphones. Moreover, the continuous improvement in microchip sensitivity will permit to extend the reading distance or, conversely, to reduce the required powers. New pervasive applications may be therefore envisaged where low-cost and even disposable wearable tags will interact with multi-services radio devices.

The position of the tags over the body has to be carefully chosen in order to avoid shadowing and excessive absorption. A single tag is not enough to establish an omnidirectional off-body link, while two or three tags placed over the chest, the shoulders or over the arms permit to interact with the moving body from any angle and with remarkable reproducibility.

Finally, the backscattered power level in on-body configurations undergoes fluctuations with amplitude of 1 up to 4dB depending on the position and on the motion. This issue has to be carefully taken into account in sensing applications based on the RSSI processing.

Table 6: Normalized turn-on power p^{to} for postures in Fig.9 and on-body RFID links in Fig.8.

Normalized turn on Power					
Posture	Link A	Link B	Link C	Link D	Link E
1	0.08	0.44	0.56	0.39	0.62
2	0.05	1.76	0.55	0.62	1.4
3	0.09	2.79	1.76	0.5	1.4
4	0.04	3.51	1.11	0.35	1.76
5	0.1	0.35	0.35	0.62	0.62
6	0.09	0.7	0.88	0.62	0.62
7	0.08	0.35	1.11	0.39	0.79
8	0.07	1.4	0.7	0.62	4.42
9	0.09	4.96	0.44	0.7	-
10	0.05	0.99	0.56	0.99	0.5
11	0.05	0.57	0.44	0.39	0.39
12	0.04	0.4	0.7	0.35	-
13	0.04	0.35	0.88	0.62	0.39
14	0.05	0.62	0.25	0.25	0.44
15	0.05	0.5	0.39	0.44	0.49
16	0.05	0.35	0.44	0.28	0.44
17	0.08	1.25	0.7	0.41	8.23
18	5.57	-	9.24	-	-
19	0.08	6.54	0.88	0.33	1.25
20	0.1	0.92	1.11	0.79	-

5

MONITORING OF BODY ACTIVITY: MOTION AND DEFORMATION

The chapter describes how to use RFID passive technology to monitor the human movements and the body deformation.

For the motion two approaches will be discussed: loaded-tag and sensor-less sensing.

A complete sensor-less approach is instead adopted for the monitoring of deformation.

One of the most important parameters in the Human Healthcare Monitoring scenario is the human activity. Unexpected falls, inactivity or hyperactivity, movements during sleep, breath rhythm and posture can be, for example, easily related to physiological and pathological conditions and give essential information about the state of the subject. The goal of activity recognition is to determine the actions or the states of one or more subjects through the analysis of sensor data from ambient sensors or on-body sensors. Ambient sensors are particularly useful for monitoring environments in which the subjects move. Body-worn sensors instead can be used to monitor one person and classify his or her actions. A combination of ambient and on-body sensors can finally give more complete information, allowing the detection and the classification of behavior and life patterns, particularly useful in case of elderly and chronic disease patients.

The detection of the motion, in particular, is of great interest in medical application, to assist the diagnosis of some neurological diseases, involving compulsory arms movements [25], in domestic healthcare, to track the behavior of elderly, but also in logistic and

security to control limited-access areas. Body-attached sensing devices with accelerometer, gyroscope and other sensing units are widely used. They are relatively low cost, portable and required less processing than video-based activity recognition approaches. However the design of wearable systems is complicated because of limited size, weight, and power consumption requirements. These drawbacks limit also their widespread diffusion, making that class of device quite intrusive and not much user friendly. The RFID technology, taking advantage from its "invisible" nature, could be instead a valid solution. At this purpose two different strategies will be introduced, discussed and experimentally tested. The first one consist in using passive accelerometers properly integrated into the wearable tag, while the second one requires a proper processing the power backscattered by the tag toward the reader, thus without specific sensor.

Strictly related to the human activity is then the possibility to monitor deformations and variations of shape (for example elongation and contraction) of muscles or body segments, during movements and breaths. The field of application are countless, from the sport to the rehabilitation and the monitoring of physical activity for patients who have suffered a stroke, multiple sclerosis, joint replacements, or reconstructions, amputation, brain, and spinal cord injury, or some motor function disability resulting from Parkinson's disease. RFID passive technology may offer a complete low-cost and off-the-shelf solution thanks to the availability of microchips transponder which digitally encode the signal transmitted back to the reader while preserving the analog electromagnetic interaction with the tagged item. A first example of strain-sensing tag was proposed in [56] where the antenna was printed over a stretchable substrate whose deformation produces a modification of the microstructure of the conductive ink and thus of the overall conductivity. However no attempt was done to control and increase the sensitivity during the antenna design.

A different and fully controllable layout is here proposed, for the UHF (868-956 MHz) RFID band, even if the same ideas may be naturally extended to higher frequencies, with improved resolution. The device is based onto a meander line antenna able to change its shape and consequently its radiation performances

depending on the experienced deformation. A parametric analysis will show that it is possible to shape the sensitivity and the dynamic range of the RFID strain sensor by a proper choice of few geometrical parameters. The idea is finally demonstrated through a working prototype subjected to controlled stress.

5.1 MONITORING OF MOTION BY MEANS OF LOADED TAG

It is here shown how the design procedure of wearable tag can be modified to take the presence of a specific sensor into account. As an example, a very simple mechanical motion sensor is considered, and a fully integrated wearable sensor RFID tag is designed, fabricated and hence experimentally evaluated.

5.1.1 *Omnidirectional motion sensor*

The sensor used here is a two terminal omnidirectional switch (Fig. 49) especially designed for the detection of movements and vibrations [57]. When disturbed from its quite condition, it produces fleeting changes of its equivalent impedance state, e.g. open to close or vice versa, and if properly conditioned to the antenna microchip, it may consequently enable or deny the RFID communication. One of the two pins of the steel-gold plated capsule is connected to the external case of the sensor while the other one is isolated from the outer part of the capsule and connected to the inner switching structure (Fig. 49 c). The switching structure comprises a dumbbell-like conductive element connected to the central pin and a conductive sphere, free to move inside the capsule.

The sensor has two possible states Ψ (see Fig.50) . In state A the internal sphere touches at a same time the inner and the outer conductors of the sensor thus shorting the output pins. In state B, the sphere does not connect the structures and the circuit remains approximately open. State A is stable while state B is unstable: at rest the switch is preferably in state A and during the movement it randomly changes between A and B varying its input impedance.

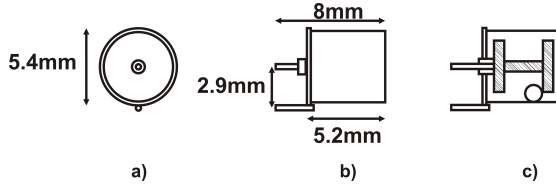


Figure 49: MS24M motion-vibration sensor design. a) Bottom view; b) Side view; c) Longitudinal section with the inner conductive structure and the switch mass [57].

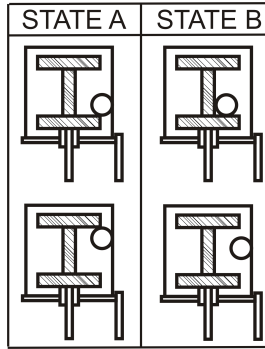


Figure 50: MS24M motion-vibration sensor state

The sensor will be connected in series to the microchip and hence the antenna design requires to properly account for the presence of the sensor, e.g. the conjugate matching condition in (2.16) becomes

$$Z_T(\Psi_m = A) = Z_A + Z_S(A) = Z_{\text{chip}}^* \quad (5.1)$$

In this choice, the reader will receive the tag ID when the tag is at rest $\Psi_m = A$ and does not receive anything if the tag is subjected to motion. The basic principle is a form of ID-modulation introduced in [26].

The RF impedance of the switch is not provided by the manufacturer and hence it has been measured with a VNA probe

connected to the switch by means of a modified SMA connector (Fig.51 inset). To avoid the unbalancing effects of the VNA coaxial cable, the capsule has been soldered directly all along the connector flange and its central pin has been inserted in the SMA inner conductor.

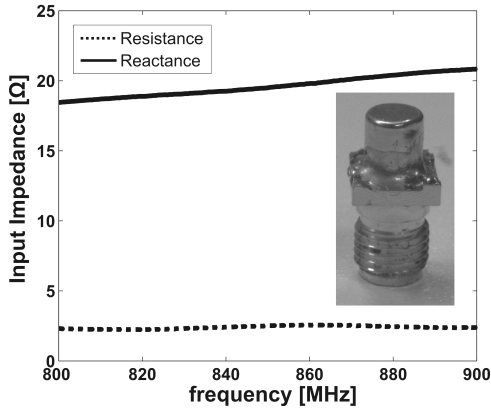


Figure 51: Measured input Impedance of the motion sensor measured with a VNA probe connected to the switch by means of a modified SMA connector.

At rest (ideally a short circuit), the sensor's measured impedance at 870MHz is $Z_s(\text{State A}) \approx 2.5 + j20 \Omega$, therefore showing a practically inductive reactance. The switch's impedance in state B is not easily measurable. During the motion, the sphere randomly moves inside the capsule varying the sensor's impedance without regularity. Basically when the sphere does not touch the sensor walls the resulting impedance is expected to be capacitive with value depending on the instantaneous sphere-wall distance.

5.1.2 RFID Motion Sensor prototype

A prototype of the wearable Motion Sensor (Fig.52) comprises a modified version of the TAG-2 described in Chapter 4, with a slightly different slot size in order to achieve the matching

condition in (5.1) having considered the sensor in series to the chip. It is worth noticing that the slot tuning has been accomplished by varying the only slot shape factor (the vertical dimension $a = 16\text{mm}$ has been changed from 18mm to 16mm), leaving unaltered all the other parameters. In order to easily solder the inertial switch, a packaged version of the microchip ($Z_{\text{chip}} = 15 - j135$) has been used instead of the strap version.

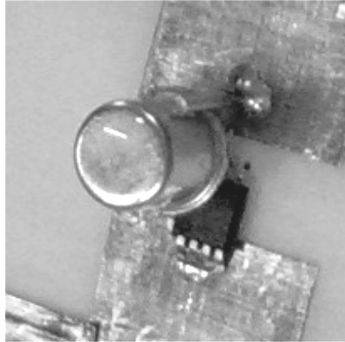


Figure 52: Particular of the prototype of the TAG-2 Motion Sensor. The inertial switch has been soldered in series to the microchip within the slot central gap.

5.1.3 Experimentation and Results

The proposed RFID motion sensor has been tested in real conditions in order to verify the effective communication and sensing performances. The movements have been also recorded by 3-axis MEMS motion sensor (LIS302DL [58]), able to measure the accelerations on the three orthogonal axis up to $2g$ (with $g = 9.8\text{m/s}^2$ gravitational acceleration) with a sampling rate up to 400Hz . The MEMS sensor has been placed behind the RFID tag in order to be affected by the same acceleration of the RFID device.

The measurement setup is visible in Fig.53. Both MEMS sensor and RFID Motion sensor have been placed on the arm and a sixteen-movements sequence has been executed moving the

arm randomly. Fig. 54 shows the module of the recorded MEMS sensor vectorial data (a) and the on/off data received at the reader (b), where the bars indicate the state B (motion). The reader-tag distance and the interrogation power are such that the RFID link may be in principle established for any position of the arm.



Figure 53: Measurement setup comprising the short-range reader, the RFID tag and the LIS302DL accelerometer placed beside the tag. Both the RFID motion sensor and the accelerometer are placed on the arm. The MEMS accelerometer data is transmitted via a WIFI module.

A significant correlation is visible between the two motion sensors, in term of number of movements, time and duration. In particular, the RFID Motion Sensor is able to monitor every body event, regardless its standing or magnitude.

Breath monitoring

A particular application of the proposed sensing platform is the monitoring of the breath activity. When placed onto the chest, the motion sensor is able to detect deep breaths and cough. This feature opens many interesting healthcare applications, in particular for the safety of operators in hazardous environments, for the monitoring of some sleep diseases and in sporting scenario.

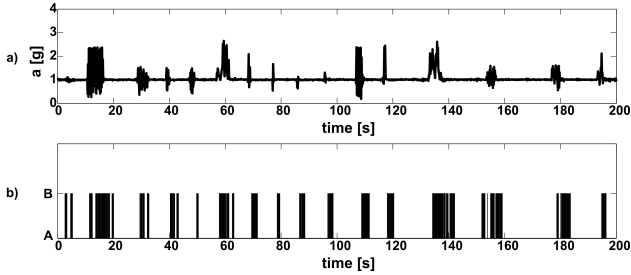


Figure 54: Comparison of data returned by the LIS302DL accelerometer (a) with the tag response received from the TAG2 Motion Sensor (b): the motion events (state B), for which the microchip does not respond, are indicated by bars.

Fig.55 shows the signals transmitted by the wearable motion sensor during the monitoring of deep breath. A sequence of 20 deep breath events is perfectly recognizable, demonstrating the validity of the proposed approach.

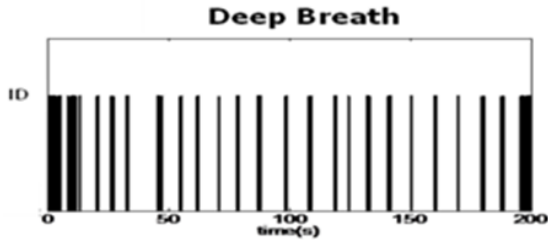


Figure 55: A sequence of 20 deep breath events correctly recognized with the tag placed onto the chest

5.2 MONITORING OF ACTIVITY BY MEANS OF SENSOR-LESS APPROACH

Processing the backscattered signals emitted by tags for Radio Frequency Identification (RFID) is a promising means to achieve passive low-cost sensing of things. Several examples have been

proposed in the very last years [22], [59], demonstrating the use of RFID tags as “*sensor-less*” sensing devices with fully controllable response.

The on-body configurations A, D and E in Chapter 4 Fig.44 are here characterized also in terms of the backscattered power $P_{R \leftarrow T}$ received by the reader. This quantity is in general less critical than the turn-on power in view to establish the quality of the RFID link since the communication bottleneck is the forward link. Nevertheless there are some emerging applications wherein the variation of the backscattered power is correlated to some physical property of the tag, and, in turn, to the change of the tagged object or of the nearby environment, with the purpose to achieve a sort of RFID passive sensing. This is the case when the tag is coupled to a chemical sensitive substrate detecting the presence of gases or when the antenna itself is deformed by motion[60].

At this purpose, three rather common postures of on-body communication are here considered with the aim to analyze the expected fluctuations of the received signals and an eventual correlation with the motion periodicity. In the first posture the subject stands up motionless at position 1 (see Fig.45). In the second one, instead, the person walks along a straight path inside a corridor with controlled steps: first a slow walking (60 cm/s per second) and then a faster motion (120 cm/s). In the third posture the subject folds the arm up and down. The same setup as in Chapter 4 is used in the three experiments. The input power to the reader is fixed to $P_{in} = 20\text{dBm}$. The backscattered power is deduced from the RSSI (Received Signal Strength Indicator) provided by the reader by means of the following conversion equation (specific for that reader)

$$P_{R \leftarrow T} = 0.8\text{RSSI} + 24 - G_{LNA} - 96 - 0.8\text{RSSI}_{th} \quad (5.2)$$

with $\text{RSSI}_{\text{th}} = 48$ and G_{LNA} gain of the low noise signal amplifier, defined in the communication register. For generality, the backscattered power (2.2) is normalized by the input power:

$$p_{\text{BS}} = \frac{P_{\text{R} \leftarrow \text{T}}}{P_{\text{in}}} \quad (5.3)$$

Fig.56 shows that the fluctuation of the p_{BS} for both the links are comparable, and are of the order of $\pm 1\text{dB}$ around the average value. This indetermination needs to be carefully taken into account to estimate the dynamic range of any sensing application based on RSSI processing.

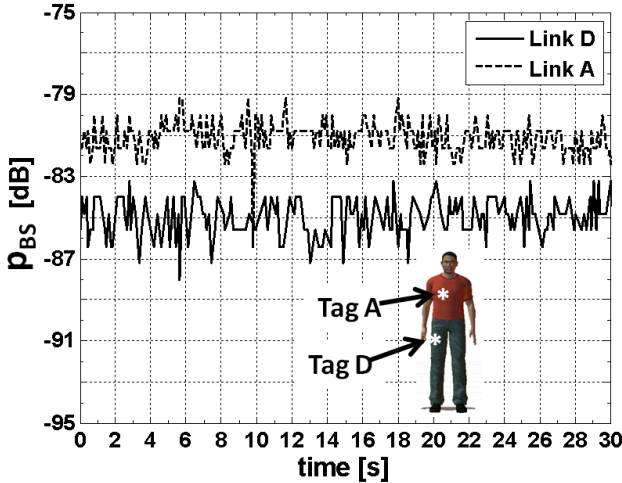


Figure 56: Normalized backscattered power p_{BS} from tags A and D as collected by the on-body PIFA antenna placed as in Fig.46 when the subject is standing motionless.

The measurements in case of walking (Fig.57) show that the motion affects the two links in a different way. While link-A (tag on chest) remains approximately oscillating around the same average value, but with higher fluctuations ($\pm 2\text{dB}$), the backscattered

power for the link-D (tag on the leg) presents a much higher variability due to the time-changing mutual position between the leg and the reader's antenna. In this case the amplitude of fluctuations is $\pm 4\text{dB}$ and they follow the walking rhythm. The period in the first part of the trace is approximately 2 sec, corresponding to a complete movement of the tagged leg at 60cm/s , and then changes to 1 sec in the second trace when the walker's speed doubles.

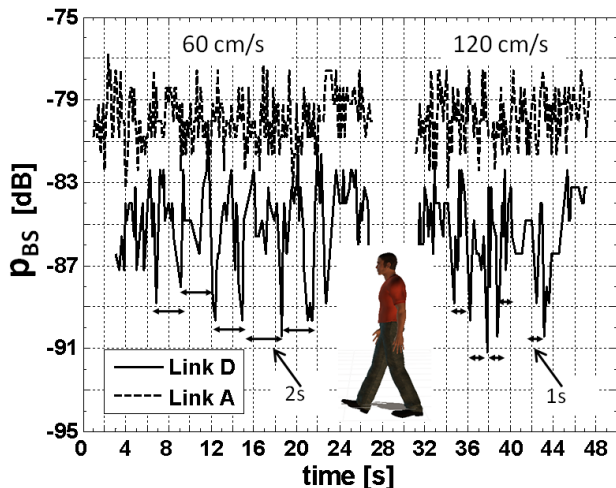


Figure 57: Normalized backscattered p_{BS} from tags A and D when the person walks along a straight line within a corridor with a velocity 60cm/s , initially, and then 120 cm/s . The p_{BS} power looks as able to follow the walking dynamics.

In the same way, link-E was characterized during periodic movements of the arm. Fig.58 shows the fluctuation of the p_{BS} in case of 2s motion periodicity. When the arm is outstretched (parallel to the body), the reader correctly detect the backscattered power while in case the arm is folded (orthogonal to the reader) the microchip does not receive enough power to activate and no signal is detected at the reader side. Hence a cluster-like response is

observed with the clear possibility to recognize the periodicity of the motion.

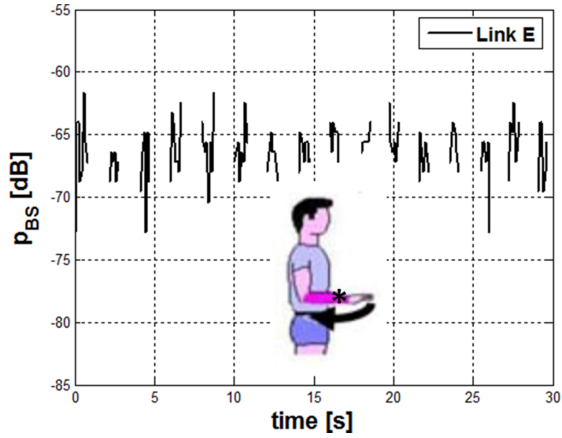


Figure 58: Normalized backscattered power p_{BS} from tag E when the subject's arm is moving up and down with frequency of 0.5Hz.

5.3 MONITORING OF DEFORMATION

The meander-line antenna (MLA) is a commonly used layout to obtain a large variety of RFID tags [61]. An example of symmetric MLA with $2N$ foldings and a tuning T-match section is shown in Fig.59(left). The profile of the wire turns, useful to reduce the antenna size, strongly impacts on the input impedance, since the foldings may be seen as distributed capacitive loads of the structure depending in turn on the mutual distance between facing segments. The antenna gain is instead mainly imposed by the overall length ($h = h_0 + 2 \sum_{n=1}^N h_n$) of the tag.

5.3.1 Mechanical model

If the MLA is subjected to tensile stress through an applied axial force $\pm F_T$, the antenna's shape factor changes (Fig.59(right)) as well. The distributed load, and hence both the input impedance and the antenna gain will be accordingly modified. More precisely, by assuming inextensible wires (rigid structure), the external forces will produce rotation of the folding elements by an angle $\alpha(F_T)$, consequently forcing the horizontal and the vertical translations of the *moving nodes* of the structure [62]. $w(\alpha)$ and $h(\alpha)$ here denote the overall size of the deformed MLA, being $w(0) \equiv w$ and $h(0) \equiv h$ the size of the MLA at rest. By neglecting the wire's radius, each turn of of the MLA under stress produces an elongation equal to $3w(0)\sin\alpha$ and hence the overall size of the MLA is simple expressed in terms of the structures at rest as

$$w(\alpha) = w(0)\cos\alpha \quad (5.4)$$

$$h(\alpha) = h(0) + 6Nw(0)\sin\alpha \quad (5.5)$$

and the *overall elongation* in the strain direction to be correlated with the force is hence $\Delta h = 6Nw(0)\sin\alpha$.

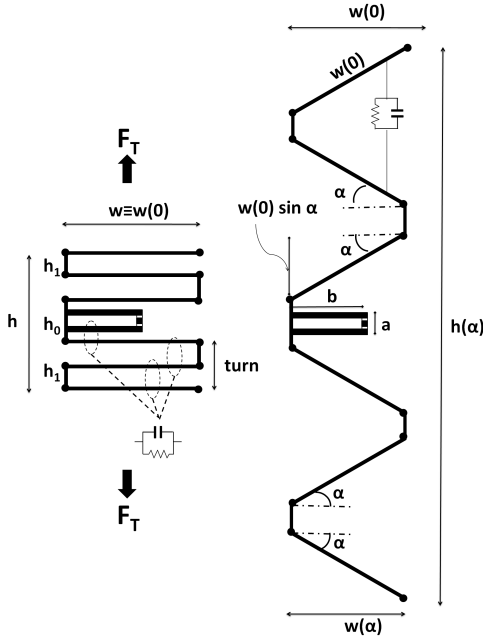


Figure 59: Meander-line tag layout with $2N = 2$ turns Left) quiet state; Right) Stretched state subjected to vertical tractive forces F_T .

5.3.2 Electromagnetic model

During the RFID communication, the passive tag generates a backscattered modulation of the impinging carrier coming from the reader. The power collected by the reader (2.2)

can be expressed by making explicit the dependence on the overall elongation Δh :

$$P_{R \leftarrow T}[\Delta h] = \frac{1}{4\pi} \left(\frac{\lambda_0}{4\pi d^2} \right)^2 P_{in} G_R^2 \eta_p^2 r_{csT}[\Delta h] \quad (5.6)$$

The backscattered power $P_{R \leftarrow T}$ is directly measurable by the reader in terms of the Received Signal Strength Indicator (RSSI), here assumed to correspond [12], [14] to the binary modulating state having $Z_{mod} = Z_{chip}$. $P_{R \leftarrow T}$ carries information about the elongation Δh of the tag thanks to the highlighted dependencies on impedance and gain. To be specific, when the reader-tag mutual position and P_{in} are exactly reproduced in successive interrogations, it is possible to simply derive a *data inversion* (or *calibration*) curve $p_s \leftrightarrow \Delta h$, independently on the reader's gain, by referring the backscattered power to the rest condition ($\Delta h = 0$) of the tag

$$\begin{aligned} p_s[\Delta h] &\equiv \frac{P_{R \leftarrow T}[\Delta h]}{P_{R \leftarrow T}[0]} = \\ &= \left(\frac{G_T[\Delta h]}{G_T[0]} \right)^2 \frac{R_A[\Delta h]}{R_A[0]} \frac{\tau[\Delta h]}{\tau[0]} \end{aligned} \quad (5.7)$$

with $\tau[\Delta h]$ power transmission coefficient of the tag (2.3) The shape of data-inversion curve $p_s[\Delta h]$ is hence a combination of three effects produced by the change of the MLA, e.g. the variation of gain G_T , the variation of the impedance matching (τ) and finally the variation of the real part R_A of the input impedance of the antenna. Other sensing indicators, based on the turn-on power or on the analog identifier, may be derived as described in [22, 15] and straightforwardly extended to the specific sensing problem.

Electromagnetic response to mechanical deformations

An example about possible relationships among the geometric (read mechanical) parameters and the electromagnetic response of the MLA is shown in Fig.2. A $3.6 \text{ cm} \times 3.6 \text{ cm}$, $N = 1$, MLA is designed to have the best conjugate matching, in the rest position ($Z_A[0] = Z_{chip}^*$), to the NXP-G2XM microchip with impedance

$Z_{\text{chip}} = 15 - j135 \Omega$. The antenna responses at 870 MHz (the European RFID frequency) are predicted by a numerical model based on the Finite-Differences Time-Domain method [45].

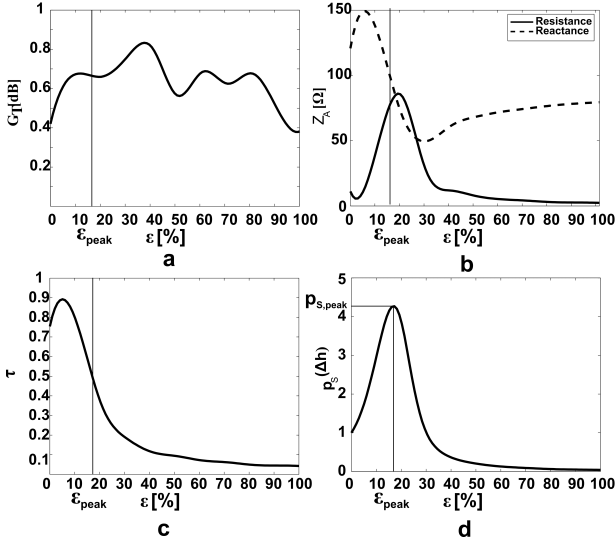


Figure 60: Example of simulated gain (a), input impedance (b), power transmission coefficient (c) and backscattered power (d) of an $N=1$ MLA tag (sizes in [mm]: $h = 36$, $h_0 = 6$, $h_1 = 7$, $w = 36$, $a = 4$, $b = 18$, radius $r_s = 0.5$) with respect to the strain ϵ .

Fig. 60 shows the simulated gain (a) and impedance (b) of the MLA under stress with respect to the *strain* ϵ [62] defined as

$$\epsilon = \frac{\Delta h}{h} \cdot 100\% \quad (5.8)$$

While the gain is only weakly sensitive to the deformation, both real and imaginary part of the tag's input impedance show instead significant variation according to a behavior similar to the

frequency dependence of the input impedance of dipole. By increasing the strain ϵ , the MLA's resistance R_A initially increases as the square [63] of the antenna's overall height $h(\alpha)$ up to reach the anti-resonance condition, afterward giving rise to a non-monotonic profile. The positive offset visible in the reactance is due to the inductive loading effect introduced by the T-match [41]. A similar Gaussian-like behavior can be found in the power transfer coefficient τ (Fig. 60c). Finally, the resulting backscattered power p_S (Fig. 60d) exhibits from (5.7), a sharp and non-monotonic dependence on the applied force with a peak value mainly imposed by the R_A 's one (approximately seven times greater than the initial value). The initial positive slope, with high sensitivity, is then followed by a negative smoother profile, suggesting the possibility of several sensing options. Finally, beyond an $\epsilon=50\%$ strain, the influence of the interactions between facing segments becomes negligible and the antenna performs as a straight dipole without possibility of further wireless sensing.

With the purpose to efficiently master the radio-sensor's response, the profile of the inversion curve is hereafter compressed into just two macroscopic features: the position and amplitude of the peak value, e.g the $(\epsilon_{peak}, p_{s,peak})$ couplet (see Fig.2 d). It is easy to verify that a fully monotonic response with negative slope may be achieved if $\epsilon_{peak} \rightarrow 0$, while a monotonically increasing curve (positive slope) if $\epsilon_{peak} \gg 0$. It is finally expected that the slope of such curves may be shaped by acting on the amplitude $p_{s,peak}$.

5.3.3 Design Methodology

The design of a strain radio-sensor must be strictly connected to the specific application it is going to monitor, and it is here finalized to shape the inversion curve. Some events show very slow and moderate dynamic range, requiring a monitor system able to amplify minimal variations in long timescales. In other cases, especially during extreme events, the processes are characterized by rapid and large structural modifications. It is therefore required that in each specific process, or process' state, the inversion curve

is able to properly follow the expected dynamics of ϵ , being for example single-valued, e.g. monotonic, and steep.

The performances of the MLA-as-a-sensor, e.g. the maximum strain (or dynamic range) and the sensitivity can be derived by the macroscopic features $(\epsilon_{\text{peak}}, p_{s,\text{peak}})$ introduced in the previous Section. The *maximum strain* ϵ_{max} is defined for monotonic sensing curves having positive ($\epsilon_{\text{peak}} > 0$) and negative ($\epsilon_{\text{peak}} = 0$) slopes as

$$\epsilon_{\text{max}} = \begin{cases} \epsilon_{\text{peak}} & \epsilon_{\text{peak}} > 0 \\ \epsilon_{0.1} : p_s(\epsilon_{0.1}) = 0.1 p_s(\epsilon_{0.1}) & \epsilon_{\text{peak}} = 0 \end{cases} \quad (5.9)$$

wherein the 0.1 threshold (10%) over the normalized backscattered power p_s has been arbitrarily chosen in order that p_s may be considered practically insensible to strain $\epsilon > \epsilon_{0.1}$ (see for instance Fig.60 d). The *sensitivity* (2.9) of the sensor is defined as

$$s [\%] = \frac{p_s(\epsilon_{\text{max}}) - 1}{\epsilon_{\text{max}}} \quad (5.10)$$

and gives the percentage variation (increase or decrease) of the collected backscattered power, with respect to the MLA's rest position, corresponding to 1% ($\epsilon_{\text{max}} = 1$) of linear deformations.

The performance of the MLA sensor can be controlled by a proper choice of the geometrical size of the antenna layout. Although in a most general case the whole MLA's shape could be fully engineered to achieve a specific input impedance, as in [18], for the sake of simplicity the foldings are here considered fixed while the control parameters are just the length h_0 of the central segment where the T-match is connected, and the length b of this last one. Fig.61 gives the simulated chart of $(\epsilon_{\text{peak}}, p_{s,\text{peak}})$ vs. the geometrical parameters (h_0, b) and it is useful to design the tag for a required sensitivity and dynamic range. It is worth noticing that the position ϵ_{peak} of the backscattered power's peak (that indirectly imposes the dynamic range of the strain radio-sensor) is

only controlled by the parameter h_0 since the iso-lines for ϵ_{peak} are almost horizontal. The change in h_0 in fact directly affects the electrical length of the MLA and hence the impedance curve $Z_A(\epsilon)$ (see again for instance Fig. 60), will be accordingly shifted like the resonance frequency of a dipole, that moves at lower or higher frequencies by changing the antenna length. In particular, a monotonically dumped response ($\epsilon_{peak} \rightarrow 0$) is achieved by increasing h_0 , e.g. the impedance curve $Z_A(\epsilon)$ is forced to move to the left.

The sensitivity s (e.g. the amplitude of the peak of p_s) which is mainly fixed by the profile of R_A , as stated above, is instead dependent on both (h_0, b) since the values of the resistance R_A originates from the impedance's transformation ratio governed by the T-match [41], and ultimately by the parameter b .

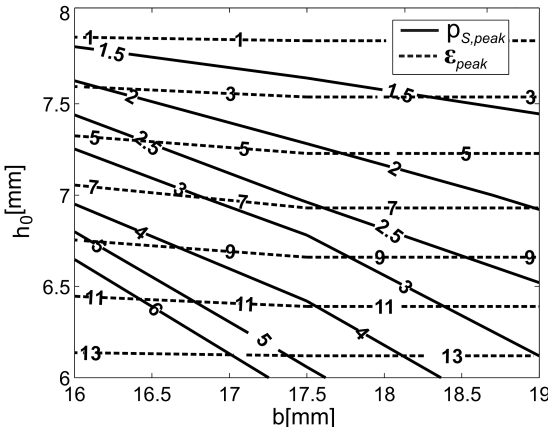


Figure 61: Features of inversion curves (position ϵ_{peak} and peak $p_{S,peak}$) for the meander line tag in Fig.59, with respect to the geometrical parameters (b, h_0) . The other sizes are fixed to the values in Fig.2.

For example, three different kinds of achievable sensing curves are represented in Fig.62 for specific choices of the geometrical MLA parameters. The case A ($h_0 = 8$ mm, $b = 17$ mm) is fully monotonic ($\epsilon_{peak} = 0$) with negative slope (Tab.7) and it

is hence suited to monitor smooth and wide deformations (for examples limb movements during sport or work activity). Case B($h_0 = 6 \text{ mm}$, $b = 18 \text{ mm}$) and case C($h_0 = 7 \text{ mm}$, $b = 16 \text{ mm}$) present instead two upward profiles with smaller ranges but greatly improved sensitivity as required for instance in rehabilitation of injured patients.

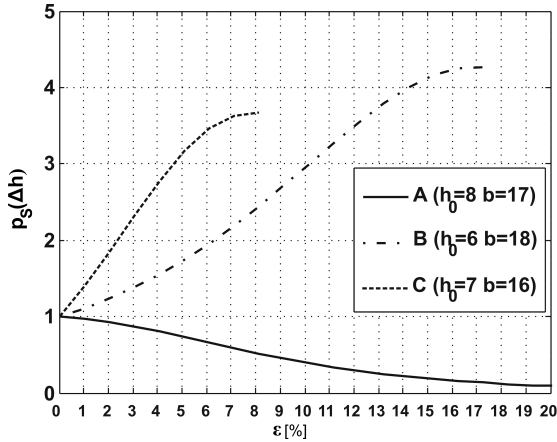


Figure 62: Simulated inversion curves p_s for three different realizations of the MLA radio-sensor, suited to monitor different strain dynamics.

Table 7: Dynamic range and Sensitivity corresponding to MLAs in Fig.62

MLA	ϵ_{max} [%]	$p_s(\epsilon_{max})$	s [%]
A	20	0.1	-4.5
B	17	4.3	19
C	7	3.7	39

In real conditions, the design procedure requires to account for the environment surrounding the tag. The calculation of tag's gain and impedance has to include the presence of all the specific materials and structures wherein the strain sensor will be attached,

e.g. the human tissues, each of them characterized in term of their electromagnetic and mechanical properties. This means that in order to extract absolute measurements about the experienced deformation by means of a specific MLA tag, data calibration should be performed by the help of more accurate measurements as well as by computer simulations on canonical environments.

5.3.4 An Experimental Example

A first $N=1$ turn prototype of the radio strain sensor is fabricated (Fig.63) by means of a folded copper wire ($r_s = 0.5$ mm) while the T-match section has been etched over a $15 \times 25 \times 0.96$ mm FR4 substrate having single-side copper metallization. The copper wires are instead soldered on it.

The geometrical parameters of the prototype are chosen in order to emphasize small deformations (Case B in Fig.62), e.g. by acting on the upward-slope.

The tag is tested by means of a digital-controlled strain gauge (Fig.64) which applies a 0 – 3 Newton axial tractive force to the antenna for a period of 80 s. The MLA is fixed at the terminals of the strain gauge by means of two plastic wires attached to the horizontal outer segments of the antenna by means of loop knots.

During the test, a short range CAEN A528 reader connected to a planar inverted F-antenna (PIFA) with maximum 3.3 dB gain interrogates the tag by means of a fixed input power $P_{in} = 20$ dBm. The distance between reader and tag is chosen to 60 cm and the two antennas are oriented so that the tag is placed exactly in front of the reader's PIFA in polarization matching.

The strain-stress (σ) curve¹ relative to the tag's tractive test is shown in Fig.4. Below the yield point, corresponding to a deformation $\epsilon_e = 6\%$, the tag will deform elastically (the stress is proportional to strain according to Hooke's law) and it will recover its original shape when the applied stress is removed. Once the yield point exceeds ϵ_e , the deformation will become permanent and non-reversible (plastic regime) [62].

¹ The stress σ is defined as the ratio between the applied tractive force and the cross-sectional area of action

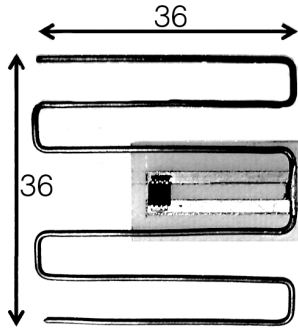


Figure 63: Tag prototype. Size at rest in [mm]: $h_0 = 7$, $h_1 = 7$, $h = 36$, $a = 4$, $b = 19$, $w = 36$, $r_s = 0.5$

The measured backscattered power (according to the conversion formula in 5.2) is visible in Fig.66, superimposed to a low-pass filtering to smooth the typical oscillations of the received RFID signal. It is possible to observe a dynamic range $\epsilon_{\max} \equiv \epsilon_{\text{peak}} = 7\%$, which covers the whole elastic deformation regime ($\epsilon = 6\%$ in Fig.7), and a sensitivity $s = 16\%$. Just to have a numerical feeling, a 10% increase in the backscattered power indicates, from (5.10), an $\epsilon = 0.6\%$ strain of the MLA, corresponding, through (5.8), to an elongation of approximately $\Delta h = 216\mu\text{m}$. It is worth observing that, if a same layout was scaled to the RFID microwave frequency $f=2450$ MHz (MLA sizes roughly reduced to one third), the elongation corresponding to 10% variation of backscattered power should be just $\Delta h = 72\mu\text{m}$.

Finally, although the rough method used to connect the MLA to the tractive machine was rather imperfect, since it does not uniformly distribute the stress over the tag and produces a non exactly symmetric deformation (see the inset of Fig.66), it is apparent that the experimental results are in reasonable agreements with mechanical and electrical simulations corroborating the idea to fully control the whole multi-physics response of the sensor.

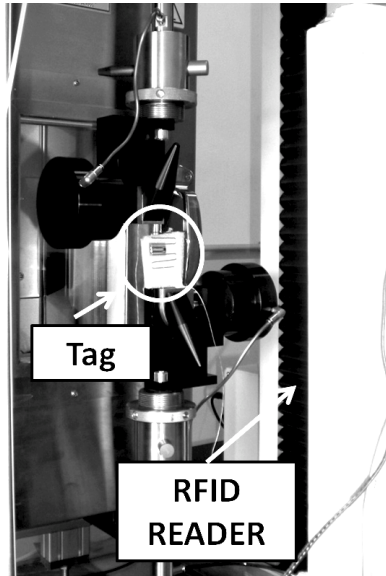


Figure 64: Strain-gauge set-up connected to the MLA prototype by means of two plastic wires attached to the horizontal outer segments of the antenna.

5.4 CONCLUSION

The monitoring of human activity could be considered an achievable target by means of the actual passive RFID technology. According to the particular motion pattern to be monitored it is possible to define different strategies, involving or not passive motion sensors. Both approaches could be used to get information about the subject's state in conventional and unconventional scenarios, every time the possibility to analyze only macroscopic indicators (the transmission or not of an ID code or the fluctuation of the signals) is enough to extract useful medical and behavioral parameters.

The use of passive sensors (digital information) appear more robust compared to the sensor-less strategy (analog information).

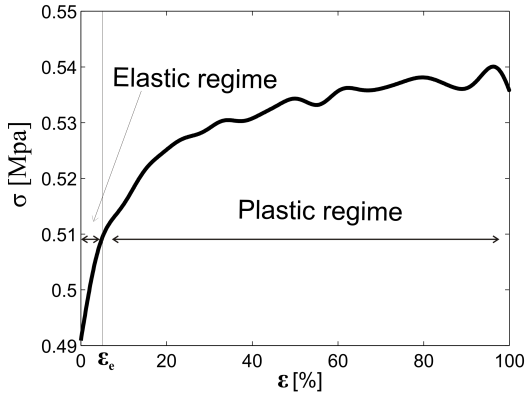


Figure 65: Measured stress-strain curve of the MLA sensor prototype

It can be furthermore enriched by acting on the sensor, e.g on its sensitivity and threshold level. The use of multiple unidirectional inertial switches opportunely placed on the tags, as discussed in Chapter 3, could finally allow the design tridimensional passive motion sensor.

Concerning the sensor-less approach, instead, it is apparent that the use of backscattered power to retrieve the output of a RFID-sensor looks very challenging for links involving moving limbs, since the theoretical dynamic range of the sensing mechanism has to be much larger than 8dB to be recognized by the reader. Nevertheless it is evident that the RSSI may be used as indicator of motion of a specific part of the body and this could be attractive in itself to collect statistics about repeated movements of working people and for remote healthcare of Elders.

Regarding the strain sensor, numerical analysis and early experimentation seem to encourage the use of meander line RFID tag. By acting on just two geometrical parameters of the sole impedance

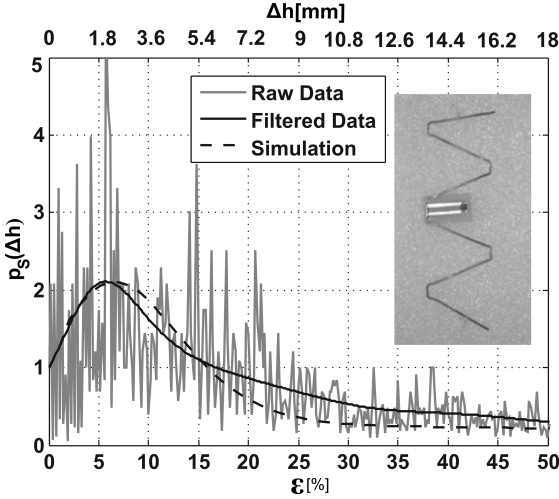


Figure 66: Simulated and measured backscattered power as collected during the strain test. Data referred to the rest condition $\epsilon = 0$ (unstrained tag)

matching section it is possible to design several kinds of sensing responses suitable to large dynamic range of elongations as well as to very small phenomena.

The passive, low-cost (when compared with fully active devices) and pervasive nature of RFID technology can thus offer great advantages when traditional and powered solutions can not be feasible, e.g. when the monitoring period is particularly long or outside from hospital structures.

The shaped conducting wire forming the MLA could be embedded in clothes in places which experience strain (for example elbows, knees, ankles, wrapped around the chest etc.) or it could be used in a separate belt. In exercise or in game applications, the sensor could be integrated into exercise equipment or clothes or it could be used as the game controller as suggested in [64]. Furthermore, in order to avoid the interaction with the human body and make the communication more robust, the same theoretical

and design approaches should be used for antennas layout more suitable for the human body, as the one described in Chapter 4.

The recovery features of the sensor can be sensibly increased by employing super-elastic conductors, e.g. the shape-memory alloys (SMA) [65] already experimented to fabricate RFID tags [66]. Such conducting materials, for instance based on the Nickel-Titanium (Nitinol) alloy, can undergo large deformations at ambient temperature and then instantly revert back to their original shape (impressed during the fabrication process) when the stress is removed. Further investigations are however required to analyze the precision and the reproducibility of the Tag responses during cyclic loads.

Anyway, the bottleneck of this sensing platform is the resolution and stability of the RFID receiver onboard the reader. Actual commercial UHF reader may commonly offer a 0.8 dB resolution (8 bit) which means a 20% minimum appreciable variation in the detected RSSI signal corresponding to a minimum elongation of 0.43 mm in the case of the example prototype. Significantly better performances are hence expected with dedicated readers having a finer resolution in the analog to digital converter.

Finally, this class of sensors may be also used within a grid configuration, as conceived in [15], to achieve a detailed and vectorial monitoring of deformation over large surfaces.

6

MONITORING OF THE ENVIRONMENT: TEMPERATURE THRESHOLD

The Chapter describes how to integrate RFID passive technology and Shape Memory materials to design threshold temperature radio- sensors able to detect, store and transmit data on the thermal history of patients, environments and objects.

In the medical context, the monitoring of the temperature is one of the most important aspects, since it reveals physiological and pathological situations for humans and environments. The clinical meanings of temperature raises and reductions are countless, from the fever due to the seasonal influenza to the hypothermia sometimes experienced by mountaineers. Similar considerations can be expressed for logistics and safety, where for example, high temperature ranges could be extremely dangerous for goods that have to be kept at constant temperature (blood, blood products, medicines and food) and people working in hazardous and extreme situations, like during Firemen's activity. [67], [68].

Nowadays, the most common devices for temperature monitoring are active data loggers [69] (wearable or environmental) which, by means of active sensors and local data storage, are able to store all the time-history of the temperature. The relative high costs and the limited lifetime before recharge make these systems only useful for an environmental-level monitoring, leaving unsolved the problems related to the pervasive personal/item-level control. An alternative and cheaper approach is represented by semi-active RFID temperature tags [70], having a longer lifetime

and able to transmit the instantaneous value of the local temperature following the reader's interrogation. Their main drawback is that the thermal event can be detected only in the presence of a close-distance reader and hence they are not suited to assess the thermal safety in complex scenarios, e.g. all along the medicine supply chain.

A possibility to reduce cost, size and maintenance of RFID sensor systems is to focus the attention to a completely passive technology where the challenge is to design a proper passive sensor component able to perform the sensing activity without batteries and to store the occurrence of the temperature hot spot independently on the reader interrogation. Very often, in fact, it is required to monitor only quick and unexpected temperature rushes over a threshold value, symptomatic of dangerous environmental conditions or severe health worsening. One-shot sensors could be at this purpose suitable and particularly useful when there is the need to rapidly screen a large number of people or items.

Following this idea, a UHF passive sensing tag which integrates a temperature printed nano sensor has been recently proposed in [71]. The sensor works as a chemical thermal fuse able to record the thermal event by irreversibly changing its resistivity through the melting of the polymeric part of the conducting ink. However, it currently looks suitable only for high temperature applications, approximately over 60°C, and not for typical cold supply chain conditions.

In [72] a similar idea was instead applied to low temperature, wherein the switch effect was obtained by the melting of an iced region placed in the close proximity of the antenna and hence the device is restricted to applications around 0°C without many tuning possibility.

This Thesis proposes a completely different mechanism to achieve one-shot RFID thermal seals, fully suitable to high and low temperatures, in a range approximately between -30°C and 100°C . A *shape-memory-alloy* (SMA) compound, introduced into an RFID tag as sensitive material, modifies its geometry depending on the local thermal boundary conditions and consequently it is able to modulate the RFID communication.

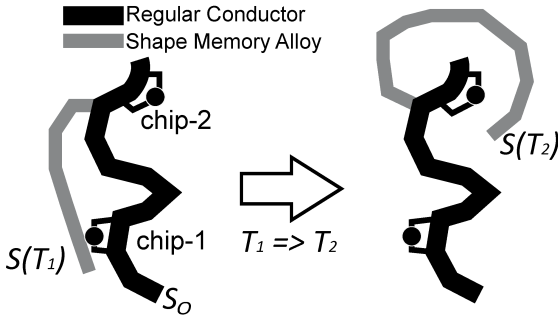


Figure 67: Functional scheme of a two-chip temperature sensing tag embedding regular conductors of shape S_0 and Shape Memory compounds whose shape S is strongly affected by the local temperature.

The sensing tag is here conceived as an antenna provided with two RFID microchips so that the first one (chip-1) is able to transmit its digital identifier (ID_1) regardless the temperature status, while the second chip (chip-2) transmits or not its code (ID_2) depending on the local temperature. Hence ID_1 has the meaning of item's identifier while ID_2 gives its status information, e.g. a thermal alarm (above or below a threshold temperature), according to the ID-modulation paradigm [26]. For this purpose, a portion of the antenna (Fig.67) is fabricated in SMA whose shape variation with respect to the temperature will be such to match or mismatch the chip-2, leaving mostly unmodified the impedance condition seen by chip-1. The occurrence of a hot spot is hence registered into the device by a shape change, independently on the presence of the reader.

The design of such a new family of devices deserves some care for what concerns the management of multi-chip RFID tags, and a proper methodology is here proposed able to take into account the two-state response of the tag.

6.1 THE NITINOL THERMAL SWITCH

Shape memory alloys [65] are characterized by two crystallographic phases, a *martensitic* one and an *austenitic* one, in which the structural and mechanical properties of the alloy greatly change. By heating, martensite transforms into austenite, the only stable phase at high temperature. SMAs are easily deformable in the martensitic phase; however they recover the prefixed austenitic shape every time they are heated above the transition A_S temperature (*Austenite Start*), with an increasing recovery as the temperature rises up to A_F (*Austenite Finish*). According to their property to recover the “memorized” shape, the SMAs can be employed both as sensors and/or as actuators.

The shape-memory effect has been found in many alloys such as CuAlNi, CuZnAl, AuCd, but NiTi, also known as Nitinol [73], is the most commonly used thanks to its good characteristics of corrosion resistance, ductility, high recoverable deformation, relatively high electrical conductivity ($\sigma_{\text{NiTi}} = 1.2 \cdot 10^7 \text{S/m}$, [74]) and biocompatibility. Nitinol is nowadays widely used in medicine and robotics mainly to build actuators. In the Electromagnetic context Nitinol wires are instead used to fabricate flexible whip antennas for mobile terminals.

It is worth mentioning that the transition temperature A_S is tunable by changing the alloy percentage composition: therefore transitions can be obtained in a very wide range of temperatures, i.e. between -30°C and more than 100°C . This unique feature makes the Nitinol an enabling compound to assess the integrity of pharma, blood sacs, frozen foods and to monitor fever rush or industrial processes in general.

6.1.1 Switch geometry

There are several options to achieve a temperature-sensitive tag taking advantage of the shape recovering feature of the Nitinol, but one of the easiest is to conceive a thermal switch which is normally closed when the temperature $T < A_S$ and open for $T > A_S$. The switch can be placed in series or in parallel to the chip-2 (see again Fig.67) to strongly affect its activity. According to the

last case, the tag' states will be: ID₁ under thermal threshold, and ID₁+ID₂ over the thermal threshold. A possible implementation of a thermal SMA-based switch, suitable to RFID antenna integration, includes a Nitinol wire segment processed to have straight shape in the austenitic (stable) phase. The wire is bent (Fig.68) in the martensitic phase, e.g. for $T < A_S$, and fixed across the gap of a copper trace (wherein the RFID microchip will be placed) by a crimped connector¹ soldered at one of the gap's sides, and more softly, by a silver glue, at the other side. When the temperature exceeds the threshold ($T > A_S$), the wire begins to recover its original straight shape, breaking the conducting glue and hence opening the switch.

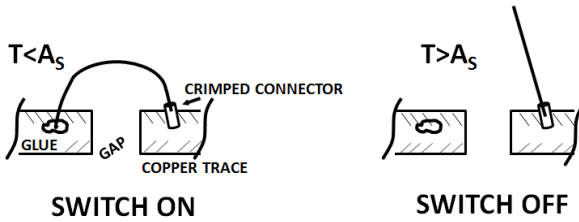


Figure 68: Geometry of the Nitinol temperature switch in the martensite and austenite states.

Since the austenitic shape is stable, a successive fall of the temperature below the threshold will not modify the wire's shape anymore. The Nitinol switch hence acts as a one-way element, configuring itself as an unidirectional thermal fuse.

6.1.2 Prototype and characterization

Fig.69 shows a fabricated example of a Nitinol switch over a FR4 substrate (thickness 1.58mm). Two Nitinol wires having a nominal transition temperature $A_S = 80^\circ\text{C}$ and different diameters (0.3mm, 0.5mm), respectively, have been considered in separate devices.

¹ The Nitinol can not be easily soldered and hence a possible fixing is achieved by crimping the Nitinol wire within a conducting small cylinder and soldering this one on the antenna trace.

The same figure gives a graphical rendering of the switch-off capability of the device, when the temperature is linearly raised from 60°C to 85°C in a thermostatic chamber. The switch-off event has been collected by monitoring the DC resistance at the switch's terminals. A sharp variation of input DC resistance from low (switch on) to an extremely high value (switch off) indicates the transition from martensite to austenite, and hence the required open circuit. The experiments have been repeated five times for each kind of switch and the detected transition temperatures in Table 8 demonstrate that the device mechanism has good repeatability, with a temperature uncertainty of 1-2 °C. The switch-off (T_{SW}) temperature is dependent on the diameter of the wire so that a thicker Nitinol will recover the stable state at a lower temperature in comparison with a thinner wire and hence this one is more sensible.

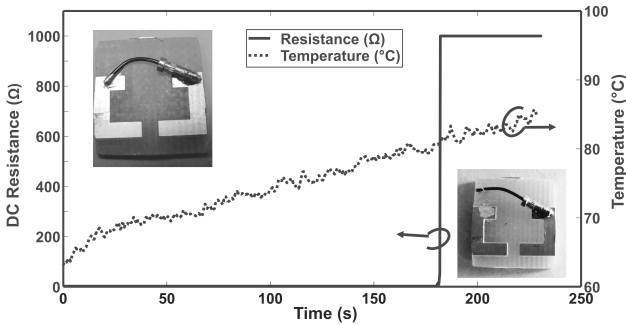


Figure 69: Example of fabricated Nitinol switch and graphical representation of the switch-off with respect to the temperature rising.

Table 8: Switch-off temperature detected by the considered Nitinol switches

Wire diameter (mm)	T_{SW} (°C)	σ_T (%)
0.3	81.7	1.44 (1.7%)
0.5	75.3	2.7 (3.1%)

From an electrical point of view, the Nitinol wire can be simply modeled by a lumped impedance $Z_{\text{NiTi}}^{\text{ON/OFF}}$, and in particular as an ideal open circuit when in the austenite phase ($Z_{\text{NiTi}}^{\text{OFF}} = \infty$), and as a real inductor ($Z_{\text{NiTi}}^{\text{ON}} = R_{\text{NiTi}} + j\omega L_{\text{NiTi}}$) with parameters

$$R_{\text{NiTi}} = \rho \frac{l}{A} \quad (6.1)$$

$$L_{\text{NiTi}} = 2l \left[\ln \left(\frac{2l}{r_0} \right) - 1 \right] \quad (6.2)$$

in the martensite phase, where l and r_0 are the length and the radius of the Nitinol wire segment, respectively [75].

6.2 TWO-CHIP TAG ANTENNA DESIGN

The passive RFID communication between reader and tags requires the input impedance of the antenna to be matched to the conjugate of microchip impedance for maximum power transfer (and hence for maximum reading range) [76]. Since the two RFID microchips are connected over a same radiating structure, the electromagnetic coupling can not be neglected and hence the input impedances to be controlled are the *active impedances* of the system [17]. The design problem can be conveniently formulated in terms of a two-port antenna system in receiving mode. The corresponding network model is given in Fig.70: $Z_{L1} = Z_{\text{chip}}$ is the load impedance at port-1, wherein the chip-1 is connected, while $Z_{L2} = Z_{\text{chip}} \parallel Z_{\text{NiTi}}$ is the terminating impedance of port-2, which depends on the ON/OFF status of the Nitinol switch, and hence on the sensed temperature. $V_{1,2}^{\text{OC}}$ are the open circuit voltages collected at the ports and produced by the interrogating field emitted by the remote reader. Z is the impedance matrix of the unloaded two-port antenna.

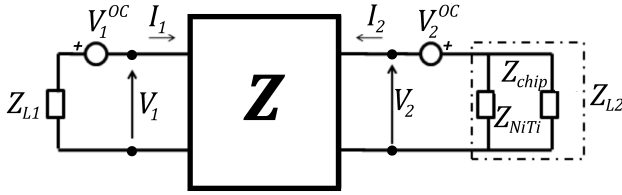


Figure 70: Two-port model of the two-chip RFID tag in receiving mode.

The network equations [77] are

$$\begin{aligned} Z_{11}I_1 + Z_{12}I_2 &= V_1 = -V_1^{OC} - Z_{L1}I_1 \\ Z_{21}I_1 + Z_{22}I_2 &= V_2 = -V_2^{OC} - Z_{L2}I_2 \end{aligned} \quad (6.3)$$

The open circuit voltages depend on the geometry of the tag but also on the mutual orientation between reader and tag. Therefore, as in the case of a regular array, the active impedances of the tag are strongly affected by the interrogation modality. The general formulation of this kind of multi-chips device, also denoted as "RFID grids", can be found in [15]. Under broadside incidence condition (e.g. the plane of the tag is perpendicular to the reader's antenna beam), it is possible to assume $V_1^{OC} = V_2^{OC}$ and the above system equation gives:

$$\frac{I_2}{I_1} = \frac{Z_{11} - Z_{21} + Z_{L1}}{Z_{22} - Z_{12} + Z_{L2}} \quad (6.4)$$

Accordingly, the active impedances for broadside interrogation are:

$$Z_{in,1} = Z_{11} + \alpha Z_{12} \quad (6.5)$$

$$Z_{in,2} = Z_{22} + \frac{Z_{12}}{\alpha} \quad (6.6)$$

where $\alpha = (Z_{11} - Z_{21} + Z_{L1}) / (Z_{22} - Z_{12} + Z_{L2})$. The maximum power transfer from the antenna to the microchip loads imposes [78] the following conjugate matching conditions at the ports:

$$Z_{in,1} = Z_{chip}^* \quad (6.7)$$

$$Z_{in,2} \parallel Z_{NiTi} = Z_{chip}^* \quad (6.8)$$

By recalling the ID-modulation [26] scheme to be implemented in the sensing RFID tag, e.g. that only the chip-1 is matched in the ON state ($T < A_S$), while both the microchips are active in the OFF state ($T > A_S$), the matching conditions to enforce on the two-ports tag are

$$\text{switch ON : } \begin{cases} |Z_{in,1} - Z_{chip}^*| \rightarrow 0 \\ |Z_{in,2} \parallel Z_{NiTi}^{ON} - Z_{chip}^*|^{-1} \rightarrow 0 \end{cases} \quad (6.9)$$

$$\text{switch OFF : } \begin{cases} |Z_{in,1} - Z_{chip}^*| \rightarrow 0 \\ |Z_{in,2} \parallel Z_{NiTi}^{OFF} - Z_{chip}^*| \rightarrow 0 \end{cases} \quad (6.10)$$

The geometrical parameters of the two port antenna have to be therefore designed such to achieve the best trade-off among the above conditions. The following fitness function

$$F = w_{11}|Z_{in,1} - Z_{chip}^*| + w_{12}|Z_{in,2} \parallel Z_{NiTi}^{ON} - Z_{chip}^*|^{-1} + w_{22}|Z_{in,2} - Z_{chip}^*| \quad (6.11)$$

has thus to be minimized by means of a conventional optimization tool (w_{mn} are constant weights), having assumed $Z_{NiTi}^{OFF} = \infty$ as discussed in the previous Section.

6.3 PROTOTYPE

A first prototype of the UHF RFID thermal seal consists of a layout as in Fig.71 originated from the single-port design in [79] where a planar dipole has been partly folded to reduce the overall area to a typical credit card size. The port impedances are controlled by the aspect ratio of two symmetric T-match circuits. The Nitinol switch has been fabricated as previously described by using a Nitinol wire of radius $r_0 = 0.5\text{mm}$ and length $l = 1\text{cm}$. Accordingly, the closed-state impedance from (6.1) and (6.2) is $Z_{\text{NiTi}}^{\text{ON}} = 0.1 + j37\Omega$. The RFID microchips are NXP TSS OP8 with nominal input impedance at 869MHz $Z_{\text{chip}} = 15 - j135\Omega$ and power sensitivity $P_{\text{chip}} = -15\text{ dBm}$.

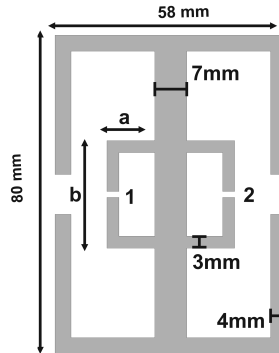


Figure 71: Layout of the two-chip tag whose double T-match aspect ratio (a, b) has to be optimized to achieve the required ID modulation.

For the sake of simplicity, the T-match circuits are assumed to be of equal sizes $\{a, b\}$ whose values are selected by minimization of the fitness function $F(a, b)$ in (6.11) with respect to weights $w_{11} = 0.85$, $w_{12} = 0.05$, $w_{22} = 0.1$. The antenna's Z matrix, for each shape of the T-match, is evaluated by an FDTD model [45] of the tag layout. Fig.72 shows the map of $F(a, b)$: a solution suited to fabrication is $a = 12\text{mm}$ and $b = 25\text{mm}$. The prototype has

been cut on adhesive copper sheet as shown in Fig.73 with a detail of the Nitinol wire insertion.

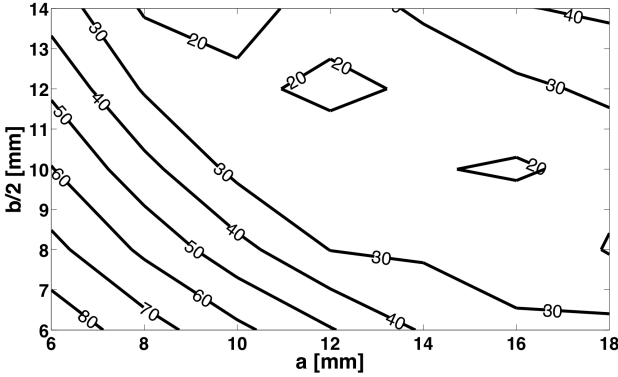


Figure 72: Map of the fitness function $F(a, b)$ in equation (6.11) calculated by FDTD simulations.

The electromagnetic tag performances in ON and OFF states have been experimentally characterized with respect to the realized gain in (2.6) which directly imposes the tag's read distance. For this purpose a customized UHF long-range reader based on the ThingMagic M5-e ASIC has been used. The sensing tag is interrogated by means of a 6dBi circular polarized patch antenna, connected to the reader. The tag is placed in front of the reader's antenna, at 1.5 m from ground and the floor reflections are minimized by using absorbing panels. The realized gain is measured by means of the turn-on power method [22].

Fig.74 and 75 give the measured $G_{\tau,n}(\theta = \pi/2, \phi)$, at 870MHz, over the horizontal plane in both the Nitinol states. When the switch is closed and hence only the chip-1 is active, the realized gain over the H-plane is rather omnidirectional, with average value close to -1dB. When the switch is open both the microchips are responding and the active radiation diagrams become less omnidirectional with specular gains of the two chips with respect to $\phi=180^\circ$. About 3dB ripple and lower values are evident with respect to the single port case due to the presence of the inter-

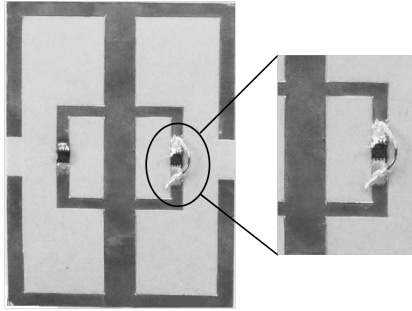


Figure 73: Adhesive copper-sheet prototype of the tag embedding two microchips and the Nitinol switch, deduced from Fig.71 with $a = 12\text{mm}$ and $b = 25\text{mm}$. The Nitinol wire length and diameter are $l = 1\text{cm}$ and $r_0 = 0.5\text{mm}$, respectively.

port coupling. Under the assumption of free space conditions and interrogation power 3.2W EIRP, the measured realized gain achieves a maximum read distance (by inverting equation (2.6)) given by $d_{\text{max}}(T < A_S) = 8\text{m}$ and $d_{\text{max}}(T > A_S) = 6\text{m}$, below and above the threshold temperature, respectively.

6.4 THERMAL CHARACTERIZATION OF THE TAG

The proposed RFID sensor has been tested in real conditions in order to verify the effective communication and sensing performances. Two different scenarios have been reproduced: a first one characterized by a high-temperature environment and a second one with a very low-temperature condition as for the logistics of frozen items. The Nitinol switch has been accordingly fabricated with wires of nominal transition temperature $A_S \simeq 80^\circ\text{C}$ and $A_S \simeq -0^\circ\text{C}$, respectively. The same antenna layout, shown in Fig.73 has been used for both the experiments.

The tag has been attached on a cardboard box and heated inside a temperature controlled chamber, while being monitored by a thermal probe and continuously interrogated by the reader antennas also placed inside the chamber itself (Fig.76). The tag's digital responses have been registered while the local temperature was

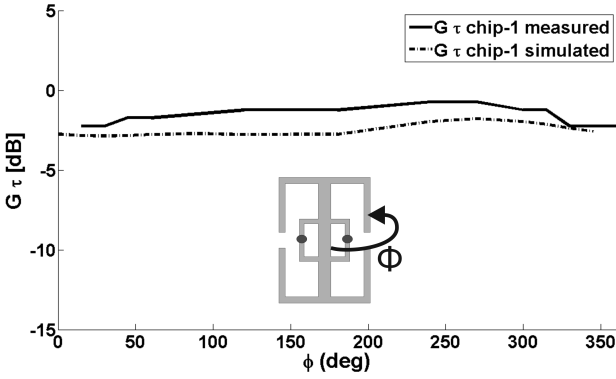


Figure 74: Measured and simulated realized gain for the sensor-tag when the temperature is under the threshold ($T < A_S$) and only chip-1 is responding.

progressively raised from a $T_{init} < A_S$ up to observe the martensite to austenite transition. The temperature was recorded through a thermocouple connected to a multimeter and correlated to the digital responses of the tag. The reader collects only the ID₁ below the A_S temperature. When both ID₁ and ID₂ are received for the first time it means that the Nitinol switch has broken the glue and the switch-off temperature T_{SW} can be accordingly detected through the thermocouple reading.

In case of the low-temperature Nitinol, particular care was devoted to the integration of the Nitinol wire into the tag and to have the conducting glue getting solid. The fabrication of the switch was hence performed inside the thermostatic chamber itself.

In both cases the measurements have been repeated five times to perform averaging. Examples of collected data in both the experiments are shown in Fig.77 and Fig.78 and the estimated switch-off temperatures can be found in Table 9.

The standard deviation is the same (3°C) in both the configurations even if it is percentually more significant in the low-temperature case. This is probably due to the more difficult integration of the nitinol wire at temperature below zero degrees. The

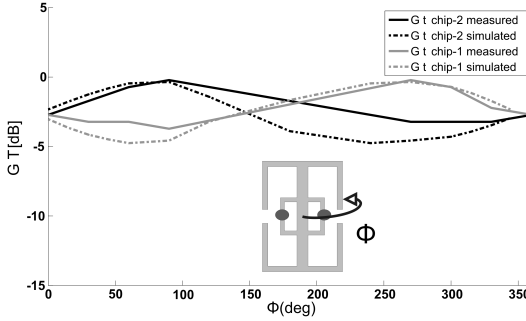


Figure 75: Measured and simulated realized gain for the sensor-tag when the temperature is over the threshold ($T > A_S$) and both chips are responding.

Table 9: Switch-off temperatures of the sensing tags

nominal A_S (°C)	T_{SW} (°C)	σ_T (°C)
80	84.7	3.1
0.0	-4.1	3.0

conducting glue adhesion reliability proved to be poor due to the presence of water/ice condensation between the nitinol and copper trace which makes it difficult to replicate the same device conditions in successive tests.

6.5 CONCLUSIONS

The Nitinol compound demonstrates to be suitable for integration into UHF tags for the control of both cold and hot goods and its response to temperature variation seems to be stable and repeatable, especially at high temperatures. The proposed layout could respond to typical requirements of *peel & stick* sensor devices, easily fixable over objects and workers' garments. As demonstrated in [80], if properly spaced from the body, also dipole-like tags can be used for wearable applications with appreciable performances. In

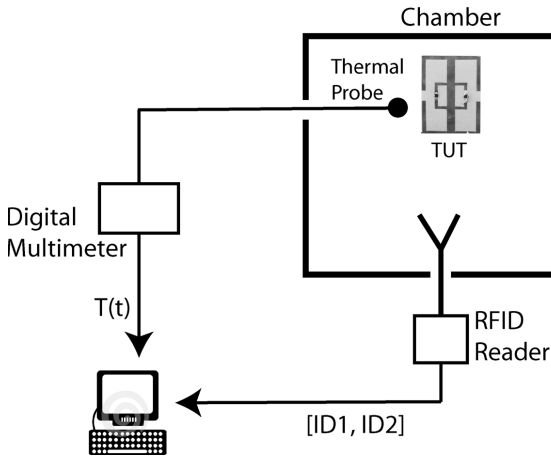


Figure 76: Measurement setup comprising the remotely controlled reader, the multimeter connected to the thermocouple and the RFID tag under test (TUT), placed into the thermostatic chamber.

order to have more suitable body-worn device, the same sensing approach can be instead integrated in patch-like antennas like the one in Chapter 4

The experiments however highlight the importance of having a stable fastening method for the Nitinol wire to the antenna and further research is required to improve the stability of the device, particularly below 0°C . Moreover the self-sensing tag should be provided with a lock mechanism to keep the Nitinol wire in the curved shape before use even at temperatures exceeding the austenite transition. This is also important in case the tags are placed over the items before they freeze.

Finally, the described design methodology for two-chip tags is more general than the considered temperature application, and it may be extended to the integration of other families of passive sensors, provided that their impedance model is known and that the fitness function is properly defined according to the required data encoding.

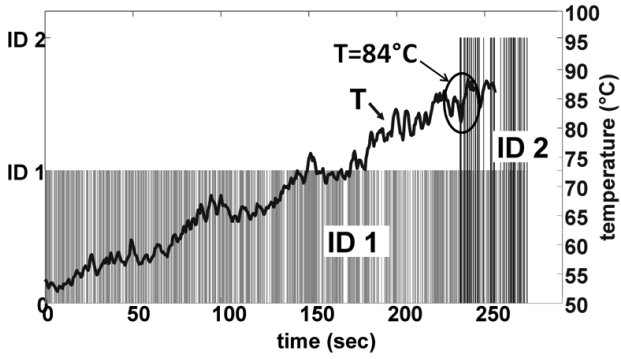


Figure 77: Digital response from sensing tag with $A_S \approx 80^\circ\text{C}$ versus temperature raise and time.

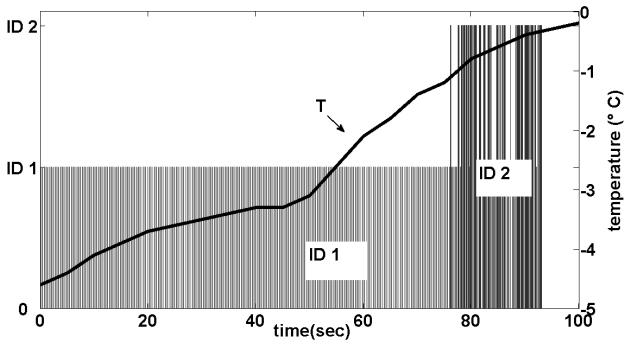


Figure 78: Digital response from sensing tag with $A_S \approx 0^\circ\text{C}$ versus temperature increase and time.

7

MONITORING OF THE ENVIRONMENT: QUALITY OF THE AIR

The Chapter proposes two RFID gas sensors for the monitoring of the quality of the air, a humidity sensor and an ammonia gas sensor. The general considerations, resulting from the theoretical and experimental analysis of the proposed devices, could open the way to more complex radio sensors, a kind of passive *lab-on-tag*, pervasively distributed on and around the human body

The monitoring of the quality of the air surrounding people indoor and outdoor is extremely important in pervasive healthcare systems to assist the analysis of personal situations and detect possible dangerous events in working and domestic scenarios. Accidental exposure to gases or toxic agents poses, for example, many challenges to the health and rescue professionals, e.g. Anesthetists and Firemen. Similarly, the safety of elderly and children could be sensibly improved by means of devices able to sense the quality and the nature of food and beverages from the gases emanated during their deterioration, such to avoid inadvertent consumptions.

The possibility to use passive RFID tags as sensors has been investigated in the previous Chapters for the wireless observation of several process in evolutions. In particular, sensitive materials may be integrated together with the tag's antenna at the purpose to transduce chemical/physical variation into changes of the tags' radiation performances, as preliminary demonstrated regarding the use of shape memory alloys to detect the threshold

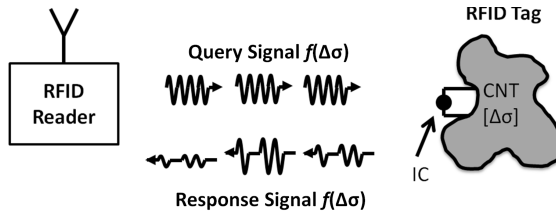


Figure 79: The change of the electromagnetic response of doped RFID tag can be related to a variation of the environment surrounding it.

rise of environmental temperature. It is hence feasible to imagine many applications to the monitoring of the environmental conditions by pervasively distributed low-cost sensors within houses, warehouses and workplaces in general.

Among the different environmental parameters characterizing the quality of the air, humidity and toxic gases are surely of prime importance.

The physical rationale of the proposed sensors lies in the clear dependence of the tag's radiation performances on the physical and chemical features of the integrated sensitive materials, strongly affected by the close surrounding environment (Fig.79). When the environment where the tag is placed undergoes changes in time, due to the presence of humidity, ammonia or other gases, the sensitive material's electrical features (permittivity ϵ and conductivity σ) accordingly change, so affecting the tag's performance, and these variations can be remotely detected by the reader [17].

In the past thirty years, many humidity sensors have been proposed based on various materials for both relative and absolute measurements, including ceramic, semiconducting, and polymers. The latter received particular attention thanks to their attractive features, such as high sensitivity, fast response, robustness at room temperature, low-cost, low toxicity and flexibility [81]. According to the sensing mechanisms, polymeric humidity sensors are divided into two fundamental categories: resistive-type and capacitive-type. The former responds to moisture variation by

changing its conductivity while the latter reacts to water vapor by varying its dielectric constant [82]. Among the different polymers showing sensitivity to humidity, one of the most exploited is *poly(3,4-ethylenedioxythiophene) : poly(styrenesulfonic acid)* PEDOT:PSS [83]. Such a conducting polymer shows significant and reversible modification in its electrical properties when exposed to changing humidity. It can be easily manufactured on an industrial scale and can be used in many deposition techniques [84]. For sensing purposes, it is very often deposited on interdigital capacitors and characterized in DC, showing monotonic exponential variation of resistance when exposed to humidity [85].

From the RFID perspective, early prototypes involving sensitive coating or substrates have been recently proposed as passive humidity sensors. In [86] the use of hydrophilic polymers and interdigital capacitors has been investigated for integration on flexible RFID tags. However, no attempts has been done to effectively integrate the device in the antenna, such to have a fully working radio-sensor. Similarly, a fully working antenna integrating polyimide films has been described in [87]. The complete RFID radio-link and first experimental characterization can be found in [88]. In this case the sensitive material is simply a blotting paper, eventually doped with NaCl (salt), covering an RFID patch-like tag: since the paper absorbs water the radiation performances of the tag sensibly degrade, thus producing appreciable variations of the tag's response link. However, the true stability of the sensor in cyclic exposures, the recovery features and the relative hysteresis have not been addressed. Very recently, the effects of water absorption of dielectric substrates has been finally evaluated and exploited in [89] for the design of a printed RFID dipole-like sensor tag. The sensitivity and the communication performances have been evaluated in term of turn-on power and frequency shift, however no attempt was done to master the achievable sensitivity and to characterize the dynamic response of such class of devices to cyclic exposures.

Traditional gas-sensing mechanisms exploit instead vapor-sensitive polymers, semiconductor metal oxides or porous structures, which require micro-fabrication techniques, power supply and data processing electronics that may preclude many low-cost mon-

itoring applications [90]. Carbon Nanotubes (CNT) composites [91] have been recently found to perform as a gas sensor due to their high surface-to-volume ratio and hollow structure that are well suited for gas molecules absorption and storage. Upon exposure to small quantities of certain gases, CNTs change their physical properties, such as their electrical conductance (molecules act as electron donors or acceptors), and this variation can be easily detected by various methods [92]. Concerning wireless systems, for example, a CNT-based inductor-capacitor resonant circuit (LC) with multi wall CNT-SiO₂ composite as sensing layer has been proposed in [93] as passive wireless gas sensor. The presence of gas in the air produces a change of the dielectric properties of the CNT coating and hence of the resonant frequency of the system, detectable by a loop antenna located approximately 15cm from the sensor. However, the extremely low frequency (~ 10 MHz) and the magnetic coupling between the radiating structures make the proposed platform not suitable to medium/long-range applications. The same sensing approach has been evaluated also in [94] for a wired configuration.

From a different side, several CNT-based antennas have also been developed for their attractive characteristics. Due to the very high inductance per unit length [95], it is possible to fabricate CNT nanoantennas, while their relatively low cost, wide bandwidth and simplicity of fabrication can indeed offer great advantages in RFID applications [96]. Finally, the good mechanical properties of this kind of materials, such as flexibility, strength and low weight, suggests interesting opportunities in wearable electronics and antennas [97].

While the idea to integrate sensing carbon nanostructures into a passive RFID tag was first introduced in [21], no attempt has been done up to date to design, fabricate and test a complete CNT-tag working as a medium-range passive radio sensor.

In this view, this Thesis explores the integration of *ad-hoc* designed UHF (870MHz) RFID tags together with sensitive polymers (PEDOT:PSS) and single wall carbon nanotubes (SWCNT) to achieve fully controllable humidity and ammonia sensors. Theoretical and experimental analysis are presented, with the aim of optimizing the amount of chemical matter and its position to

enhance the communication and sensing features. The effective sensing performances are experimented in real scenarios, which permit to evaluate the phenomena of recovery and hysteresis.

7.1 HUMIDITY SENSOR

The proposed device is a modified version of the wearable antenna presented in the previous Chapter 4: a folded planar structure over a teflon substrate 4mm thick, provided with a radiating edge and a sensing H-shaped slot wherein gas-sensitive polymers can be spread (Fig. 80). The H-slot acts as an impedance transformer and hosts high value of electric field, for this reason the sensitive polymers are thus placed just within it [60]. In order to reduce the area of chemical deposition and increase the sensitivity of the device, two rectangular conductive patches have been placed inside the H-slot. In this way, the current is forced to flow with opposite phases along the outer and inner perimeters of the slot and hence each half glasses-like profile may be considered as a combination of six slotlines whose characteristic impedances are affected by the dielectric properties of the polymer spread on top (Fig.81). The tag can be described by means of the same equivalent circuit proposed in Chapter 4 by simply modifying only the portion relative to the coupled slot.

The field distribution is not uniform inside the H-slot. The most sensitive area, i.e the portions where the field is maximum, is the central gap (hosting the RFID IC) and the upper inner vertical segments.

Since the water absorption produces a change of the polymer's dielectric properties, a variation of both input impedance and losses of the antenna is in turn expected and may be remotely detected by the reader as a modification of the tag's activation and backscattered power.

It is worth noticing that only one of the radiating elements of the antenna is affected by the sensing activity, since the fringe slot (indicated as "radiating edge" in Fig. 80) remains unmodified and thus assures the robustness of the communication link regardless the sensing process.

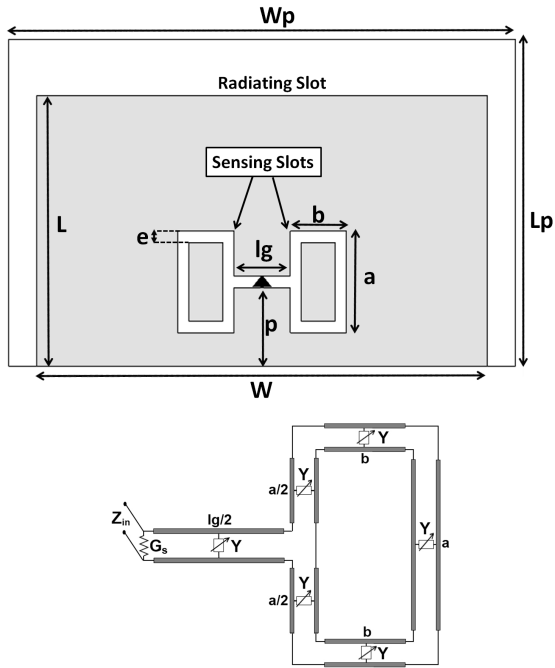


Figure 80: RFID humidity sensor and equivalent slot-line circuit of the H-slot.

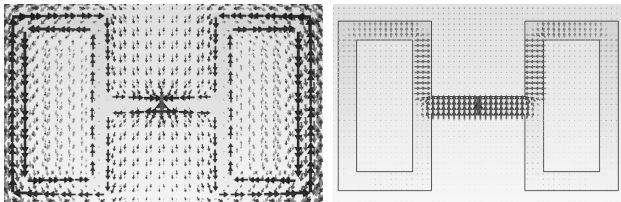


Figure 81: Current (left) and aperture field (right) distribution on the sensitive H-slot

Sensitive material

The material used in this work is the commercial species Clevios PH 500, a dispersion for conductive coatings with PEDOT to PSS ratio of 1:2.5 (Fig.82). Like other polymers containing sulfonic acid groups, PEDOT:PSS is strongly hygroscopic and takes up moisture when handled under ambient conditions. Thin layers of PEDOT:PSS films up to a thickness of about 100 nm are almost able to instantaneously absorb water from the environment: the absorbed water is incorporated into the films and consequently produces an increase of the layer thickness, especially pronounced for films with a high PSS content (as in the considered case) and can reach up to 30%.

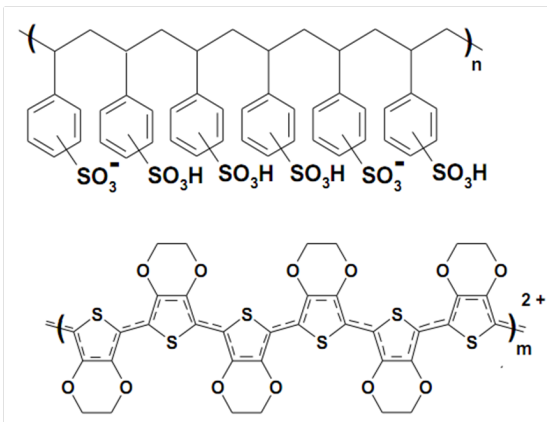


Figure 82: Poly(3,4-ethylenedioxythiophene) : poly(styrenesulfonic acid) PEDOT:PSS chemical formula.

PEDOT:PSS is well known within the antenna and RF community. Thanks to its characteristics, it has been recently used as conductive material for printed antennas applications [98]. Optical translucency of PEDOT:PSS allows to hide an antenna or make the antenna virtually invisible [99, 100] when mounted on a transparent substrate, such as the screen of a laptop or PDA, while the ductility allows to attach the polymer on flexible fabrics and plastic substrates.

7.1.1 Prototype and Characterization

A first prototype (Fig. 83) of the proposed tag has been designed and fabricated according to the guidelines described in Chapter 4 (size listed in Table 10). The tag is matched to the G2iL NXP IC with $Z_{\text{chip}} = 26 - j227\Omega$ and power sensitivity $P_{\text{chip}} = -18\text{dBm}$. The design procedure has been optimized for the unloaded tag, i.e. without polymer spread on the H-slot.

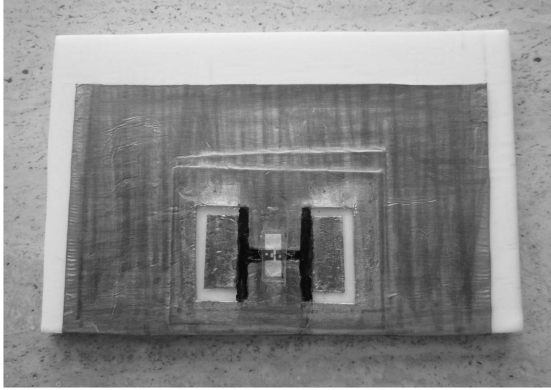


Figure 83: RFID sensor prototype over a Teflon substrate 4mm thick with a partial polymer filling on the sensing glasses-like slots.

The communication features of the unloaded tag have been characterized by considering the realized gain G_{τ} (2.6). The measured and simulated profiles are shown in Fig. 84. Simulations are performed by a Finite-Difference Time-Domain (FDTD) tool. For the measurement, an UHF long-range reader based on the ThingMagic M5-e ASIC has been used with 0.5dBm resolution in setting the output power. The sensor tag is interrogated by means of a 5dB linear polarized patch antenna connected to the reader and placed 50cm apart from the tag itself. Ground and walls reflections are minimized by using absorbing panels; the turn-on method has been used [22]. From (2.5) it is possible to determine the maximum activation distance, $d_{\text{max}} = 8\text{m}$, by considering

Table 10: Size in [mm] of the parameters in Fig. 80

Parameter	Value [mm]
a	18
b	10
e	2
p	14
L	48
Lp	58
lg	10
W	80
Wp	90

3.2W EIRP, the maximum emitted power from the reader allowed by European regulations.

PEDOT:PSS Characterization

While some information about permittivity and conductivity of PEDOT:PSS are available in DC, its electric properties are not known in the RFID band. At this purposes, the sensor tag itself has been used as dielectric measurement device according to the following parametric identification procedure. The sensing slots have been filled by the polymer as in Fig. 83 and the same structure has been simulated by the FDTD solver: since it is reasonable to assume that the PEDOT:PSS acts as a lossy conductor [98], the conductivity σ_P of the simulated load has been varied such to minimize the difference between measured and simulated tag response in term of the maximum realized gain G_τ :

$$\sigma_P : \Delta_{\text{tot}}(\sigma_P) = \sum_{i=1}^3 \frac{|G_{\tau, f_i}^{\text{meas}}(\sigma_P) - G_{\tau, f_i}^{\text{sim}}(\sigma_P)|^2}{|G_{\tau, f_i}^{\text{meas}}(\sigma_P)|^2} \rightarrow 0 \quad (7.1)$$

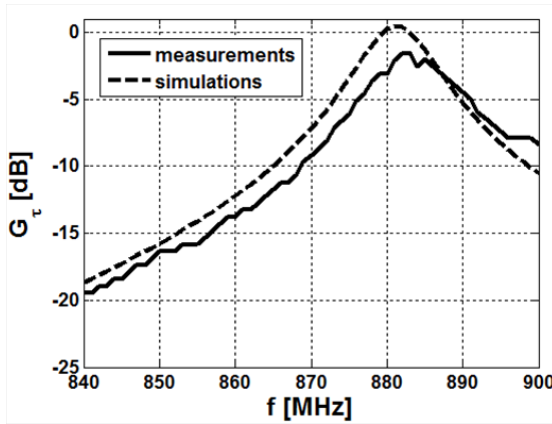


Figure 84: Measured and Simulated realized gain for the unloaded sensor tag

With the observed frequencies $f_i = [860, 870, 880]$ MHz. Two different environmental conditions have been considered: ambient dry air (RH = 50%) and wet air (RH = 100%), such to evaluate also the expected sensing dynamic. To expose the radio sensor to a controlled humidity level, it has been placed inside a closed plastic chamber partially filled with water (Fig. 85). When the chamber is closed, the relative humidity tends to RH = 100% (wet air), while in case the cover is removed the humidity is that of the ambient dry air (RH = 50%). The measurements have been performed at room temperature of 24°C, to be considered stable all along the process.

The error profiles for two humidity conditions (RH = 50% and RH = 100%) are shown in Fig. 86.

The estimated values of σ_P minimizing the global error Δ_{tot} are 5 S/m for RH = 50% and 10 S/m for RH = 100%: the conductivity of PEDOT:PSS approximately doubles going from a ambient dry air to a completely saturated air, sensibly increasing the antenna's losses. A variation of about 6 dB and a frequency shift of about 10 MHz is expected during a complete exposure cycle (RH = 50% \rightarrow 100%).

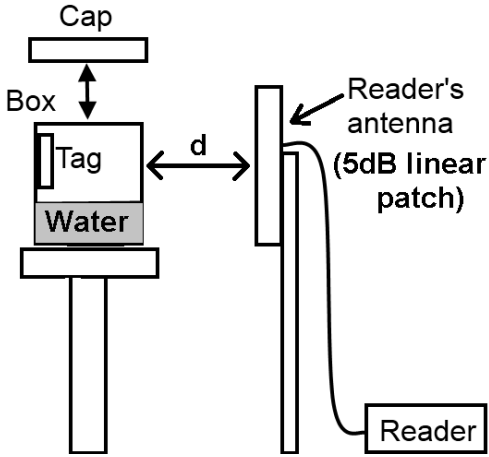


Figure 85: Measurement set-up: the sensor tag is placed into a sealed plastic chamber partially filled with water and 50cm away from the reader's antenna.

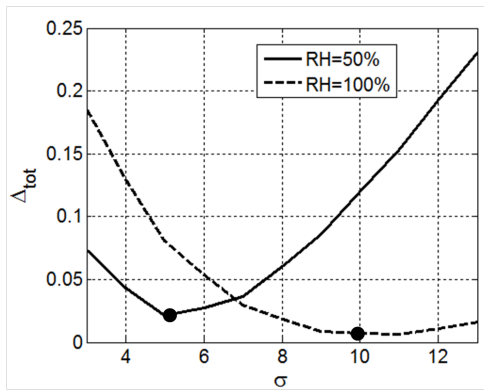


Figure 86: Global error in the parametric identification of the PEDOT:PSS conductivity σ_p for ambient dry air (RH =50%) and wet air (RH=100%).

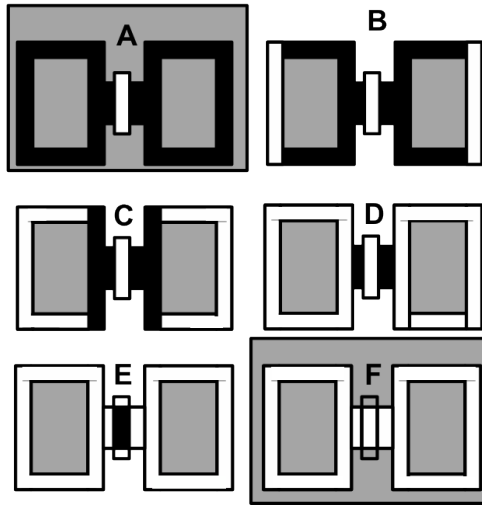


Figure 87: H-slot sensitive area: the sensor tag has been characterized for six different polymer depositions. The first condition (A) corresponds to a complete loading of the slot, the last one (F) to a complete unloaded tag.

7.1.2 Operative characterization

Since there is no decoupling from the operative and structural point of view between antenna and sensor, the proposed device must be characterized and optimized from both perspectives: the main goal is to enhance its sensing capabilities keeping almost unaffected the communication features or at least to find the most suitable tradeoff between the two constraints.

Communication features

The communication performances have been statically evaluated, e.g. without exposure to the humidity, in term of realized gain G_{τ} versus the amount of polymer deposition, schematized in Fig. 87.

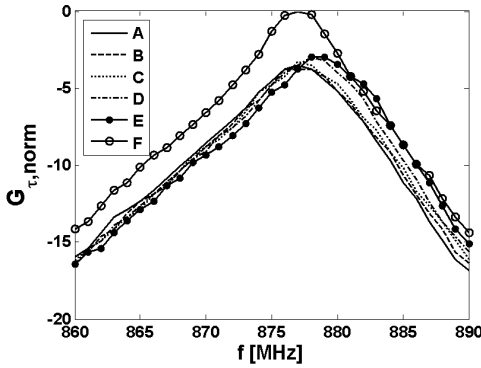


Figure 88: H-slot sensitive area: measured normalized G_{τ} .

The measured profiles, shown in Fig. 88, are normalized with respect to the maximum realized gain of the unloaded tag (case F of Fig.87) as follows:

$$G_{\tau, \text{norm}}(\xi) = G_{\tau}(\xi) - \max(G_{\tau}(F)) \quad (7.2)$$

with the observed different deposition $\xi = [A, B, C, D, E, F]$ of Fig. 87.

It is clearly visible a difference of about 4dB of realized gain between the completely loaded (A- case in Fig.87) and unloaded (F- case in Fig.87) antenna. As the polymer deposition area increases (from E- case to A- case), slight monotonic variations are measured: the frequency shifts of about 2MHz with an attenuation of almost 1dB. However, the strongest variation (almost 3dB) is between case E and case F: even a small drop of PEDOT:PSS sensibly increases the losses of the tag, reducing the expected activation distance from 8m to 5.5m.

Sensing features

The sensing performances of the RFID tag have been dynamically analyzed, i.e. when the humidity inside the box of Fig. 85 gradu-

ally changes from ambient conditions up to saturation, versus the amount of polymer deposited into the H-slot.

Fig. 89 shows the measured variation of the turn-on power $P_{in}^{to}[\text{RH}]$ with respect to the increase of humidity for three different polymer depositions (cases A, C and E in Fig.87). In each case the frequency that guarantees the largest range of variation, i.e the frequency of the minimum turn-on power, has been selected for the measurement. All the configurations are suitable to sense the variation of the humidity according to the typical exponential profiles of conventional active sensors. During the exposure process ($t = 60\text{min}$) the turn-on power increases of about 3.5dB – 6dB depending on the specific PEDOT deposition. It is clearly visible that the wider is the area covered by the polymer, the greater is the water absorption and thus the variation of the radiation performances of the sensor. The sensor's response indeed saturates for a higher humidity percentage. It is moreover worth noticing that during the early grade of the exposure, e.g. for $50\% < \text{RH} < 75\%$ ($t < 10\text{min}$) the slopes of the curves A and C are completely overlapped, and hence a similar response may be achieved by using just half the maximum amount of the polymer. Finally, by observation of curve E, it is apparent that even a single drop of polymer placed right under the IC offers the possibility to detect the humidity's change even if with a smaller sensitivity and dynamic range. The stair-step shaped trend is due to the limited resolution 0.5dBm of the UHF reader.

The normalized AID[RH] profiles for the same depositions are shown in Fig. 90. They show a monotonic exponential profile proportional to the deposition area, but are quite different than P_{in}^{to} especially regarding the dynamic range. The AID reveals to be less sensitive to the humidity: the maximum variation is about 2dB and it is achieved by the A configuration. The slope of the curves is maximum at the beginning of the process, e.g for $\text{RH} = 50\%$, but the profiles are not overlapped as in the turn-on case.

The trends seem confirming the strong influence of the losses induced by the water absorption, since the parameter involving the tag's gain, i.e. G_{τ} , is extremely more variant than the one involving only the input impedance, i.e. AID.

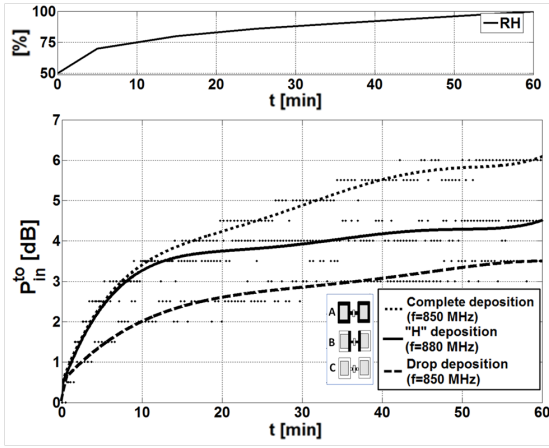


Figure 89: Top) Measured variation of humidity inside the plastic box containing the RFID radio-sensor. Bottom) Turn-on power normalized with respect to its initial value, e.g. at ambient RH, for three different polymer depositions into the H-slot. Measured data (discontinuous dots) have been fitted by a mean square interpolation.

As for conventional sensor, also in this case it is possible to determine the calibration curves, e.g. the plots of the sensor response versus the variation of the humidity. The normalized values of turn-on and backscattered power respect to the initial condition are visible in Fig. 91. The profiles appear almost linear, especially for low humidity grades. The slopes of the curves are in general proportional to the deposition area, except for the early stage of the process. As expected, the curve relative to the drop deposition is the less steep. From Fig. 91 it is possible to extract the sensitivity of the device (2.9), e.g. the power difference generated by one percent change in the RH level:

$$S_{\xi} = \frac{|\Delta\xi|}{|\Delta RH|} = \frac{|\xi(RH_{high}) - \xi(RH_{low})|}{|RH_{high} - RH_{low}|} \quad (7.3)$$

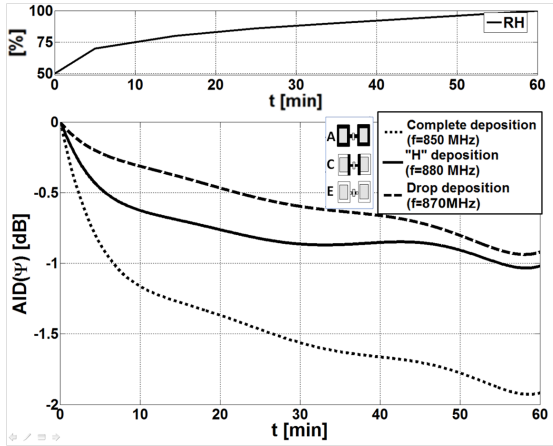


Figure 90: Top) Measured variation of humidity inside the plastic box containing the RFID radio-sensor. Bottom) AID normalized with respect to its initial value, e.g. at ambient RH, for three different polymer depositions into the H-slot. For clarity only the fitting curves are shown.

where $\xi = \{p_{in}^{to}, p_{BS}\}$. The values for the three depositions of Fig. 91 are listed in Table 11.

Degree of load and humidity absorption jointly contribute to weaken the communication robustness of the proposed device. Depending on the required sensitivity and on the range of humidity it has to be monitored, it is thus necessary to reduce the amount of load to the bare minimum: in fact the smaller the quantity of polymer spread in the sensing slots is, the better the communication performances can be preserved all along the sensing process.

7.1.3 Cyclic Exposure

Once the sensor has been calibrated and the communication performances characterized, it is tested in a realistic scenario in order

Table 11: Turn-on and backscatter Sensitivities [dB/RH].

	RH _{low} – RH _{high}	Case A	Case C	Case E
S _{P_{in}} ^{pto}	50% – 80%	0.13	0.12	0.08
	80% – 100%	0.1	0.05	0.05
S _{P_{BS}}	50% – 80%	0.18	0.2	0.12
	80% – 100%	0.13	0.05	0.05

to verify the effectiveness of its features, the recovery and the possible hysteresis.

The sensor with intermediate polymer deposition (case C of Fig.87), has been exposed to two cyclic variations having different duration (and extent) between wet and dry air, with the purpose to better characterize the reproducibility of its response. The results are given in terms of turn-on power and backscattered power. The profiles are visible in Fig. 92 for the selected frequency of 880MHz, which ensures the strongest signals variation during the process.

The change of the RFID powers reasonably follows the variation of the humidity with different profiles. For the turn-on power, the dynamic range is about 5dB in the first exposure cycle $0 < t < T_1$ (RH =50% → 100%) and about 3dB in the second cycle of shorter duration $T_1 + T_2 < t < T_1 + T_2 + T_3$ (RH =50% → 90%). At the same frequency, the backscatter indicator has a variation of about 7dB in the first cycle and 5dB in the second one.

The recovery process at RH=50% takes place after the two cycles humidity exposure during $T_1 < t < T_1 + T_2$ and $T_1 + T_2 + T_3 < t < T_1 + T_2 + T_3 + T_4$. As the box is opened the relative humidity drops to the value of ambient air and the radio sensor starts its recovery. After a period $T_2 = 60$ min the recovery can be considered completed, however, just 5min are enough for the sensor to recover 3dB of turn-on power and 4dB of the backscattered power.

The effects are reversible, with a negligible hysteresis: once the baseline value have been reached, the response remains stable with only 1dB of difference between the beginning and the end of the process. Finally the comparison with the response of a “blank”

tag, e.g without polymer deposition and subjected to the same cyclic exposure as before, further demonstrates the effectiveness of the proposed sensor. As clearly visible in Fig.92, the “blank” tag shows a remarkable small variation (± 1 dB) only due to the formation of water drops over the copper tag.

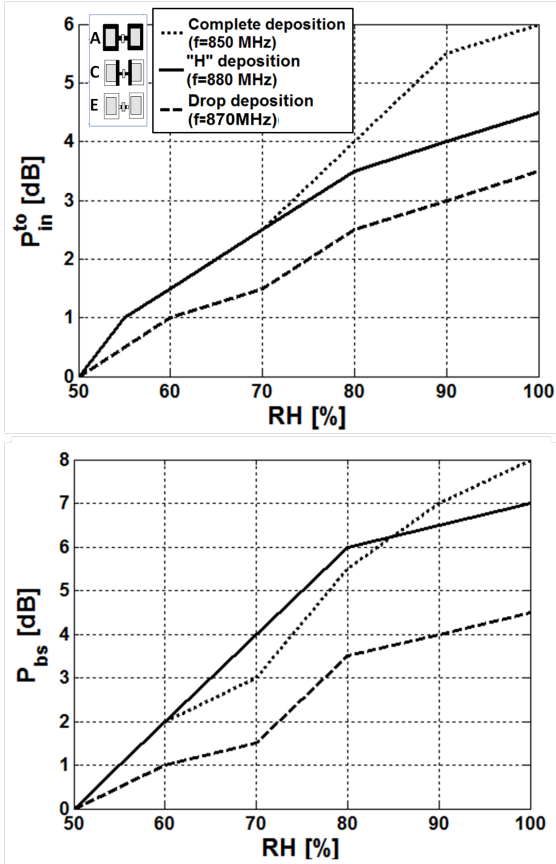


Figure 91: Calibration Curves of the humidity RFID sensor. Top) Turn-on power; Bottom) Backscattered power.

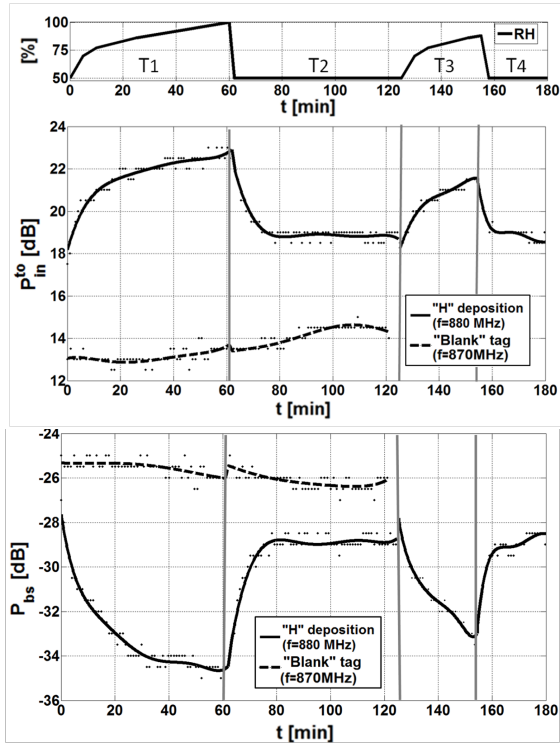


Figure 92: Measured turn-on and backscattered power normalized with respect to the turn-on power during cyclic exposures. Also the power from the “blank” tag is visible. Here $T_1=60$ min, $T_2=60$ min, $T_3=30$ min, $T_4=30$ min.

7.2 GAS SENSOR

The first part of the analysis will be focused on the fabrication and characterization of the SWCNT *buckypaper*, to be used as part of the radio-sensor. The design of the RFID passive radio sensor is then discussed in Sec. 7.2.2 by means of equivalent circuit model and experimentations. Finally, in Sec.7.2.3 the sensing features of the CNT-based RFID tag are fully investigated in the American and European UHF band, by means of many experimental tests.

7.2.1 SWCNT Material Preparation and Characterization

Several deposition techniques have been proposed for CNT-based antenna and electronics: inkjet and screen-printing procedures [21], CVD processes [97] and thin films [96] are recent examples of useful techniques able to offer high conductive CNT samples.

SWCNT film, also referred to as *buckypaper*, offers isotropic conductivity, good mechanical strength and flexibility and gives the possibility to easily cut out the shape of the desired antenna [101]. The fabrication procedure generally consists in filtering SWCNT suspension in aqueous or organic media, such as Triton X-100 or dimethyl formamide (DMF), under positive or negative pressure.

In this work, an alternative preparation method is presented, where the filtration over membrane has been replaced by evaporation in a controlled environment. The process is schematically shown in Fig.93. A 100mg purified, high functionality with carbonaceous purity $\geq 90\%$ SWCNT powder from Carbon Solutions, Inc has been dispersed in 66mL of water by sonication at 30W for 60min. Next, in order to get rid of the water and form the CNT buckypaper, the dispersion has undergone an overnight evaporation at 70°C. Finally a circular sheet with diameter $d = 90\text{mm}$ has been produced over a polyamide membrane. The thickness of the buckypaper is determined by the total amount of CNTs used in the dispersion per unit surface of the membrane, since the water is removed during the evaporation process. It can be evaluated in first approximation by a simple mathematical proportion with the density and the thickness achieved in [102]. With a calculated

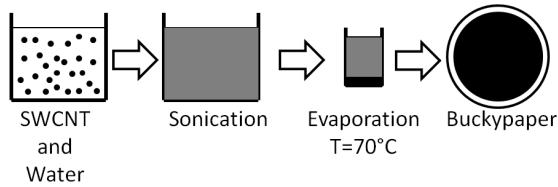


Figure 93: Buckypaper preparation steps.

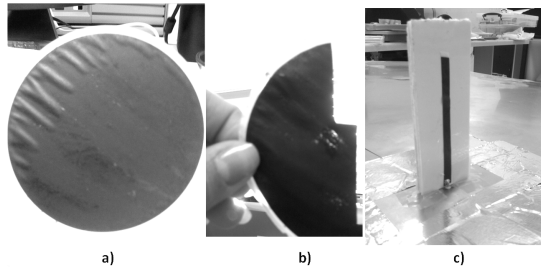


Figure 94: CNT Buckypaper a) prepared sample b) irregularities of the sample towards the center c) CNT buckypaper monopole over the ground plane

density $S = 1.6 \times 10^{-2} \text{ mg/mm}^2$ the thickness results to be about $32 \mu\text{m}$.

The sonication and the evaporation/filtration procedures are extremely critical for optimizing the CNT buckypaper performance. Large CNT agglomerates in the CNT solution will dominate leading to a brittle film, as well as a non uniform evaporation produces a non uniform sheet with holes and consequently non isotropic conductive performances. Fig.94 shows the result of the process: the CNT buckypaper appears macroscopically uniform (a), but some undesired inconsistencies are present at the center of the sample (b) leading to poor and not uniform conductivity and mechanical properties.

RF Characterization

The dielectric properties of CNT are strictly dependent on their deposition techniques. Concentration, orientation, number of layers and material type are important parameters that affect the performances of the nanotubes, especially at RF. Although several characterization data have been presented, especially in DC, the dielectric properties at RF are not univocally defined, making it necessary to preliminarily characterize the produced buckypaper. Here, an indirect method, using both measurements and computer simulations, has been used to refine the different values available in the literature according to our specific sample. Based on the assumption that CNT can be considered a lossy metal (with finite conductivity σ), several strips of the CNT buckypaper of size $80\text{mm} \times 5\text{mm}$ were cut out of the membrane and plated on foam substrates in order to form monopole antennas in the RFID UHF frequency band. Fig. 94 c) shows the picture of one of the monopole antennas used in the measurement setup. A silver epoxy mixture was applied at the interface CNT antenna - SMA connector and cured to improve their electrical and mechanical connectivity. The input impedance of the CNT antennas has been measured by means of a Vector Network Analyzer (VNA Rohde&Schwarz ZVA8). In parallel, FDTD simulations were performed by varying the unknown σ around the value available in literature. The CNT layer was accounted by a surface impedance model. A root mean square (r.m.s.) minimization has been finally applied in order to fit the measured and simulated input impedances and thus evaluate the conductivity. The optimum value obtained for the buckypaper after averaging on different monopole geometries was $\sigma \approx 2.5\text{S/m}$.

Sensing Characterization

The response of the CNT to the ammonia is here investigated by analyzing the variation of the radiation performances of one of the previous monopoles (size $80\text{mm} \times 5\text{mm}$), in term of both input impedance and transmission characteristics.

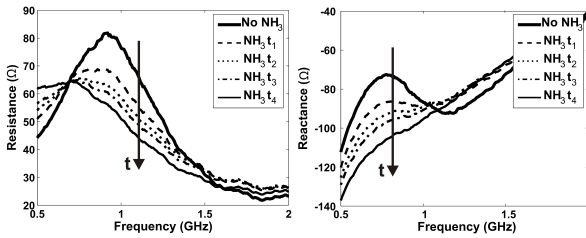


Figure 95: Z_{in} results of the monopole CNT antenna of Fig. 94 with and without the presence of the NH_3 . Here $t_1 = 1\text{min}$, $t_2 = 5\text{min}$, $t_3 = 10\text{min}$, $t_4 = 15\text{min}$

INPUT IMPEDANCE Fig.95 (thick line) shows the measured Z_{in} of the CNT antenna before the exposure to ammonia. As expected, due to the very high losses, the monopole is strongly capacitive with a $-110 \leq jX_{in} \leq -70 \Omega$ and with a resistance $30 \leq R_{in} \leq 80 \Omega$.

A volume of 6ml of commercial off the shelf 10% ammonia hydroxide was then guided into the 460cm^3 plastic chamber surrounding the monopole. Upon the addition of the ammonia, a quick and strong variation of the monopole impedance was recorded. This is shown in Fig. 95 where t_1 implies the time the measurements were recorded right after the introduction of the gas. The effect is monotonic for both R_{in} and X_{in} during the whole exposure $t_4 - t_1 \approx 15\text{min}$. As time progresses, slight saturation in the recorded measurements is observed.

The recovery of the Z_{in} to its initial value was monitored after removing the ammonia from the chamber (Fig.96). As in the exposure process, the variation is monotonic but much slower (here $t_3 - t_1 \approx 1\text{hour}$). A slight difference between the input impedances before the exposure to ammonia and after the recovery phase is observed as well, demonstrating the quite irreversible effect of the NH_3 on the CNT. This effect is well known in the literature [93], and it is caused by the nature of gas absorption and desorption process to the nanotubes.

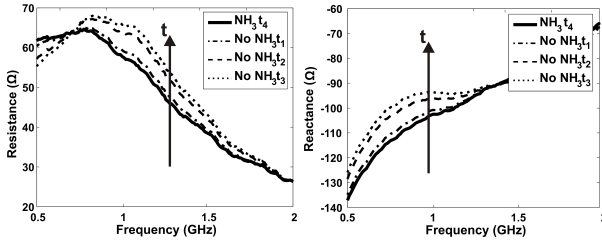


Figure 96: Z_{in} recovery features of the monopole CNT antenna of Fig. 94 after ammonia removal. Here $t_1 = 10\text{min}$, $t_2 = 30\text{min}$, $t_3 = 60\text{min}$.

TRANSMISSION Two identical CNT monopoles fabricated as before are now faced and separated by 20 cm to measure the transmission characteristics or S_{21} with and without NH_3 . This measurement gives an evaluation of the variation of the gain in the presence of gas, which is proportional to the $|S_{12}|^2$ between the two antennas [103]. Only one monopole is exposed to the ammonia, according to the setup previously described. The measured S_{21} are shown in Fig. 97 upon adding NH_3 (a) and upon its removal (b). The measurement times are defined similarly to those of Fig. 95 and 96, with $t_4 - t_1 \approx 15\text{min}$ in the exposure process and $t_3 - t_1 \approx 1\text{hour}$ for the recovery.

Without ammonia (Fig. 97 thick line) the S_{12} has in the UHF band an average value of about $\sim -40\text{dB}$, suggesting the low conductivity of the radiating structures. Similarly to the input impedance, the S_{12} changes monotonically in presence of gas as time progresses. It is observed that a quick response takes place upon the addition of NH_3 , as well as saturation phenomena as $t \rightarrow t_4$. The transmission performance deteriorates as the antenna is exposed to NH_3 , losing almost 7dB. This effect seems to confirm a decrease in conductivity, as experienced in [21] and [93]. This can be explained considering that this gas is a reducing agent that injects electrons to the nanotubes (p-type) reducing the number of holes and hence the conductivity.

Recovery features are still present, but slower than in the previous experiment. The permanent effects of the gas are clearly

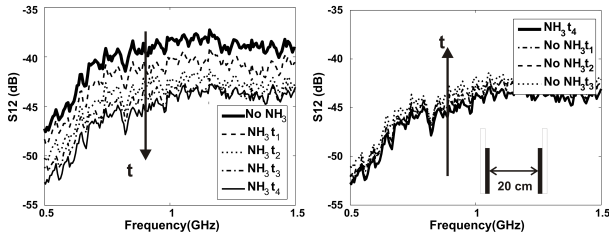


Figure 97: S_{12} variation between two identical CNT monopole antennas with and without the presence of the NH_3 .

visible: the recovery variation is about 4dB, almost half of the one achieved during the exposure process.

From these experiments it is hence clear that the presence of ammonia affects both the impedance and gain of the monopole, potentially promising interesting applications in the RFID domain.

7.2.2 RFID Gas Sensor: design and prototype

There are several options to achieve a gas-sensitive tag taking advantage of the sensing feature of the CNT demonstrated in Sec.7.2.1. A first classification could be done considering the CNT as a part of the antenna radiating structure, e.g. an antenna totally or partially made of nanotubes, or considering instead the buckypaper as a doping component of the tag, e.g. a variable load properly placed in close proximity of the radiating elements [21]. Both solutions offer advantages and drawbacks; the best trade-off between communication and sensing must be finally adopted. By considering CNT as a radiating element, it is possible to maximize the gas sensitivity of the device, however lowering the antenna efficiency and the activation distance of the RFID tag. These two parameters, together with the cost, are essential in RFID systems. The other solution, on the contrary, offers better communication and cost performances but could provide a weaker sensitivity to the gas.

In this work, CNT film is used as a loading impedance of a conventional RFID passive tag [21]. The considered antenna layout

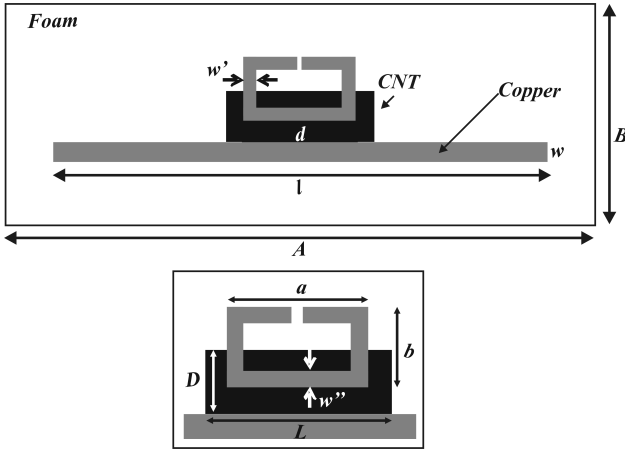


Figure 98: RFID Tag: Inductively Coupled Loop with a rectangular CNT load. The matching to the IC can be achieved for example by acting on the parameter d and a and by fixing the others.

is a copper dipole with an inductively coupled loop [18], matched to an NXP IC with complex impedance $Z_{\text{chip}} = 16 - j148 \Omega$ and sensitivity $P_{\text{chip}} = -15\text{dBm}$. In this geometry (Fig. 98), the strength of the coupling is controlled by the distance d between the loop and the radiating body, as well as by the shape factor (a, b) of the loop. A rectangular sample of CNT buckypaper (of size $D \times L$) is thus placed in the space between the loop and the radiating dipole, being this area the most critical for the antenna's radiation performances.

The CNT film affects the coupling between the two structures, modifying the current's distribution and consequently the input impedance of the tag. More specifically, the presence of the CNT film between the dipole and the loop produces a current flow between the two copper structures (Fig.99), whose effect competes against the one produced by the inductive coupling: for extremely low conductivity the prevailing effect is inductive, while, as well as the conductivity increases, the ohmic effect becomes stronger and the structure resembles, from a current point of view, a T-

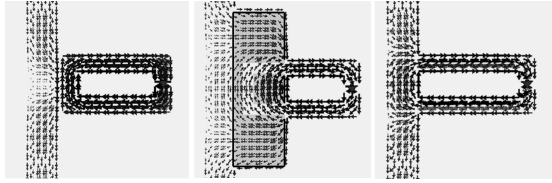


Figure 99: Current distribution simulated by FDTD method. Left) Standard loop fed dipole (no CNT); Center) Loop fed dipole integrating CNT; Right) Conventional T-match dipole. Although the magnitude is quite similar, the currents are sensibly different in the CNT area, making the antenna very similar to the T-matched one.

match feed [18]. Two different effects are hence present: ohmic currents that flow along d and a variation of the shape factor of the loop (see Fig.99 center). As visible, the currents tend to reduce the length of the loop, flowing all along the surface and the perimeter of the CNT area. Both real and imaginary part of the input impedance are accordingly dependent on the lossy CNT material.

Circuit Model

Under the hypothesis that the CNT can be considered as a lossy metal with variable conductivity, the input impedance of the radio sensor and its variation with the CNT conductivity can be described by the general equivalent circuit in Fig.100. The circuit has been obtained through a proper modification of the topology described in [18] whose impedance transformer is here replaced by its T-model equivalent by introducing the series impedances:

$$Z_1 = j\omega L_d - Z_T \quad (7.4)$$

and

$$Z_2 = j\omega L_l - Z_T \quad (7.5)$$

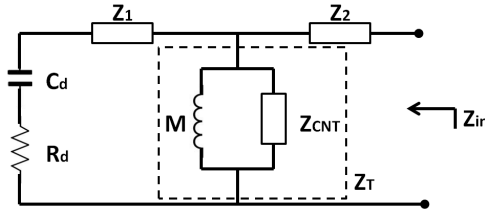


Figure 100: RFID radio-sensor integrating CNT equivalent circuit. A T-model has been adopted to represent the transformer in [18]. The parameters R_d , C_d , and L_d (for clarity grouped in Z_1) give the input impedance Z_A of the radiating body near its (series) resonance.

where $Z_T = j\omega M \parallel Z_{CNT}$ is the modified impedance of transformation, which takes into account the presence of CNT (Z_{CNT}) and of the mutual inductance M only related to the geometry of the structures [104]. L_1 is the loop inductance and finally $Z_A = R_d + 1/j\omega C_d + j\omega L_d$ the input impedance of the radiating body around its first resonance. The presence of the CNT film impacts on the coupling between the dipole and the loop, so that the input impedance at the chip port is finally given by

$$Z_{in} = j\omega L_1 + \frac{(Z_T)^2}{Z_A} \quad (7.6)$$

Z_{CNT} is related to various CNT's parameters, such as its size, its conductivity and the consequent skin effect δ_s . It is roughly proportional to the surface impedance of imperfect conductors [105] and can be evaluated by means of best fitting of the numerically computed input impedance to the circuital expression in (7.6), in order to take into account the specific shape factor of the film. For the particular structure described in Fig.98:

$$Z_{CNT} = f(\sigma, \text{shape factor}_{CNT}) \approx K_1 \frac{(1+j)}{\sigma \delta_s} \quad (7.7)$$

where $\delta_s = \sqrt{2/(\omega\mu_r\sigma)}$ is the skin depth, $\mu_r = 1$ is the relative magnetic permeability of conductor and σ its conductivity. The loop inductance L_1 is mainly related to the geometric features of the structures [104], however, as shown in Fig.99(center), the presence on the CNT film in the inner part of the loop strongly modifies its current distribution, essentially reducing the overall perimeter of the effective current loop. The width of the horizontal segment $w''(\sigma)$ (in Fig.98) can thus be properly corrected to include this effect as:

$$w'' \approx w' + (K_2\sigma + K_3) \cdot a \quad (7.8)$$

with weights $K_{2,3}$ to be defined through linear fitting.

It is worth noticing that for extremely low conductivity ($\sigma \rightarrow 0$), the CNT impedance becomes an open circuit ($Z_{CNT} \rightarrow \infty$) and $Z_T \rightarrow M$ as for the standard inductively coupled structure, while for $\sigma \rightarrow \infty$, $Z_{CNT} \rightarrow 0$ and $Z_T \rightarrow 0$ (ohmic contact), giving rise to a T-match feed.

The circuit model in Fig.100 is of general application and could be used to support the design of other gas sensors integrating CNT with different conductivity σ , as well as to understand how this last parameter affects the tag's radiation performances. It is however worth noticing that since the circuit represents an hybrid between the T-match and the inductively coupled loop, it is reasonably valid only for relative low values of σ : as the conductivity increases more suitable equivalent circuit model should be used to describe the T-match like structure [18].

Parametric Analysis

Fig.101 shows an example of parametric analysis, computed by the equivalent circuit model, for the loop-driven dipole in Fig.98 loaded by a 30mm \times 10mm CNT buckypaper with $\sigma = 2.5S/m$ as evaluated in Sec.7.2.1, when varying the shape factor of the loop a and its distance from the dipole d . Such analysis has been compared with the one produced by the fullwave FDTD simulation. For the particular geometry of CNT, the following

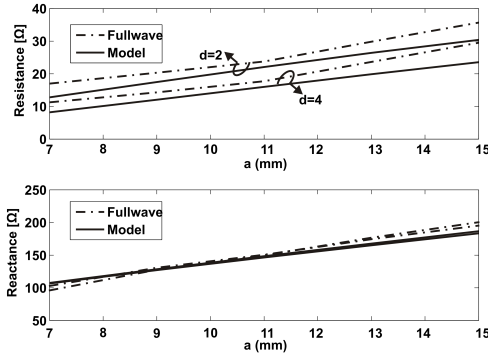


Figure 101: Parametric analysis of the input impedance varying the shape factor of the loop and its distance from the vertical dipole, having fixed (size in [mm]) $l = 160, w = 5, L = 30, w' = 2, b = 22, D = 10$.

weights have been found by linear fitting $K_1 = 1.7, K_2 = 6 \cdot 10^{-2}$ and $K_3 = -4 \cdot 10^{-2}$.

The input reactance is nearly unaffected by the loop-dipole distance d . For a fixed loop size, instead, the resistance reduces when the loop-dipole distance increases. For the particular choice of parameters as $a = 10\text{mm}$ and $d = 2\text{mm}$, the predicted antenna impedance is $Z_{in}(a, d) = 17 + j140 [\Omega]$, very close to the required value to match the NXP IC.

For this size of the loop, the variation of the input impedance at 915MHz with conductivity is shown in Fig.102 for $\sigma = [1, 5]\text{S/m}$.

As expected from physical considerations, the variation of CNT conductivity impacts both the real and the imaginary part of the input impedance. They monotonically decrease as the conductivity increases, according to different variation profiles. In percentage terms, the effect is stronger on the input resistance, since the reactance is mainly governed by the shape factor of the loop as indicated in Fig.99. Moreover, the presence of CNT will modify the losses of the tag, producing also a variation of gain.

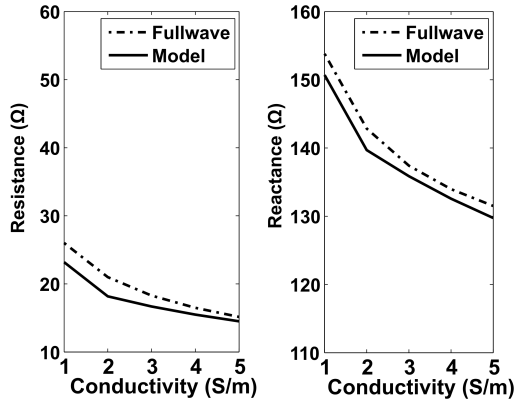


Figure 102: Change of the input impedance of the loaded RFID tag with conductivity.

Prototype

A first prototype of the tag is shown in Fig.103. Voyantic Tagformance is used for the characterization of the RFID response of the tag. The interrogator antenna is a Kushcraft patch having a 6dBi gain and a circular polarization. The reader's antenna-tag distance is fixed to $r = 63.5\text{cm}$. Both the reader and the tag are 101cm high from the floor. All the measurements have been performed in an anechoic chamber.

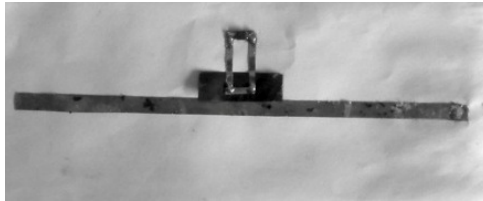


Figure 103: Photo of the Prototype. Size in [mm]: $A = 180, B = 80, l = 160, w = 5, L = 30, w' = 2, a = 10, b = 22, D = 10, d = 2$.

The measured AID (2.7) and realized gain G_τ (2.6) are shown in Fig.104 for three different orientations. The AID is independent of the reader-tag mutual position [15], while the realized gain is rather sensitive to the reader-tag orientation due to the variable gain of the tag over the H-plane. Simulation and measurements have been compared along the normal direction, e.g. when the tag is placed exactly in front of the reader. Although there are some deviations at the lower and higher frequencies, basically due to the non linearity of the IC, they reasonably fit around the designed frequency 915MHz, as shown in Fig.104.

It is important to point out the effect of the CNT buckypaper on the radiation performances of the tag. The maximum measured realized gain is around -7dB , that implies a simulation gain of about -6dB , worse than typical gain for this kind of antenna (0-2dB) due to the presence of a lossy loading.

The maximum reading distance r_{Max} can be evaluated from (2.1) enforcing $P_{\text{R} \rightarrow \text{T}} = P_{\text{chip}}$. Taking into account the measurement results and considering a reader emitting up to 4W EIRP in linear polarization, the estimated maximum read distance is 4m.

7.2.3 Sensing Characterization

To test the sensing performances of the tag, it has been placed into a 684cm^3 plastic gas chamber, and a volume of 6ml of 10% ammonia hydroxide was guided into it (Fig.105). The reference condition for the tag, without ammonia, accounts for the presence of the gas chamber in close proximity of the radiating structures.

Fig. 106 shows the results of the $P_{\text{in}}^{\text{to}}[\Psi]$ for the tag-under-test (TUT) following the exposure to NH_3 . The measurement time-steps are indicated in Tab.I. An immediate and sharp variation of response is observed at $t_1 = 1\text{ min}$ followed by a saturation. Within the band of interest, the behavior is monotonic, with about 2dB of overall variation. Since the turn-on power is inversely proportional to the realized gain $G_\tau = G_T \cdot \tau$ of the tag, the diagrams in Fig.106 suggest that the tag performances improve along with the exposure to ammonia. This behavior seems to be in contrast with the two CNT-monopoles experiment in Fig.97 wherein $|S_{12}|^2$ reduces as $[\text{HN}_3]$ increases. A possible explanation is that the

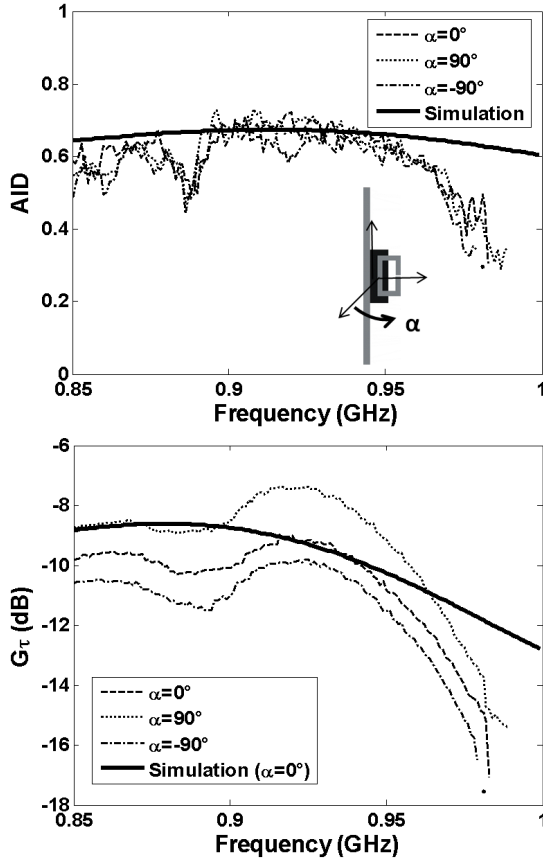


Figure 104: Simulation and Measurement results for G_τ and AID for the CNT-loaded RFID prototype.

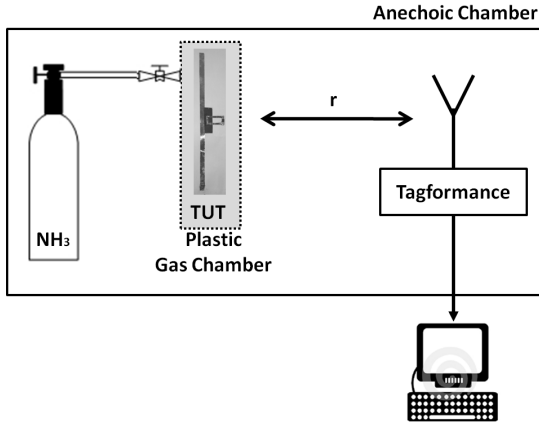


Figure 105: Measurement setup comprising the remotely controlled reader, the ammonia tank connected to the gas chamber and the RFID tag under test (TUT). The reader's antenna-tag distance is fixed to $r = 63.5\text{cm}$

presence of ammonia tends to improve the impedance matching (τ) between the tag and the microchip. A more detailed chemical analysis of the absorption should be nevertheless required to fully understand this effect.

It is worth noticing that the time required to take a complete measurement of data (840-980 MHz) is approximately 90 sec and thus it may be comparable with the response time of the sensor (approximately 2 min according to [93]). This could affect the accuracy of the data especially at higher frequencies since the absorption of the ammonia and thus the electromagnetic features of the CNT are changing in the meanwhile the measurement is performed. However, for the two UHF RFID frequencies considered in the paper (European and American band) the measurement time can be assumed to be less than 40 sec and hence the measurement artifact could be considered negligible.

The visible variation of $G_{\tau}[\Psi]$ and $AID[\Psi]$ in the presence of NH_3 (Fig.107) confirms that both input impedance and gain are affected by the gas. As expected, the latter indicator is more

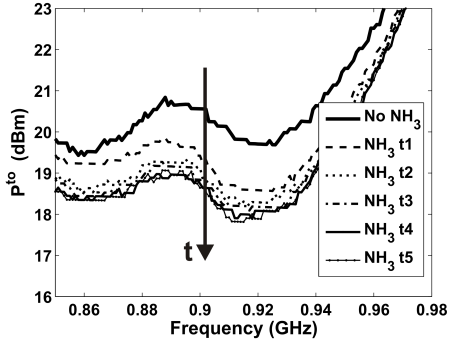


Figure 106: Turn on Power of the CNT loaded RFID Tag with NH₃.

Table 12: Exposure and Recovery measurement time-steps

Exposure time	Recovery time
$t_1 = 1\text{min}$	$t_1 = 5\text{min}$
$t_2 = 4\text{min}$	$t_2 = 13\text{min}$
$t_3 = 6\text{min}$	$t_3 = 40\text{min}$
$t_4 = 9\text{min}$	$t_4 = 50\text{min}$
$t_5 = 15\text{min}$	$t_5 = 60\text{min}$

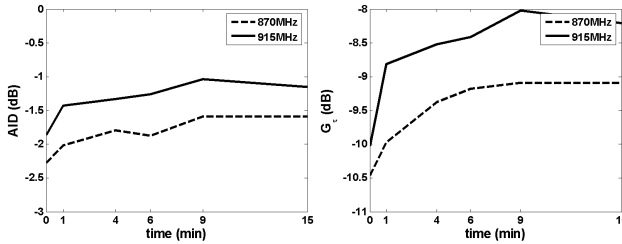


Figure 107: G_{τ} and AID for the CNT-loaded RFID prototype with NH_3 .

sensitive to the NH_3 than AID, due to the additional dependence on the tag's gain $G_{\tau}[\theta, \phi, \Psi]$.

It is useful to analyze also the percentage variation of realized gain ΔG_{τ} and AID ΔAID as in (2.8). The maximum variation for both indicators arises just after the ammonia introduction, more specifically $\Delta G_{\tau}(t_1) = 30\%$ and $\Delta \text{AID}(t_1) = 10\%$. The total variation is $\Delta G_{\tau}(t_5) = 60\%$ and $\Delta \text{AID}(t_5) = 20\%$ and seems to be maximum at 915MHz.

Recovery Features

Fig. 108 and Fig.109 show the recovery plots of $P^{t_o}[\Psi]$, $G_{\tau}[\Psi]$ and $\text{AID}[\Psi]$ vs frequency after having removed the ammonia. A monotonic recovery characteristic is present, with a slower response (see Tab.I for all the recovery time steps), mainly occurring in the first 15 min.

Although G_{τ} shows clear recovery features, the AID seems quite insensitive to the phenomena, especially at 870MHz. This issue could be related to the fact that the dependence of the latter indicator only on the input impedance of the tag makes it less sensitive to the physical variation of the antenna.

When considering the whole cycle, it is apparent that the presence of ammonia irreversibly modifies the tag's radiation performances, producing an hysteresis in both input impedance and gain (Fig.110). A difference of about 10% in the turn-on power is indeed observed between the initial condition (without ammonia) and the final condition (after recovery).

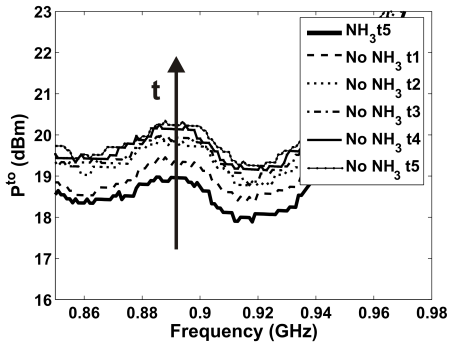


Figure 108: Turn on Power of the CNT loaded RFID Tag - Recovery.

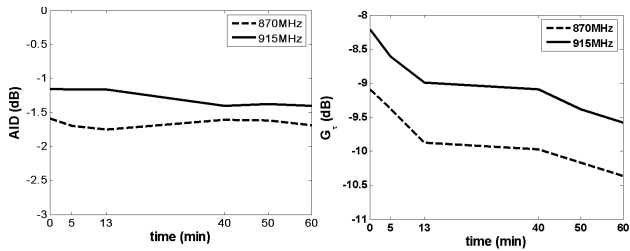


Figure 109: G_{τ} and AID for the CNT-loaded RFID prototype with NH_3 -Recovery.

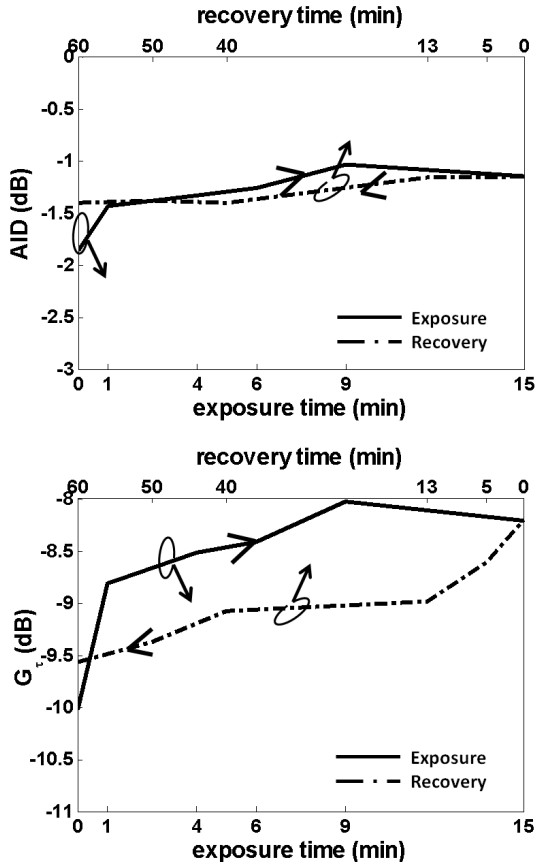


Figure 110: G_{τ} and AID at 915MHz during the exposure and the recovery process

7.3 CONCLUSIONS

The complete integration of CNT film and PEDOT:PSS into RFID tag has been here reported aiming at designing and testing fully working passive radio-sensors suitable to monitor the quality of the air in term of humidity and toxic gases.

A new wearable antenna, suited to be doped with different sensitive materials have been introduced, with interesting features in term of localization and reduction of the material's amount.

Simplified fabrication procedures as well as indirect RF characterizations for the CNT buckypaper have been proposed with promising results in term of feasibility and accuracy. The proof of concept of using CNT-antenna and CNT-based passive RFID Tag as NH_3 wireless sensors has been theoretically and experimentally verified in spite of the strikingly low σ of the tested samples.

Beside the promising early results, the optimization of this class of chemical-doped RFID tags is still prone to considerable improvements concerning the technology process to produce and deposit the load, the antenna design and not least the interrogation algorithm. Depending on the load preparation technique and process, in fact, the properties and the behavior of the radio-sensors can significantly vary, and this is a very crucial issue for the large-scale production of chemical-based devices. Furthermore, in order to design efficient sensing systems, it is necessary to quantify, and especially to enhance, the sensitivity of the films, as well as its response time and selectivity.

Regarding the CNT, the proposed fabrication procedure seems indeed to offer great opportunities in term of cost and simplicity, but it should be better controlled and optimized in order to get defect-free and reproducible sensitive films at the cost of the lowest CNT amount. Possible improvements of the proposed evaporation technique can be achieved by producing smaller area of buckypaper in order to better control the uniformity of the deposition and reduce the required amount of nanotubes. Functionalized CNT should be considered for increasing the gas-sensitivity. The long recovery time, which could be a limiting issue for real-time monitoring of oscillating events, could instead find interesting application for one-shot sensor, e.g. by taking advantage on the

permanent physical modifications especially visible in the AID response.

In order to fully control the tag's behavior in time-varying boundary conditions, the electromagnetic design of the radio sensor needs further refinements for instance by employing multi-physics models.

Finally, the interrogation of the tag in real-world environments could present big challenges, especially concerning the natural fluctuation of the electromagnetic responses caused by multipath. If the measurement is performed in static conditions, e.g. the mutual position between the reader and the sensor tag remains unchanged during the whole phenomenon to monitor, or similarly a same measurement set-up can be exactly replicated in successive readings, the turn-on indicator gives a feasible and sharp response. More in general, the AID metric could be a solution to reduce the reading uncertainties but further effort is required to better enhance its dynamic range in a controlled way.

Part II

SENSING FROM INSIDE

REQUIREMENTS AND FEASIBILITY

This Chapter introduces the main issues concerning the possibility to use RFID implanted radio-sensors to monitor biological process in evolution. Numerical investigations based on realistic clinical cases are devoted to prove the feasibility of the approach in term of communication and sensing performances, finally corroborated by an early experiment campaign with liquid human phantoms.

The possibility to monitor processes in evolution, discloses interesting opportunities in Telemedicine and Human Health Monitoring in general, especially concerning implantable devices. One or more battery-less RFID radio-sensors could be integrated into implanted medical devices such as prosthesis, sutures, endovascular devices and orthopedic fixings, and then interrogated by an external reader (Fig. 111). By data acquisition at different times (days or even hours), the change history of geometrical or chemical features of the tissues could be collected, thus observing in an indirect way the healing process and possible complications, e.g. abnormal cell proliferations, edema and inflammatory events.

In general, the critical issues in the design of implanted radios are a reasonable link range [106], low power consumption [107], biocompatibility [108] and miniaturized packaging [109]. Implanted RFID tags were used in the past for tagging animals. Passive devices for human identification purposes have instead been proposed very recently in [110], as well as implantable antennas suitable to host biological sensors (blood-pressure, temperature, glucose). Patch-like antennas [106] and monopole-like antennas

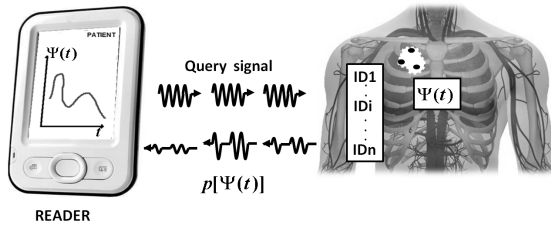


Figure 111: The change of the electromagnetic response p of implanted RFID tags may be related to a biologic process in evolution $\Psi(t)$ inside the human body.

[111] have been studied for subcutaneous implants, while first examples of ingestible RFID capsules interrogated by a wearable reader can be found in [112].

Up to now, no attempt has been reported, according to our knowledge, to obtain sensing capabilities from passive RFID implanted tags in addition to more traditional identification codes. Beside the critical issues shared by conventional RFID and implanted antennas, the very big challenge is the control of the sensitivity and of the dynamic range of the tag-as-sensor during the design task in addition to the usual communication requirements.

Biological processes are characterized by a great variety of dynamic ranges in terms of evolution timeline and amplitude (see for instance Tab.13). Some pathologies may show very slow and moderate evolutions, while in other cases, especially during acute events, rapid and large tissues modifications may be observed. The measurable response of RFID radio sensor needs therefore to be properly correlated to the process under observation. In this view, this thesis demonstrates, for the first time, that the self-sensing concept may be successfully applied to human body processes, and proposes a procedure to assist the design of such class of devices with specific attention to the sensing performances.

The dissertation makes use of numerical electromagnetic simulations to study some realistic pathological processes, such as liver cancer [113] and brain edema evolution [114], corroborated by

Table 13: Healthy and Unhealthy human tissues: dielectric property at 870MHz

Tissue	Healthy	Unhealthy
Brain White Matter	$\bar{\epsilon} = 38.9 - j12$	$\bar{\epsilon} = 50.2 - j20.78$ Brain Edema [115, 114]
Liver	$\bar{\epsilon} = 46.9 - j17.4$	$\bar{\epsilon} = 64.1 + j27.85$ Cancer [116] $\bar{\epsilon} = 61.7 + j28.68$ Cirrhotic Tissue [116]
Treated Vessels	$\bar{\epsilon} = 61.4 - j31.5$	$\bar{\epsilon} = 55 - j19.2$ Neointimal Proliferation[117] $\bar{\epsilon} = 5.46 - j1.04$ Atherosclerotic plaque [118]

preliminary laboratory experiments with a tag prototype placed inside a liquid body phantom and subjected to a controlled local permittivity variation.

8.1 CASE STUDY: LIVER CANCER AND BRAIN EDEMA

The Human body is characterized by dishomogeneous lossy tissues and the physiological or pathological events in evolution are generally localized in regions which are small in term of wavelength. The effective dielectric contrast experienced by an implanted antenna could be therefore rather modest and the in-body sensing may become very challenging. In order to test the feasibility of the proposed methodology, two realistic clinical cases are

	870MHz	
	ϵ_r	σ [S/m]
Skin	41	0.85
Fat	5.46	0.05
Bone	12.48	0.14
Dura	44.5	0.95
Liquor	68.7	2.4
Grey Matter	52.87	0.93
White Matter	39	0.58
Blood	61.46	1.52
Edema	50.25	1.0
Liver	46.97	0.842
Liver Cancer	60	1.5
Internal Organs	52	0.91
Muscle	55	0.93

Table 14: Dielectric properties of healthy and unhealthy human tissues at $f = 870\text{MHz}$

here numerically investigated: liver cancer and brain edema. They are pathological conditions characterized by local modifications of tissues according to different dynamics. In both cases, however, abnormal cell proliferation and fluid accumulation produce a progressive dielectric contrast (tissues properties in Tab 14 [119]) over the healthy condition, which could be in principle detectable by an implanted RFID tag.

8.1.1 Liver Cancer Monitoring

The liver is a common site for both primary and secondary malignancies. These pathologies are characterized by angiogenesis and disruption of vascular architecture [113], producing in general abnormal tissues with higher dielectric properties, similar to blood. The dielectric contrast in the UHF band could be approximated at

about 30% for the permittivity and about 80% for the conductivity, as reported in [116].

An FDTD stratified model has been adopted for the human body. A $L = 3.5\text{cm}$ dipole coated by silicon is implanted into the liver (Fig. 112). It is important to notice that the radiating element's length is roughly one wavelength in the medium and hence it is close to the antiresonance wherein the sharp variation of resistance and reactance versus the effective permittivity makes the bandwidth narrower and thus the device more sensible. The same AA as in Chapter 2 Sec. 5.2 has been chosen.

Each tissue is characterized by specific dielectric properties (given in Table 14). Cancer has been modeled as a spherical volume of diameter D surrounding the antenna and the whole simulated dynamics is made to change from the absence of malignant tissue ($D = 0\text{mm}$) to the complete filling of the radiating structure ($D = L$) (Fig. 112). Position and size of the tumor have been derived by Computer Tomography (CT) data of typical pathologies. The body parameter to be sensed is hence the variation of the tumor diameter in successive measurements, e.g. $\Psi = D(t)$ with $0 \leq \Psi \leq L$.

Two kinds of microchips are considered with $Q_n = \{0.4, 20\}$. By enforcing the matching equation (2.16) with $\Psi_m = D(t_2) = 0.44L$, e.g. in the intermediate stage t_2 of the process, it is possible to emphasize the system resolution in the first part of the process and detect the tissue's variation typical of cancer. Fig. 113 shows the backscattered power calculated from (2.2) and the analog identifier from (2.7), which have been normalized to the initial condition $\Psi_0 = D(t_1)$ (early stage cancer), e.g. at the time of the implant. It is well evident that the sensed variation sensibly enlarges by using a microchip with high phase angle Q . For both microchips, the backscattered power is more sensitive to the tumor evolution than AID, thanks to the additional dependence of the former indicator on the tag's gain $G_T[\theta, \phi, \Psi]$ which sensibly reduces with the increase of the losses of the malignant tissue. However, both backscattered power and AID in case of higher- Q microchip are monotonic and steep around the reference condition t_1 enabling the unambiguous monitoring of the process (decrease or increase of the cancer volume) in its early stage, just after the implant.

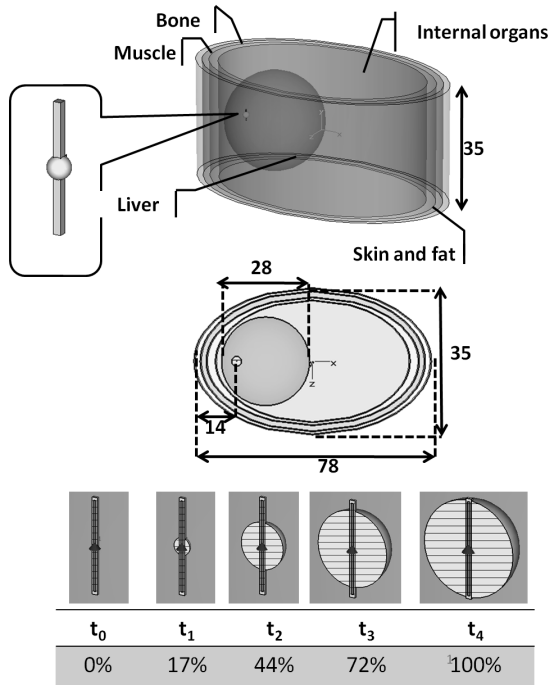


Figure 112: FDTD model of human liver cancer (size in [cm]). The implanted antenna is a λ -long dipole ($L = 3.5$ cm). The percentages indicate the diameter of the tumor with respect to the length of the dipole in some intermediate stages t_n of the process.

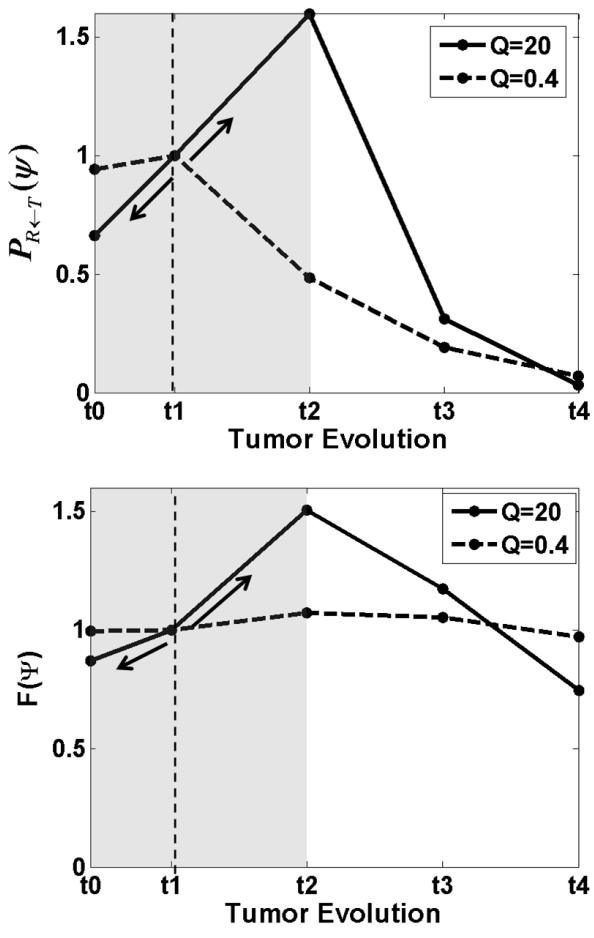


Figure 113: Liver Cancer. Simulated backscattered Power (top) and Analog Identifier (bottom) of the implanted dipole, referred to the corresponding values at t_1 (early stage cancer).

8.1.2 Brain Edema Monitoring

The edema arises from the flow of fluids into the extracellular space of the brain parenchyma after the surgical treatment of brain cancer. It is well known that the peritumoral tissues gradually absorb the liquid, consequently modifying their electromagnetic characteristics [120]. Due to the increase of the intracranial pressure, this pathology causes high grade symptoms: reduction in cerebral blood flow, nausea, vomiting, neurological disorders and, in its most severe form, the widespread ischemia. The differential diagnosis of the edema progression is actually possible only with CT scan or Nuclear Magnetic Resonance. Unfortunately, these imaging tools can not be used by many Countries, due to their high cost and low availability.

In the following numerical simulations, the head has been modeled as a multilayered lossy dielectric hemisphere, whose external and internal sizes reproduce with good approximation the real human districts (Fig.115). The tag is again modeled as a λ -long coated dipole ($L = 4\text{cm}$, in this case) and it is fully immersed in the center of the edema. The same AA as in Chapter 2 Sec. 5.2 has been chosen.

Particular attention has been devoted to the definition of edema dielectric properties since up to date only few works are available in the open scientific literature. A generic theoretical model [115] has been adopted elaborating the proposed empirical equations valid over a 0.01 – 17GHz frequency range:

$$\epsilon_r = 1.71f^{-1.13} + \frac{[\epsilon_S^m - 4]}{1 + (f/25)^2} + 4 \quad (8.1)$$

$$\sigma = 1.35f^{0.13}\sigma_{0.1} + \frac{[0.0222(\epsilon_S^m - 4)f^2]}{1 + (f/25)^2} \quad (8.2)$$

with f frequency of operation in GHz and ϵ_S^m and $\sigma_{0.1}$ empirical coefficients dependent on the tissue water content (Fig.114)..

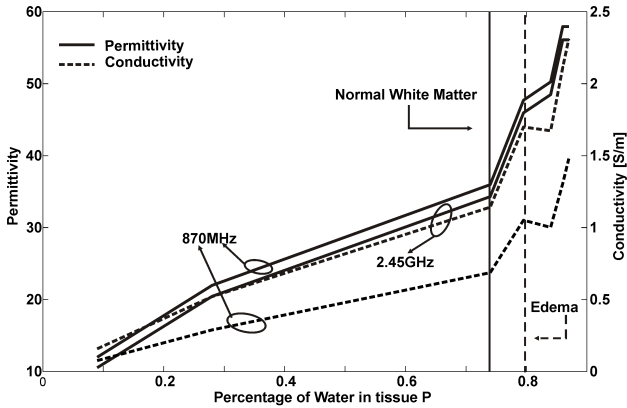


Figure 114: Dielectric properties of white matter varying its percentage of water.

The edema has been considered as normal white matter with an anomalous 80% water content (data in Tab.14). Position and size of the edema has been chosen following data produced by human computer tomographies (CT) of typical pathologies. The dielectric contrast in the UHF band, with respect to the surrounding environment, is approximately 25% for the permittivity and 60% for the conductivity.

The edema's parameter Ψ to be monitored is its diameter $0 < D < L(4\text{cm})$ as in the previous example.

Unlike liver cancer case, the matching equation (2.16) is here applied in an advanced edema condition $\Psi_m = D(t_3)$ such to achieve monotonic sensing curves within most of the process' evolution. Brain edema is in fact a rapid and massive event and thus it is important to be able to observe a wide range of possible values.

The backscattered power and the Analog Identifier variations with the edema evolution are visible in Fig.116, when referred to the initial state $D(t_0)$ (no edema), e.g at the time of the tag placement. Unlike the liver cancer, the not so high variation of conductivity produces lower variation of the backscattered signals:

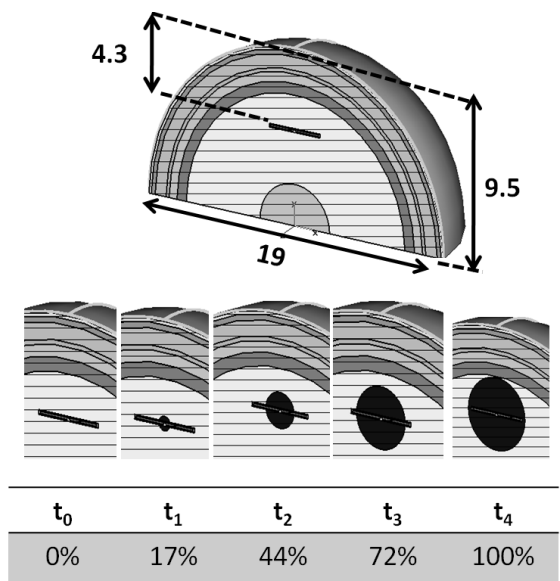


Figure 115: FDTD model of the brain edema evolution. The edema is modeled as a variable spherical volume. The tag is a $L = 4\text{cm}$ coated dipole.

$P_{R \leftarrow T}(\Psi)$ changes of about only 25% having imposed the same tissues evolution in term of volume and shape as before. However the inversion curves are monotonic for a wide range of values, approximately for the entire dynamics. Even in this case the choice of a high-Q microchip sensibly improves the dynamics of both inversion curves.

UWB Analysis

A first impulsive analysis is applied to understand the physical potentiality of an ultra wideband interrogation. The analysis of the implanted tag response is again performed by considering the tag in transmitting mode. The dipole's gap is sourced by a differentiated Gaussian pulse $x_G(t)$ of unitary peak value and maximum frequency of about 15GHz. The frequency dispersion of the different healthy and unhealthy cerebral tissues is properly included in FDTD simulations according to the model in [119].

The behavior of the tag during the edema evolution is analyzed through the concept of antenna impulse response which is independent on the particular interrogation waveform or interrogating antenna. At this purpose, denoting with $E_\xi(\underline{r}_0, t)$ the $\xi = \{x, y, z\}$ component of time-varying electric field radiated by the implanted antenna at point \underline{r}_0 outside the head, the antenna impulse response $h_\xi(t, \underline{r}_0)$ is calculated by deconvolving the excitation signal $x_G(t)$ out of $E_\xi(\underline{r}_0, t)$, e.g.

$$h_\xi(\underline{r}_0, t) = x(t) \otimes \underline{E}_\xi(\underline{r}_0, t) \quad (8.3)$$

The Gaussian deconvolution is numerically performed by the Moment Expansion method in [121]. It is worth noticing that the impulse response includes the effect of tag's shape but also the electromagnetic interaction with the living tissues which are rather lossy. This means that although the implanted dipole is not broadband itself, the presence of lossy tissues will make the transmitted wavepacket rather concentrated in time, simplifying the detection.

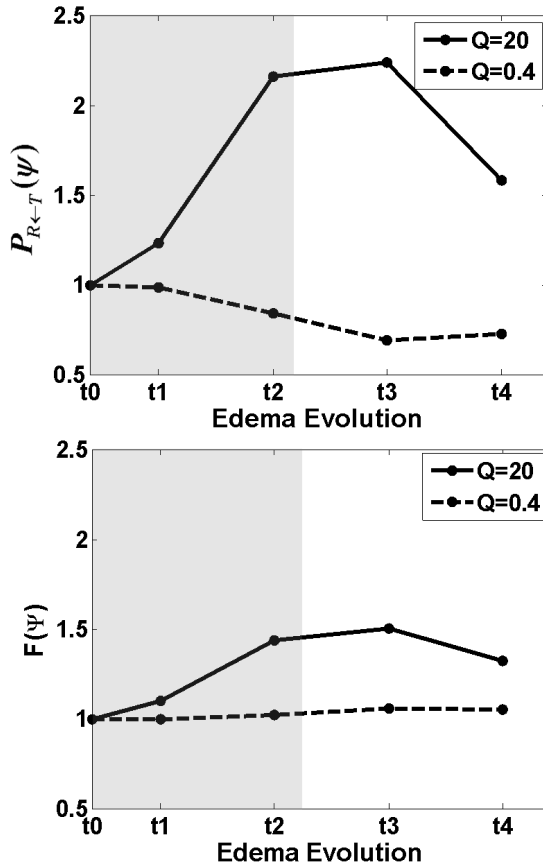


Figure 116: Brain edema. Simulated backscattered Power (top) and Analog Identifier (bottom) of the implanted dipole, referred to the initial state t_0 (no edema).

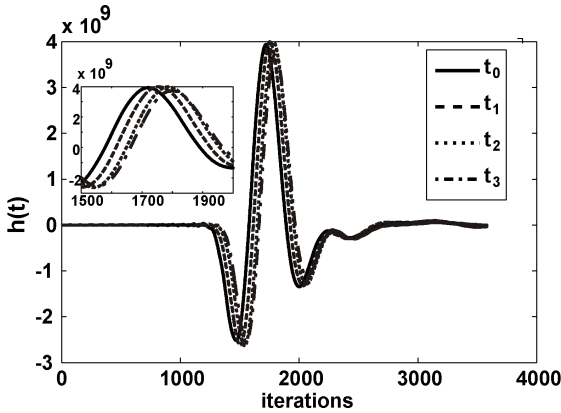


Figure 117: Effective height $h(t)$ of the implanted dipole

Fig.117 shows the x-component of the impulse response at 0.5cm from the head's surface, in correspondence to the y-axis (see Fig.115).

The edema evolution primarily produces a linear time shift of the signals with respect to the initial condition. The attenuation effects are instead not significant. The presence of the time shift can be related to the different propagation paths of the fields inside the head caused by the edema evolution. Due to an increased water content, the dielectric permittivity of the edema is sensibly different from the healthy tissue, as shown in Fig.118, with variation $\Delta\epsilon_r = \epsilon_{rEdema} - \epsilon_{rWhite} \sim 10$ which stays approximately constant in the entire band. The edema-filled region is hence electrically wider than the white matter one, therefore introducing an increasing delay in the field propagation.

It is possible to appreciate in Fig.119 that the time-delay of the signals' peak is rather monotone with the edema evolution, so promising the possibility of a remote detection capability.

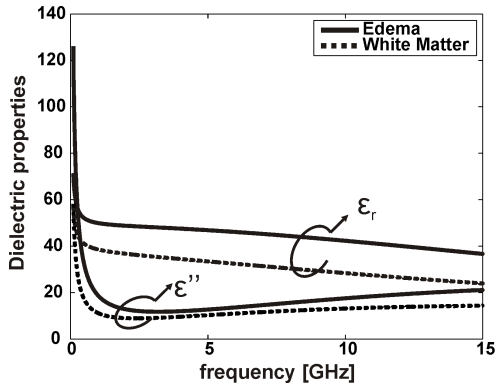


Figure 118: Dielectric property of normal and edematous white matter in the entire frequency range

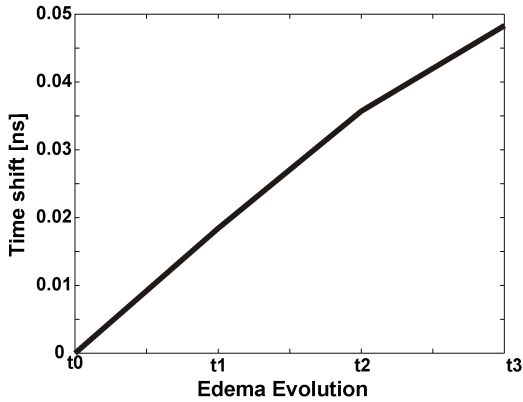


Figure 119: Time shift of the signal peaks referred to the initial condition t_0

Tissue	Complex Permittivity
Neck	$\bar{\epsilon}_1 = 41.4 - j14.8$
Muscle	$\bar{\epsilon}_2 = 55 - j19.2$
Physiologic Solution 0.157N	$\bar{\epsilon}_3 = 75.2 - j35.7$

Table 15: Liquid Phantom Properties at 870MHz

8.2 EXPERIMENTS WITH LIQUID BODY PHANTOM

The proposed idea of RFID sensing has been preliminarily experimented also by means of a first prototype of RFID tag implanted into a human equivalent phantom, a perspex cylinder (radius $r = 4\text{cm}$ and height $h = 20\text{cm}$) filled by a liquid mixture of water, sugar and salt [122] simulating a generic human district. A 0.8cm-diameter pipe, concentric to the container, simulates a possible body region in evolution (Fig.120) and it is filled, at different times, by liquids of increasing permittivity $\bar{\epsilon} = \epsilon_{\text{Re}} - j\epsilon_{\text{Im}}$ as reported in Tab.15. The parameter to be sensed is hence the variation of the permittivity of the filling liquid $\Psi = \bar{\epsilon}(t)$

The tag is a copper 3cm-long dipole (radius 0.5mm) connected to an NXP microchip of impedance $Z_{\text{chip}} = 15 - j135\Omega$ ($Q = 9$) and power sensitivity $P_{\text{chip}} = -15\text{dBm}$. The Antenna Adapter is simply an inductor L_m connected in series to the chip as in Fig.120. The reference process state is $\Psi_m = \bar{\epsilon}_3$, e.g. when the pipe is filled by a physiologic solution. The estimated antenna's input impedance is $Z_A(\epsilon_3) = 15 + j5\Omega$ and, accordingly, the required matching inductor from (2.16) is $L_m = 24\text{nH}$. The microchip and the inductor are insulated from the highly conductive liquids by a teflon tape (not shown in the figure).

All the measurements have been performed by means of a UHF Thing-Magic reader, connected to a 6-dB gain circular polarized patch antenna.

The variation of the backscattered power and Analog Identifier vs. the change of pipe's liquid are visible in Fig.121. The variation of liquid sensibly affects the radiation performance of the tag: the percentage variation (as in 2.8) is 50% for the backscattering indicator and 40% for the AID indicator. Although the tag is

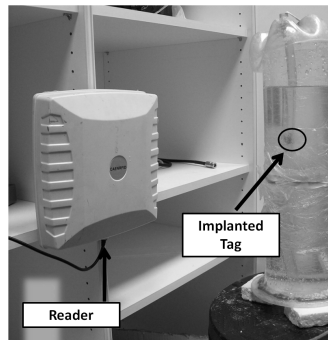
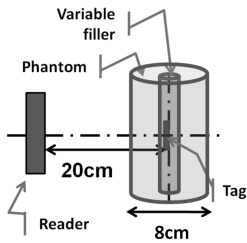
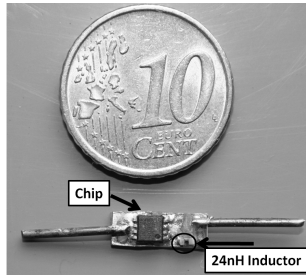


Figure 120: Prototype of implanted dipole and measurement setup.

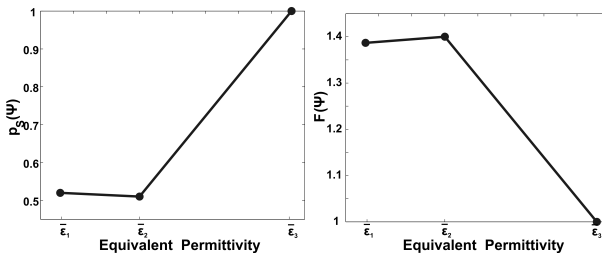


Figure 121: Laboratory phantom. Backscattered Power and Analog Identifier of the implanted dipole varying the liquid into the pipe, referred to the reference condition $\Psi_m = \epsilon_3$ (physiologic solution).

not matched to an extremely high-Q microchip, the system is nevertheless able to recognize even the small dielectric contrast between filler $\bar{\epsilon}_1$ and $\bar{\epsilon}_2$ ($\Delta\epsilon_{Re} = 24\%$ and $\Delta\epsilon_{Im} = 23\%$), as demonstrated in the left portion of the curves.

Fig.122 shows the measured variation of the turn-on power entering into the reader antenna with respect to the different liquids after fixing the reader-tag distance to $d = 20\text{cm}$. Changing the three filling liquids, the turn-on linearly ranges from 0.6W to 0.9W . It is worth mentioning that in the best matching condition and with the maximum interrogation power (3.2W EIRP) the implanted tag is readable up to 40cm from the phantom.

8.3 CONCLUSIONS

Numerical analysis and early experimentations seem to corroborate the possibility to sense some inner biological processes by means of implanted passive RFID tags. These phenomena in evolution produce specific and macroscopic effects on the electromagnetic response of the radio-sensor, which are detectable by the available low-cost technology and with limited power budgets (maximum radiated power less than 0.5W EIRP), enabling the use of hand-held devices.

Tag design may benefit from various degrees of freedom: the sensibility of the radio-sensor may indeed be enhanced by using

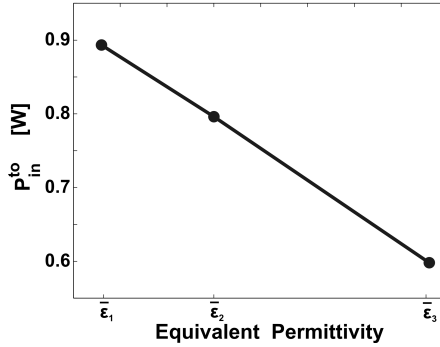


Figure 122: Laboratory Phantom. Turn on power (in EIRP) of the implanted dipole for different liquids filling the pipe.

high impedance microchips, while the inversion curves may be shaped by properly choosing the impedance matching condition. However further researches are needed to fully master the design of the *tag-as-a-sensor*, i.e. to achieve the full control of the antenna response over a time-varying process and to maximize the sensibility for the specific application. Many benefits are expected to come from multi-physics models and optimizers.

The RFID interrogation provides two independent measurements out of the turn-on power, the backscattered power and the analog identifiers. These could be used in a combined way to partly reduce the measurements uncertainties and achieve a more robust discrimination of phenomena. Moreover, in order to pursue a better control over the inversion curves, multi-chip tags could be considered where a plurality of antenna's ports are matched to their own microchip for different realizations $\{\Psi_1, \dots, \Psi_M\}$ of the process [17]. Narrowband sounding (involving standard RFID protocols) and UWB interrogations could be merged together by data fusion algorithms to improve the sensitivity or even to collect multi-dimensional informations about edema evolution.

Finally, although the sensing performances of the proposed platform could be worse than the ones provided by more complex active instruments, the possibility to use only passive devices

could offer great advantages in term of biocompatibility, cost and reliability. The application's simplicity, inside and even outside hospital environments, promises a pervasive diffusion and proves this technology as a valid support to the real-time medical diagnosis especially in Third World Countries, providing timely warning for more accurate screening.

CASE STUDY: THE STENTAG

This Chapter explores a realistic medical case concerning the modification of an endo-vascular device to achieve a STENTag able to sense the state of the vessel wherein it has been implanted. Theoretical and experimental analysis corroborate the feasibility of sensor-less RFID sensing for implantable human applications.

The idea of self-sensing implanted tag may found application in the monitoring of a biological ducts, subjected to a stent implant. A stent is a metal-mesh tubular device used to recover a *stenosis* [123], e.g. the occlusion of an artery due to abnormal accumulation of atherosclerotic plaque (Fig.123). The stent is surgically implanted into the vessel, then expands, keeps the vessel open thus improving blood flow, and stays in its seat permanently. Unfortunately, this procedure is not definitive (Fig.123) since a new accumulation of tissue inside and around the stent may give rise to risk of *in stent re-stenosis* (ISR). Such a phenomenon could begin just after the implant, due to hyper proliferation of neointimal cells (similar to muscular tissue) [117], as well as in a longer period due to the formation of new atherosclerotic plaque (similar to a mixture of water and fatty tissue) [118]. A common post-surgery requirement is the monitoring of the device status, or in other words the sensing of its local environment. This check, when possible, is actually performed using complex imaging techniques such as contrast angiography, computer tomography, magnetic resonance or IVUS, which are generally characterized by high costs for the hospital and long waiting queues for the patients.

A possible site of stenting and hence of ISR is the carotid. From a clinical and a prognostic point of view, the ISR can be usefully classified according to its evolution pattern and grade. As reported in [124], a more than 40% diameter reduction of the vessel can be considered critical for the safety of the patient, while a reduction of more than 80% must be regarded extremely dangerous and requires a further surgical treatment. The most severe forms of ISR occur when the lesions are wide ($> 10\text{mm}$ long) and extend beyond the margins of the stents. This latter form is referred to as *diffuse proliferative* ISR.

Since a vascular stent is typically fabricated with biocompatible metallic alloys, for instance the Nickel-Titanium (Nitinol) [125] with nice conducting features, some researchers have recently proposed to use the stent itself as a radiating element to set-up a transcatheter wireless telemetry system [126] where the status of the vessel is detected by a dedicated sensor integrated on board the stent. The idea to use the stent as sensor of restenosis has been instead investigated in [127], by relating the presence of cell proliferation and tissue growth to a low frequency (0.1Hz to 10MHz) impedance measurement. However, the wired nature of the device (being necessary catheters to measure the impedance of the stent), makes the described platform not suited to a wireless telemetry system.

The stent is instead a natural candidate to achieve a self-sensing implanted RFID tag which would combine both mechanical and sensing capabilities. This device, hereafter denoted as “STENTag”, has been obtained from an existing stent after minimal geometrical modification and by the inclusion of an RFID IC.

9.1 DESIGN PROCEDURES

The design guidelines in Chapter 2, are applied to a commercial $L=4.3\text{cm}$ long self-expanding stent [128]. The Antenna Adapter is here reduced to just an inductor connected in series to the chip,

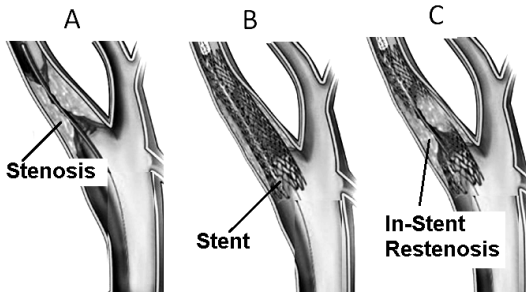


Figure 123: *Stenosis, stenting* procedures and *in-stent restenosis* of a biological duct. Adapted from [117]

and hence the transformed impedance of the STENTag will be simply

$$Z_T = Z_A + j\omega L_m \quad (9.1)$$

The considered IC is the NXP-G2X having power sensitivity $P_{\text{chip}} = -15\text{dBm}$ and impedance at 870MHz $Z_{\text{chip}} = 15 - j135\Omega$ (corresponding to impedance phase angle $Q = 9$). The IC is integrated into the device by means of an additional $l = 1\text{cm}$ long Nitinol straight wire, protruding from the tubular grid (Fig.126). The resulting object may be regarded as an asymmetrical dipole, with a hollow branch. Although a real implant of this augmented stent should require additional work, aimed to properly shape the added Nitinol wire and to preserve the biocompatibility, nevertheless this geometry is useful to demonstrate the design methodology and to understand the achievable sensitivity.

The process evolution R to be monitored is the proliferation of tissue inside the stent, according to typical diffuse proliferative patterns: as the ISR increases, the healthy tissue (normally blood) is progressively replaced by neointima (muscle cells proliferation), up to stimulate, in the very long period, the possible formation of new atherosclerotic plaque. Because of all those tissues are characterized by different dielectric properties, the parameter Ψ to be sensed is the equivalent complex permittivity $\bar{\epsilon}_{\text{stent}}$ inside

the stent. The desired STENTag should have an overall variation of the power response of not less than 3dB between the healthy condition and the full atherosclerotic restenosis, e.g.

$$\Delta p(R) \geq 3 \text{ dB} = 100\% \quad (9.2)$$

and a required turn-on power similar to the power emitted by hand-held smart-phones:

$$P_{in}^{\dagger}(\Psi) \leq 0.25W = 24 \text{ dBm} \quad \forall \Psi \in R \quad (9.3)$$

A simplified numerical model of the neck and of the in-stent restenosis has been set-up by the Finite Difference Time Domain (FDTD) method. The neck is simulated by cylinder of diameter $D=9\text{cm}$ and height $h=20\text{cm}$ filled by a homogeneous dielectric having the weighted average permittivity of all the main tissues composing the neck, ($\bar{\epsilon}_{neck} = 41.4 - j14.8$), while a smaller off-centered 1cm-diameter cylinder simulates the human carotid and it is filled by blood-like dielectric ($\bar{\epsilon}_{vessel}$). The STENTag is inserted in the middle of the smaller cylinder, tight fitting its internal surface, in a localized volume simulating the diffuse proliferative restenosis. Such a district, of height $S=8\text{cm}$, is homogeneously filled with a dielectric with variable permittivity ($\bar{\epsilon}_{stent}$). It is worth noticing that, although the proposed model sensibly simplifies the ISR patterns, it could be assumed as a reasonable approximation of the phenomena, since the radial increase/decrease of the diffuse proliferative IRS can be converted into the change of an homogeneous dielectric having the weighted average permittivity of all the healthy and the un-healthy portions of the vessel. As specified in Tab.16 seven conditions have been simulated, starting from the blood, passing through the neointimal proliferation, down to a plaque restenosis. Finally, the meshed tubular part of the STENTag has been simulated as a continuous cylindrical surface as in [126].

Table 16: Re-stenosis: Properties at 870MHz of the vessel's dielectric

Vessel's filler	Theoretical Complex Permittivity	Measured Complex Permittivity
1- Healthy vessel ISR = 0%	$\bar{\epsilon}_1 = 61.45 - j31.5$	$\bar{\epsilon}_{1m} = 57.8 - j33.0$
2-Neointimal proliferation ISR = 50%	$\bar{\epsilon}_2 = 58.22 - j25.3$	$\bar{\epsilon}_{2m} = 56.17 - j27.6$
3-Neointimal proliferation ISR = 100%	$\bar{\epsilon}_3 = 55 - j19.2$	$\bar{\epsilon}_{3m} = 51.65 - j22.7$
4-Plaque proliferation <i>grade 1</i>	$\bar{\epsilon}_4 = 48.2 - j17.0$	$\bar{\epsilon}_{4m} = 46.7 - j20.19$
5-Plaque proliferation <i>grade 2</i>	$\bar{\epsilon}_5 = 41.4 - j14.8$	$\bar{\epsilon}_{5m} = 41.8 - j17.6$
6-Plaque proliferation <i>grade 3</i>	$\bar{\epsilon}_6 = 27.5 - j10.95$	$\bar{\epsilon}_{6m} = 27.5 - j10.95$
7-Plaque proliferation ISR = 100%	$\bar{\epsilon}_7 = 14.13 - j12.15$	$\bar{\epsilon}_{7m} = 14.13 - j12.15$

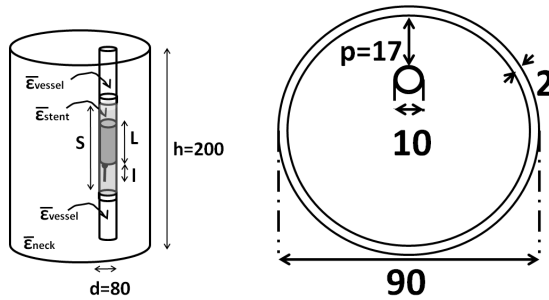


Figure 124: Cylindrical model of the neck, the carotid and the ISR (side view and top view). The STENTag is inserted in the middle of the smaller cylinder, tightly fitting its internal surface, as in a real-life implant. The ISR is modeled has a localized (shaded) volume with variable permittivity extending beyond the margins of the stents. Size in [mm]

Once fixed the antenna’s shape, the topology of the impedance adapter, the RFID IC, the design constraints and the models simulating the biological process under investigation, it is possible to iteratively apply the design procedure in Chapter 2 in order to search for the most suitable *matched state* Ψ_m and the corresponding value of the inductance L_m . In all the considered cases the electromagnetic model is solved by an FDTD tool which directly provide the antenna gain and impedance, while the derived power functions in (2.1) and (2.5) are then obtained in post-processing assuming a reader-tag distance of 20cm and a 5dB-gain reader’s antenna in linear polarization. Fig. 125 shows the backscattered power as in (2.2) normalized to the turn on power P_{in}^{to} , $p_S(\Psi) = P_{R \leftarrow T} / P_{in}^{to}$ and the turn-on power as in (2.5) versus the ISR process for three possible matched states $\Psi_m = \{\epsilon_1, \epsilon_6, 1\}$, calculated at the European UHF-RFID frequency 870MHz.

Among the considered choices of Ψ_m , the case $\Psi_m = \bar{\epsilon}_6$ offers the best trade-off between sensing sensibility (the slope of the curves) and the communication reliability which is expected to improve since the turn-on power decreases as the vessel’s state

worsens. The simulated dynamic range of the backscattered power between the healthy stent and the atherosclerotic restenosis is about 1 : 3, while the maximum required turn-on power is 25dBm, comparable with the power emitted by a mobile phone.

The resulting value of input impedance at 870MHz is $Z_A(\bar{\epsilon}_G) = 29 + j22\Omega$ and finally the matching inductor, as deduced from inversion of (2.16) through (9.1), is $L_m = 30\text{nH}$.

9.2 PROTOTYPES AND EXPERIMENTATION

A prototype of the STENTag is shown in Fig. 126. Since the Nitinol alloy can not be easily soldered, the wire components have been interconnected by means of crimped miniature connectors. Finally, the IC and the inductor have been insulated by a teflon tape (not shown in the figure) before the implant.

The STENTag has been experimented *in vitro* by means of equivalent liquid phantoms, according to the numerical model of Fig. 124. The larger and smaller cylinders have been fabricated by perspex pipes of thickness 2mm and 1mm, respectively, and then filled with liquid mixtures of water, sugar and salt which simulates the dielectric properties of the human tissues according to the recipes in [122]. The measured permittivity of the liquid phantoms, averaged over 6 samples, are indicated in Tab.16 and compared with the expected values from the recipes. The diffuse proliferative ISR has been rendered by dividing the small pipe into three parts. The central one, wherein the STENTag is placed, is dynamically filled/emptied by means of a proper hydraulic circuit (Fig. 127).

All the measurements have been performed within the UHF band (840-960 MHz) by means of a UHF Thing-Magic M5e reader, connected to a 5dB gain linear polarized patch antenna (Fig. 127) which is placed at 20cm from the neck phantom, as in the simulations. The reader permits to control the input power by 0.5dB steps and the receiving module performs a 8-bit digital conversion of the signals backscattered by the tag.

Fig. 128 shows the curves of the measured turn-on power in the UHF band, versus the change of permittivity of the liquid filling the STENTag. The curves have similar behavior but are clearly

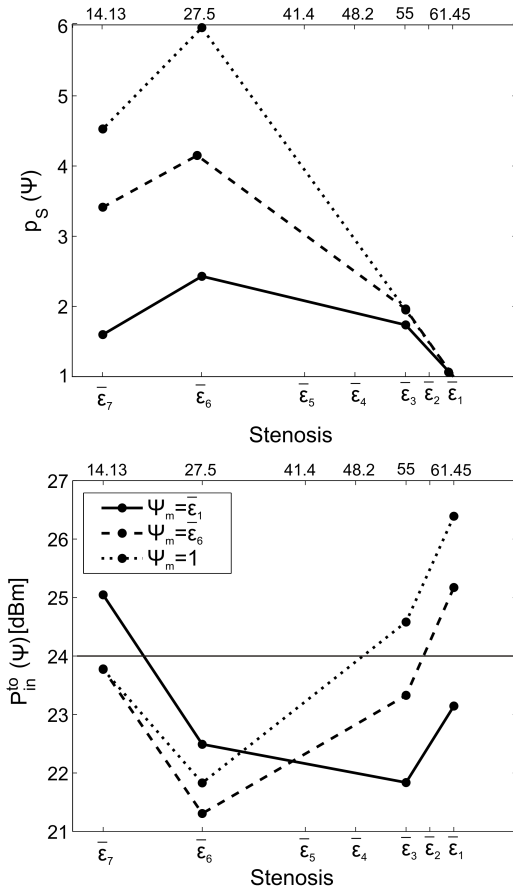


Figure 125: Normalized backscattered power and turn-on power of the STENTag simulated at 870MHz during the ISR process for three different choices of the matched state. The simulated data are sorted according to the real part of the considered complex permittivity.

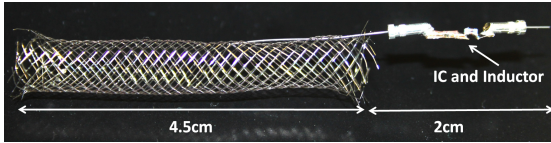


Figure 126: STENTag prototype with a details of the integration of RFID IC and of the inductor.

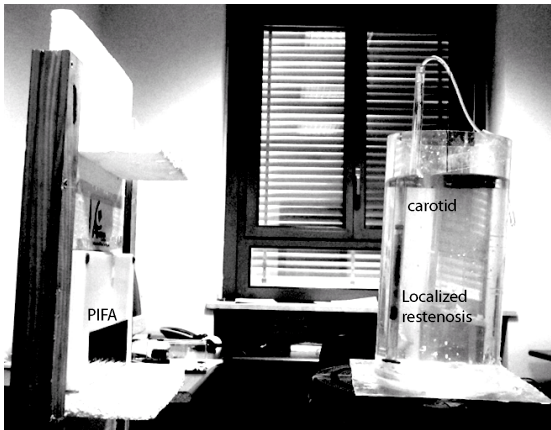


Figure 127: Experimental set-up comprising the liquid phantom resembling the neck where the STENTag has been implanted , and the interrogation 5dB patch antenna connected to the Thing-Magic M5e reader (not shown in the figure). The darker area in the central part of the phantom corresponds to the ISR. Such a volume is filled/emptied by means of a proper hydraulic circuit.

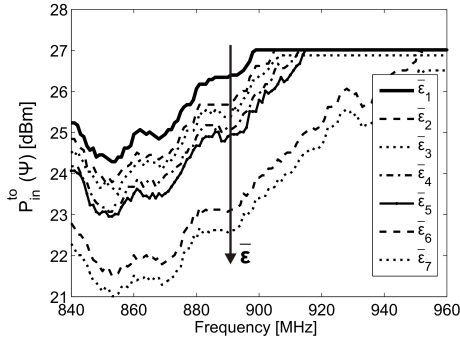


Figure 128: Measured turn-on power in the UHF (World- Wide) Band for the STENTag prototype, versus the change of the liquid permittivity filling the carotid-like pipe.

distinguishable. The power required to turn on the chip reduces as the stenosis's grade gets worse. A nearly 3dB dynamic range is observed at each frequency when moving from the healthy condition to complete plaque occlusion of the duct.

A more quantitative representation including the error analysis and the comparison with the computer simulations at 870MHz is given in Fig. 129 for both the backscattered power $p_S(\Psi)$ and the turn-on power $P_{in}^{to}(\Psi)$. The mean value and the standard deviation (the gray region) have been calculated starting from nine measurements at different angular offset (within $\pm 30^\circ$) between the reader's antenna and the tag.

First of all, it is apparent that in spite of the high tolerance in the fabrication of the tag and, non least, the typical instabilities of the receiving module of the RFID reader, simulations and measurements are in reasonable agreement, demonstrating the possibility to master the sensing and the communication response of the implanted radio sensor by means of the proposed design methodology.

The sensitivity to the tag's status is remarkable even in the early modification of the liquid, corresponding to an IRS = 50% (from $\bar{\epsilon}_1$ to $\bar{\epsilon}_2$) with a monotonic behavior in the entire considered per-

mittivity range. The turn-on measurement is almost invariant with the observation angle with less than 0.5dB uncertainty mainly due to the poor resolution of the reader. An even sharper sensitivity to the vessel's change is finally found by the backscattering analysis, with approximately 5dB span between the healthy carotid ($\bar{\epsilon}_1$) and the full occlusion by plaque ($\bar{\epsilon}_7$). The measurement variability of the backscattered power is instead not negligible, especially for extremely low values of $\bar{\epsilon}_{stent}$.

In order to analyze the sensibility of the proposed approach to the variability of the body district, the STENTag has been experimentally characterized also by considering a bigger neck phantom, resembling a stout subject. Such a phantom, referred to as *thick phantom*, is similar to the one in Fig. 124, except for the different diameter of the large cylinder ($D=13\text{cm}$) and for the position of the carotid-like pipe with respect to the border ($p=3\text{cm}$). The results (Fig. 129) are similar to those of the previous case except for a 3dB scaling since the increased size of the phantom and the deeper position of the radio-sensor produce a rise of the losses and consequently of the power required to establish the communication.

The uncertainty in the measured data may be however reduced by using all the frequency domain data in Fig. 128 and the *normalized scale factor* in 2.10. Fig. 130 shows the averaged γ_{ps} and $\gamma_{p_{in}^{to}}$ for the two phantoms. For clarity only the standard deviation of the thin case is presented. Since γ is a relative parameter, the profiles of the two phantoms are almost overlapped, demonstrating the repeatability of the sensing measurement regardless the human variability. Moreover the use of an averaging indicator sensibly reduces the uncertainty of the data, when compared to Fig. 129. In the worst case the uncertainty is only the 3% of the mean value, while in the early grade of the restenosis (ISR <50%) it drops to less than 1.5%.

Finally, by a linear fitting of the curves in Fig. 129 and 130, it is possible to estimate the percentage variation of all the previous power indicators referred to the healthy state $\bar{\epsilon}_0$ (Tab.II). In particular, a remarkable 33% of variation of the STENTag response may be achieved in the early restenosis ($\bar{\epsilon}_1 \rightarrow \bar{\epsilon}_2$) by monitoring the changes of the normalized scale factor of the backscattered power

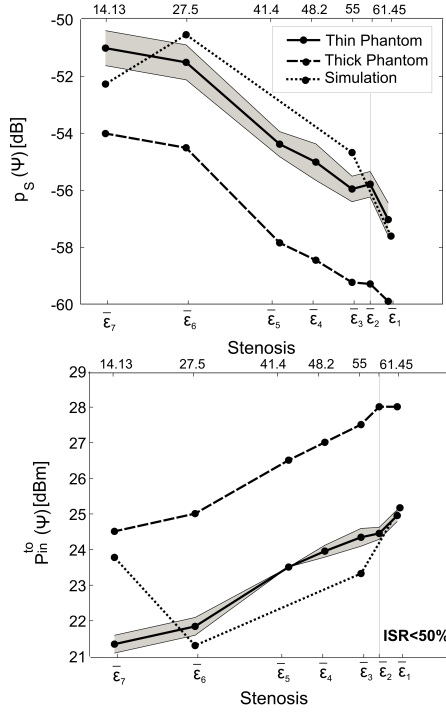


Figure 129: Measured (mean and shaded uncertainty region) and simulated a) backscattered power and b) turn on power for the STENTag prototype at 870MHz, on varying the liquid composition inside the carotid-like phantom. The measured data are sorted according to the real part of the considered complex permittivity.

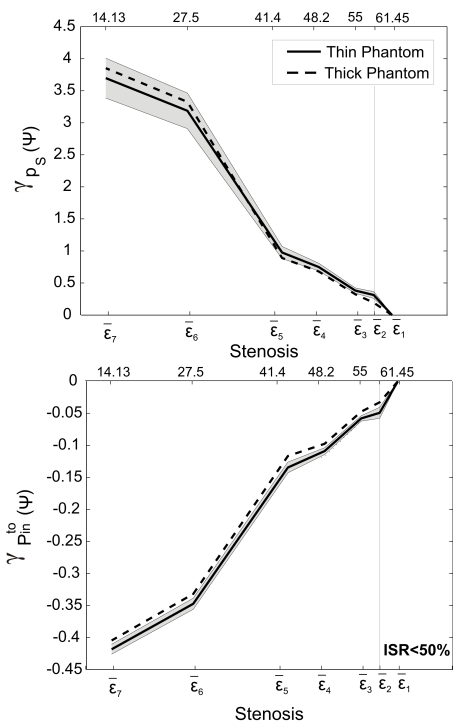


Figure 130: Normalized scale factor γ of a) backscattered power and b) turn on power for the two phantoms, on varying the liquid composition inside the carotid-like pipe. The measured data are sorted according to the real part of the considered complex permittivity.

Table 17: Measured relative changes in the STENTag responses

	$\Delta P_{t_0}^{in}(\%)$	$\Delta P_{R \leftarrow T}(\%)$	$\Delta \gamma_{P_{t_0}^{in}}(\%)$	$\Delta \gamma_{P_S}(\%)$
$\bar{\epsilon}_1 \rightarrow \bar{\epsilon}_2$	11%	33%	6%	38%
$\bar{\epsilon}_1 \rightarrow \bar{\epsilon}_7$	56%	400%	42%	370%

and more than 3 times changes at the atherosclerotic restenosis ($\bar{\epsilon}_1 \rightarrow \bar{\epsilon}_7$).

9.3 CONCLUSIONS

Theoretical and experimental investigations demonstrate the possibility to transform a vascular STENT into a radio-sensor with minimal structural modifications. The STENTag design can be effectively optimized to shape its sensitivity and dynamic range and in particular the achieved sensing capabilities look enough to fully discriminate the early grade of restenosis ($\bar{\epsilon}_1 \rightarrow \bar{\epsilon}_2$ $ISR \simeq 50\%$) by about a 40% variation in the measured data.

The RFID interrogation provides two independent measurements: turn-on power and the the backscattered power which, if observed over the frequency, may provide really robust and monotonic metrics, rather immune to the specificity of patients and to the measurement modality.

The described design technique may be however straightforwardly extended to many other implanted metal devices, such as prosthesis, sutures, graft or orthopedic fixings, for which long-term monitoring may provide an added value and turn the patient itself into a primary hub in the emerging personal Healthcare Systems.

10

CONCLUSIONS AND FUTURE PERSPECTIVES

The investigations and the results presented in this Thesis demonstrated that it is feasible to envisage *Pervasive Healthcare Systems* entirely based on passive RFID technology.

The first important result concerns the communication issue. Since the proposed platform is completely passive, the possibility to achieve a robust communication link in agreement with the actual power regulations was doubtful, especially for implanted devices. Thanks to innovative wearable antenna layouts, well decoupled from the body, the subjects can be monitored regardless their activity by means of fixed and portable readers: in the first case it is possible to cover distances comparable with domestic ambients, hospital rooms and offices, in the second case the read ranges are similar to the ones offered by traditional active body area networks. The most interesting outcomes regard however the implanted tags. Preliminary experiments demonstrated that a simple half-wave dipole implanted at 4 cm depth could be read up to 40 cm of distance, while by considering the power emitted by conventional smart-phone it should be possible to reach up to 10 – 20 cm.

In both cases, the proposed wearable and implantable antennas seem to respect the constraints related to the weight, the sizes and the invasiveness: the former can be easily integrated into clothes and plasters, for the latter it is instead possible to borrow from the military and aerospace world the concept of *structural antennas*, such to transform typical implanted devices provided with conductive elements (prosthesis, sutures, surgical implants,

orthopedic fixing and vascular stents) into RFID tags without additional radiating element and strong structural modifications.

The integration of several passive sensors and the possibility to use the tag itself as a sensitive device allowed the observation of many key parameters necessary to the effective remote monitoring of people and environment in usual and unusual scenarios: the subject can be observed *from inside* and *from outside* and can act also as an *environmental probe* of its surroundings. By properly combining the proposed sensors it should be possible to monitor a firemen during his activity or a elder within his house, to diagnose some neuromuscular diseases and follow the patient during his rehabilitation, to continuously verify the openness of a vessel and the functioning of an implanted stent. The designed working prototypes corroborate the idea that, even if passive approaches could sometimes suffer from weak sensitivity and poor selectivity, they can however offer great advantages in term of biocompatibility, cost, reliability and scalability and they result extremely useful when traditional and powered solutions can not be feasible, e.g. when the monitoring period is particularly long and complex.

The design of such a class of radio sensors demands for new paradigm and guidelines, deep focused on the physics of both radiation and sensing. Although they often have opposite requirements, it is possible to dynamically optimize their cohabitation according to the specific process to be monitored.

The promising results disclosed several unsolved questions and future research perspectives. The most challenging aspect remains the effective possibility to implant radio-sensor within the human body. More accurate analysis and test are required to validate the biocompatibility of the devices and their clinical performances.

From the system perspective, it is necessary to improve the robustness and the accuracy of the readers, such to transform them in real measurement devices and to face all the issues concerning the security and the privacy of the communication.

True applications are however not so distant: to completely fulfill the vision of passive pervasive healthcare, the Electromagnetism must be opened to broader and long-term perspectives and become the convergence of a number of heterogeneous medical

and engineering disciplines and expertise.

Regarding the future, however, it is paradoxically necessary to answer the question related to the effective usefulness of completely passive RFID radio-sensors themselves. From the implantable perspective, it is straightforwardly to deduce that the possibility to avoid batteries and dedicated electronics improves the biocompatibility of the radio-sensors and overcomes the drawbacks related to their low sensitivity. From the wearable point of view, instead, the benefits are not completely obvious. Due to the advances in low-power electronics, it is now feasible to have sophisticated RFID-like devices integrating sensing and signal processing, whose functionalities are enabled by small batteries integrated on board or even by the RF power transmitted by the reader. The last generation of RFID IC integrates for example active temperature sensors able to encode their data within the ID backscattered by the tag to the reader. Similarly, other IC integrate low-power DSP and can be easily interfaced with different active sensors: in all the cases, the idea is that the communication must be passive, while the sensing activity could be supported by means of external power.

Is it thus still useful to concentrate the future research efforts on completely passive systems? The answer is not univocal. All the environmental sensors designed to be integrated into daily objects or to be pervasively embedded into infrastructures must be passive such to guarantee their “transparent” action for long period, without the need of maintenance and at wide distance (it is worth noticing that if the sensors are externally powered, their read distance is sensibly reduced). Furthermore, passive sensors are necessary every time the correspondent active devices are extremely more expensive and technologically pointlessly more intricate, e.g. chemical and strain sensors. Finally, regarding the pure medical applications, it is possible to affirm that completely passive radio-sensors are useful to allow the widespread diffusion of smart disposable devices, e.g. plasters enhanced with sensing and communication functionalities, extremely advantageous to further bring the *assisted healthcare* concept into the daily life.

BIBLIOGRAPHY

- [1] U. Varshney, "Pervasive healthcare and wireless health monitoring," *Mobile Networks and Applications*, vol. 12, pp. 113–127, 2007. (Cited on page 1.)
- [2] T. Yilmaz, R. Foster, and Y. Hao, "Detecting vital signs with wearable wireless sensors," *Sensors*, vol. 10, no. 12, pp. 10837–10862, 2010. [Online]. Available: <http://www.mdpi.com/1424-8220/10/12/10837/> (Cited on pages 2 and 3.)
- [3] J. Bardram, "Pervasive healthcare as a scientific discipline," *Methods of information in medicine*, vol. 47, no. 3, pp. 178–185, 2008. (Cited on page 2.)
- [4] Y. Meng and H.-C. Kim, "Wearable systems and applications for healthcare," in *Computers, Networks, Systems and Industrial Engineering (CNSI), 2011 First ACIS/JNU International Conference on*, may 2011, pp. 325–330. (Cited on page 7.)
- [5] C. M. W. S. Ancoli Israel, R. Cole and C. P. Pollak, "The role of actigraphy in the study of sleep and circadian rhythms," *Sleep*, vol. 26, no. 3, pp. 342–392, May 2003. (Cited on pages 9 and 42.)
- [6] W. Yao, C.-H. Chu, and Z. Li, "The use of rfid in healthcare: Benefits and barriers," in *RFID-Technology and Applications (RFID-TA), 2010 IEEE International Conference on*, june 2010, pp. 128–134. (Cited on page 9.)
- [7] Z. Pang, Q. Chen, and L. Zheng, "A pervasive and preventive healthcare solution for medication noncompliance and daily monitoring," in *Applied Sciences in Biomedical and Communication Technologies, 2009. ISABEL 2009. 2nd International Symposium on*, nov. 2009, pp. 1–6. (Cited on page 9.)

- [8] M. Philipose, K. Fishkin, M. Perkowitz, D. Patterson, D. Fox, H. Kautz, and D. Hahnel, "Inferring activities from interactions with objects," *Pervasive Computing, IEEE*, vol. 3, no. 4, pp. 50 – 57, oct.-dec. 2004. (Cited on pages 9 and 14.)
- [9] M. Chen, S. Gonzalez, V. Leung, Q. Zhang, and M. Li, "A 2g-rfid-based e-healthcare system," *Wireless Communications, IEEE*, vol. 17, no. 1, pp. 37 –43, february 2010. (Cited on page 9.)
- [10] K. Finkenzerler, *RFID Handbook: Fundamentals and Applications in Contactless Smart Cards and Identification*, 2nd ed. New York, NY, USA: John Wiley and Sons, Inc., 2003. (Cited on page 14.)
- [11] G. Y. B. Lo, "Key technocal challenges and current implementations of body sensor network," in *International Workshop on Wearable and Implantable Body Sensor Networks*, Imperial College, London, April 2005. (Cited on page 14.)
- [12] P. Nikitin and K. Rao, "Theory and measurement of backscattering from rfid tags," *Antennas and Propagation Magazine, IEEE*, vol. 48, no. 6, pp. 212 –218, dec. 2006. (Cited on pages 14, 15, and 107.)
- [13] G. Marrocco, "Pervasive electromagnetics: sensing paradigms by passive rfid technology," *Wireless Communications, IEEE*, vol. 17, no. 6, pp. 10 –17, december 2010. (Cited on pages 14 and 23.)
- [14] F. Fuschini, C. Piersanti, F. Paolazzi, and G. Falciasecca, "Analytical approach to the backscattering from uhf rfid transponder," *Antennas and Wireless Propagation Letters, IEEE*, vol. 7, pp. 33 –35, 2008. (Cited on pages 15 and 107.)
- [15] G. Marrocco, "Rfid grids: Part i:electromagnetic theory," *Antennas and Propagation, IEEE Transactions on*, vol. 59, no. 3, pp. 1019 –1026, march 2011. (Cited on pages 16, 107, 118, 126, and 167.)

- [16] S. Caizzone and G. Marrocco, "Rfid grids: Part ii: Experimentations," *Antennas and Propagation, IEEE Transactions on*, vol. 59, no. 8, pp. 2896–2904, aug. 2011. (Cited on page 16.)
- [17] G. Marrocco, L. Mattioni, and C. Calabrese, "Multiport sensor rfids for wireless passive sensing of objects: Basic theory and early results," *Antennas and Propagation, IEEE Transactions on*, vol. 56, no. 8, pp. 2691–2702, aug. 2008. (Cited on pages 20, 31, 125, 136, and 196.)
- [18] G. Marrocco, "The art of uhf rfid antenna design: impedance-matching and size-reduction techniques," *Antennas and Propagation Magazine, IEEE*, vol. 50, no. 1, pp. 66–79, feb. 2008. (Cited on pages 22, 28, 110, 161, 162, 163, and 164.)
- [19] K. Rao, P. Nikitin, and S. Lam, "Impedance matching concepts in rfid transponder design," in *Automatic Identification Advanced Technologies, 2005. Fourth IEEE Workshop on*, oct. 2005, pp. 39–42. (Cited on page 23.)
- [20] J. Bolomey, S. Capdevila, L. Jofre, and J. Romeu, "Electromagnetic modeling of rfid-modulated scattering mechanism. application to tag performance evaluation," *Proceedings of the IEEE*, vol. 98, no. 9, pp. 1555–1569, sept. 2010. (Cited on page 25.)
- [21] L. Yang, R. Zhang, D. Staiculescu, C. Wong, and M. Tentzeris, "A novel conformal rfid-enabled module utilizing inkjet-printed antennas and carbon nanotubes for gas-detection applications," *Antennas and Wireless Propagation Letters, IEEE*, vol. 8, pp. 653–656, 2009. (Cited on pages 26, 138, 155, 159, and 160.)
- [22] G. Marrocco and F. Amato, "Self-sensing passive rfid: From theory to tag design and experimentation," in *Microwave Conference, 2009. EuMC 2009. European*, 29 2009-oct. 1 2009, pp. 001–004. (Cited on pages 30, 71, 101, 107, 129, and 142.)
- [23] G. Marrocco, "Rfid antennas for the uhf remote monitoring of human subjects," *Antennas and Propagation, IEEE Transac-*

- tions on, vol. 55, no. 6, pp. 1862–1870, June 2007. (Cited on pages 35, 58, and 59.)
- [24] M. J. Thorpy, "Classification of sleep disorders," *J Clin Neurophysiol*, vol. 7, no. 1, pp. 67–81, Jan 1990. (Cited on page 41.)
- [25] W. Hening, "The clinical neurophysiology of the restless legs syndrome and periodic limb movements. part i: diagnosis, assessment, and characterization," *Clinical Neurophysiology*, vol. 115, no. 9, pp. 1965–1974, 2004. (Cited on pages 42 and 93.)
- [26] M. Philipose, J. Smith, B. Jiang, A. Mamishev, S. Roy, and K. Sundara-Rajan, "Battery-free wireless identification and sensing," *Pervasive Computing, IEEE*, vol. 4, no. 1, pp. 37–45, Jan.-March 2005. (Cited on pages 43, 96, 121, and 127.)
- [27] A. Sample, D. Yeager, P. Powledge, and J. Smith, "Design of a passively-powered, programmable sensing platform for uhf rfid systems," in *RFID, 2007. IEEE International Conference on*, March 2007, pp. 149–156. (Cited on page 43.)
- [28] M. Zucconi, R. Ferri, R. Allen, P. C. Baier, O. Bruni, S. Chokroverty, L. Ferini-Strambi, S. Fulda, D. Garcia-Borreguero, W. A. Hening, and et al., "The official world association of sleep medicine (WASM) standards for recording and scoring periodic leg movements in sleep (PLMS) and wakefulness (PLMW) developed in collaboration with a task force from the international restless legs syndrome study group," *Sleep Medicine*, vol. 7, no. 2, pp. 175–83, 2006. [Online]. Available: <http://www.ncbi.nlm.nih.gov/pubmed/16459136> (Cited on page 44.)
- [29] (1999) European Council Recommendation 1999/519/EC of 12 July 1999 on the limitation of exposure of the general public to electromagnetic fields (0 Hz to 300 GHz). [Online]. Available: http://ec.europa.eu/enterprise/electr_equipment/lv/rec519.pdf (Cited on page 46.)

- [30] *Inertia Switch : Miniature series acceleration switches.* (2007). [Online]., Available: <http://www.inertiaswitch.com>. (Cited on page 47.)
- [31] M. M.Y.Agargun and L.Hanoglu, "Sleeping position, dream emotions, and subjective sleep quality," *Sleep Hypnosis*, vol. 6, no. 1, pp. 8–13, 2004. (Cited on pages 47 and 48.)
- [32] "Solidworks." [Online]. Available: <http://www.solidworks.it/> (Cited on page 50.)
- [33] *STMicroelectronics "LIS302DL, MEMS Motion Sensor Data Sheet"*, www.st.com. (Cited on page 53.)
- [34] P. S. Hall and Y. Hao, Eds., *Antennas And Propagation for Body-Centric Wireless Communications*, 1st ed. Norwood: Artech House Publishers, August 2006. (Cited on pages 57 and 74.)
- [35] L. Ukkonen, M. Schaffrath, D. Engels, L. Sydanheimo, and M. Kivikoski, "Operability of folded microstrip patch-type tag antenna in the uhf rfid bands within 865-928 mhz," *Antennas and Wireless Propagation Letters, IEEE*, vol. 5, no. 1, pp. 414–417, dec. 2006. (Cited on page 58.)
- [36] M. Hirvonen, K. Jaakkola, P. Pursula, and J. Saily, "Dual-band platform tolerant antennas for radio-frequency identification," *Antennas and Propagation, IEEE Transactions on*, vol. 54, no. 9, pp. 2632–2637, sept. 2006. (Cited on page 58.)
- [37] S.-L. Chen and K.-H. Lin, "A slim rfid tag antenna design for metallic object applications," *Antennas and Wireless Propagation Letters, IEEE*, vol. 7, pp. 729–732, 2008. (Cited on page 58.)
- [38] C. Calabrese and G. Marrocco, "Meandered-slot antennas for sensor-rfid tags," *Antennas and Wireless Propagation Letters, IEEE*, vol. 7, pp. 5–8, 2008. (Cited on page 58.)
- [39] S. M. Polivka M. and H. P, *UHF RFID of People*, 1st ed. Vienna: In Tech Education and Publishing, In Tech Education and Publishing, January 2009, ch. 4. (Cited on page 58.)

- [40] L. Yang, L. Martin, D. Staiculescu, C. Wong, and M. Tentzeris, "Conformal magnetic composite rfid for wearable rf and bio-monitoring applications," *Microwave Theory and Techniques, IEEE Transactions on*, vol. 56, no. 12, pp. 3223–3230, dec. 2008. (Cited on page 58.)
- [41] C. Balanis, *Antenna Theory: analysis and Design*, 2nd ed. New York: Wiley and Son, 1997. (Cited on pages 62, 63, 69, 109, and 111.)
- [42] I. A. R.Garg, P.Bhartia, *Microstrip antenna design handbook*. Boston: Artech House Publishers, 2001. (Cited on page 63.)
- [43] M. El Yazidi, M. Himdi, and J. Daniel, "Transmission line analysis of nonlinear slot coupled microstrip antenna," *Electronics Letters*, vol. 28, no. 15, pp. 1406–1408, july 1992. (Cited on page 63.)
- [44] J. P. Kim and W. S. Park, "Analysis and network modeling of an aperture-coupled microstrip patch antenna," *Antennas and Propagation, IEEE Transactions on*, vol. 49, no. 6, pp. 849–854, jun 2001. (Cited on page 64.)
- [45] F. G.Marrocco, "Best: a finite-difference solver fo time electromagnetics," *Simulation Practice Theory*, no. 7, pp. 279–293, 1999. (Cited on pages 64, 108, and 128.)
- [46] P. Salonen, Y. Rahmat-Samii, M. Schaffrath, and M. Kivikoski, "Effect of textile materials on wearable antenna performance: a case study of gps antennas," in *Antennas and Propagation Society International Symposium, 2004. IEEE*, vol. 1, june 2004, pp. 459 – 462 Vol.1. (Cited on page 74.)
- [47] P. Salonen and Y. Rahmat-Samii, "Textile antennas: effects of antenna bending on input matching and impedance bandwidth," *Aerospace and Electronic Systems Magazine, IEEE*, vol. 22, no. 3, pp. 10–14, march 2007. (Cited on page 74.)
- [48] S. Zhu and R. Langley, "Dual-band wearable textile antenna on an ebg substrate," *Antennas and Propagation, IEEE Trans-*

- actions on*, vol. 57, no. 4, pp. 926–935, april 2009. (Cited on page 74.)
- [49] G. Marrocco, E. Di Giampaolo, and R. Aliberti, “Estimation of uhf rfid reading regions in real environments,” *Antennas and Propagation Magazine, IEEE*, vol. 51, no. 6, pp. 44–57, dec. 2009. (Cited on pages 77, 78, 81, and 90.)
- [50] D. Psychoudakis, G.-Y. Lee, C.-C. Chen, and J. L. Volakis, “Military uhf body-worn antennas for armored vests,” in *Antennas and Propagation (EuCAP), 2010 Proceedings of the Fourth European Conference on*, april 2010, pp. 1–4. (Cited on page 77.)
- [51] L. Vallozzi, H. Rogier, and C. Hertleer, “A textile patch antenna with dual polarization for rescue workers’ garments,” in *Antennas and Propagation, 2009. EuCAP 2009. 3rd European Conference on*, march 2009, pp. 1018–1021. (Cited on page 77.)
- [52] C. Occhiuzzi and G. Marrocco, “The rfid technology for neurosciences: Feasibility of limbs’ monitoring in sleep diseases,” *Information Technology in Biomedicine, IEEE Transactions on*, vol. 14, no. 1, pp. 37–43, jan. 2010. (Cited on page 77.)
- [53] D. D.D.Arumugam, “Specific absorption rates in the human head and shoulder for passive uhf rfid systems at 915mhz,” in *XXIX General Assembly of the International Union of Radio Science URSI*, 2008. (Cited on page 77.)
- [54] A. Alomainy, Y. Hao, X. Hu, C. Parini, and P. Hall, “Uwb on-body radio propagation and system modelling for wireless body-centric networks,” *Communications, IEE Proceedings-*, vol. 153, no. 1, pp. 107–114, feb. 2006. (Cited on page 84.)
- [55] D. Arumugam, D. Engels, and M. Mickle, “Specific absorption rates in muscle tissues for passive uhf rfid tag backscatter,” in *Radio and Wireless Symposium, 2009. RWS ’09. IEEE*, jan. 2009, pp. 445–448. (Cited on page 89.)

- [56] "Printed passive uhf rfid tags as wearable strain sensors," in *Applied Sciences in Biomedical and Communication Technologies (ISABEL), 2010 3rd International Symposium on*, nov. 2010, pp. 1–5. (Cited on page 94.)
- [57] *Comus Group of Companies "MS24M Product Data Sheet"*, Available at www.comus-intl.com. (Cited on pages 95 and 96.)
- [58] *STMicroelectronics "LIS302DL, MEMS Motion Sensor Data Sheet"*, www.st.com. (Cited on page 98.)
- [59] C. Occhiuzzi and G. Marrocco, "Pervasive body sensing: Implanted rfid tags for vascular monitoring," in *Antennas and Propagation Society International Symposium (APSURSI), 2010 IEEE*, july 2010, pp. 1–4. (Cited on page 101.)
- [60] C. Occhiuzzi, A. Rida, G. Marrocco, and M. Tentzeris, "Rfid passive gas sensor integrating carbon nanotubes," *Microwave Theory and Techniques, IEEE Transactions on*, vol. PP, no. 99, p. 1, 2011. (Cited on pages 101 and 139.)
- [61] G. Marrocco, "Gain-optimized self-resonant meander line antennas for rfid applications," *Antennas and Wireless Propagation Letters, IEEE*, vol. 2, no. 1, pp. 302–305, 2003. (Cited on page 105.)
- [62] R.C.Hibbeler, *Engineering Mechanics: Combined Statics and Dynamics*, 12th ed. Prentice Hall, 2010. (Cited on pages 105, 108, and 113.)
- [63] S. Best, "On the resonant properties of the koch fractal and other wire monopole antennas," *Antennas and Wireless Propagation Letters, IEEE*, vol. 1, no. 1, pp. 74–76, 2002. (Cited on page 109.)
- [64] S. Merilampi, T. Bjorninen, L. Ukkonen, P. Ruuskanen, and L. Sydanheimo, "Embedded wireless strain sensors based on printed rfid tag," *Sensor Review*, vol. 31, no. 1, 2011. (Cited on page 117.)

- [65] H. Funakubo, *Shape Memory Alloys*. New York: Gordon and Breach Publishers, 1987. (Cited on pages 118 and 122.)
- [66] S. Caizzone, C. Occhiuzzi, and G. Marrocco, "Multi-chip rfid antenna integrating shape-memory alloys for detection of thermal thresholds," *Antennas and Propagation, IEEE Transactions on*, vol. PP, no. 99, p. 1, 2011. (Cited on page 118.)
- [67] M. O'Connor, "Coldchain project reveals temperature inconsistencies," *RFID Journal*, December 2006. (Cited on page 119.)
- [68] A. Dada and F. Thiesse, "Sensor applications in the supply chain : The example of quality-based issuing of perishables," *Internet of Things 2008 First International Conference for Academia and Industry*, pp. 140–154, 2008. (Cited on page 119.)
- [69] R. Kuchta and R. Vrba, "Wireless and wired temperature data system," *Systems, Second International Conference on*, vol. 0, p. 49, 2007. (Cited on page 119.)
- [70] S. Kim, J.-H. Cho, H.-S. Kim, H. Kim, H.-B. Kang, and S.-K. Hong, "An epc gen 2 compatible passive/semi-active uhf rfid transponder with embedded feram and temperature sensor," in *Solid-State Circuits Conference, 2007. ASSCC '07. IEEE Asian*, nov. 2007, pp. 135–138. (Cited on page 119.)
- [71] J. J.Gao and H.E.Nilsson, "Printed temperature sensors for passive rfid tags," in *Progress In Electromagnetics Research Symposium, Xi'an, China*, 2010. (Cited on page 120.)
- [72] R. Bhattacharyya, C. Floerkemeier, S. Sarma, and D. Deavours, "Rfid tag antenna based temperature sensing in the frequency domain," in *RFID (RFID), 2011 IEEE International Conference on*, april 2011, pp. 70–77. (Cited on page 120.)
- [73] H. Funakubo, *Shape Memory Alloys*. New York: Gordon and Breach Publishers, 1987, vol. 11. (Cited on page 122.)
- [74] AA.VV, "Niti Smart Sheet-properties", <http://web.archive.org/web/20030418012213/>

<http://www.sma-inc.com/NiTiProperties.html>. (Cited on page 122.)

- [75] E. Rosa, "The self and mutual inductances of linear conductors," *Bulletin of the Bureau of Standards*, vol. 46, no. 2, p. 301, 1908. (Cited on page 125.)
- [76] D. M. Dobkin, *The RF in RFID: passive UHF RFID in Practice*. Amsterdam: Elsevier, 2007. (Cited on page 125.)
- [77] R. Harrington and J. Mautz, "Modal analysis of loaded n-port scatterers," in *Antennas and Propagation Society International Symposium, 1972*, vol. 10, dec 1972, p. 267. (Cited on page 126.)
- [78] C. Desoer, "The maximum power transfer theorem for n-ports," *Circuit Theory, IEEE Transactions on*, vol. 20, no. 3, pp. 328 – 330, may 1973. (Cited on page 127.)
- [79] B. Yang and Q. Feng, "A folded dipole antenna for rfid tag," in *Microwave and Millimeter Wave Technology, 2008. ICMMT 2008. International Conference on*, vol. 3, april 2008, pp. 1047 –1049. (Cited on page 128.)
- [80] T. Kellomaki, T. Bjorninen, L. Ukkonen, and L. Sydanheimo, "Shirt collar tag for wearable uhf rfid systems," in *Antennas and Propagation (EuCAP), 2010 Proceedings of the Fourth European Conference on*, april 2010, pp. 1 –5. (Cited on page 132.)
- [81] H. Bai and G. Shi, "Gas sensors based on conducting polymers," *Sensors*, vol. 7, no. 3, pp. 267–307, 2007. [Online]. Available: <http://www.mdpi.com/1424-8220/7/3/267/> (Cited on page 136.)
- [82] Y. Sakai, Y. Sadaoka, and M. Matsuguchi, "Humidity sensors based on polymer thin films," *Sensors and Actuators B: Chemical*, vol. 35, no. 1-3, pp. 85 – 90, 1996. [Online]. Available: <http://www.sciencedirect.com/science/article/pii/S0925400596020199> (Cited on page 137.)

- [83] W. U. M. K. A. Elschner, S. Kirchmeyer, *PEDOT: Principles and Applications of an Intrinsically Conductive Polymer*. CRC Press, 2010. (Cited on page 137.)
- [84] T. Kinkeldei, C. Zysset, K. Cherenack, and G. Troster, "A textile integrated sensor system for monitoring humidity and temperature," in *Solid-State Sensors, Actuators and Microsystems Conference (TRANSDUCERS), 2011 16th International*, June 2011, pp. 1156–1159. (Cited on page 137.)
- [85] J. Reboun, A. Hamacek, T. Dzugan, and M. Kroupa, "Sensorial characteristics of conductive polymers," in *Electronics Technology, 2009. ISSE 2009. 32nd International Spring Seminar on*, May 2009, pp. 1–5. (Cited on page 137.)
- [86] A. Oprea, N. Baersan, U. Weimar, M.-L. Bauersfeld, D. Ebling, and J. WÄÄ¶llenstein, "Capacitive humidity sensors on flexible rfid labels," *Sensors and Actuators B: Chemical*, vol. 132, no. 2, pp. 404–410, 2008. [Online]. Available: <http://www.sciencedirect.com/science/article/pii/S0925400507008179> (Cited on page 137.)
- [87] K. Chang, Y. Kim, Y. Kim, and Y. Yoon, "Functional antenna integrated with relative humidity sensor using synthesised polyimide for passive rfid sensing," *Electronics Letters*, vol. 43, no. 5, pp. 7–8, 1 2007. (Cited on page 137.)
- [88] S. Johan, X. Zeng, T. Unander, A. Koptuyug, and H.-E. Nilsson, "Remote moisture sensing utilizing ordinary rfid tags," in *Sensors, 2007 IEEE*, Oct. 2007, pp. 308–311. (Cited on page 137.)
- [89] J. Virtanen, L. Ukkonen, T. Bjoandrninen, A. Z. Elsherbeni, and L. Sydaandnheimo, "Inkjet-printed humidity sensor for passive uhf rfid systems," *Instrumentation and Measurement, IEEE Transactions on*, vol. PP, no. 99, pp. 1–10, 2011. (Cited on page 137.)
- [90] M.I. Baraton, *Sensors for Environment, Health and Security*. Springer, 2009. (Cited on page 138.)

- [91] P. Avouris, J. Appenzeller, R. Martel, and S. Wind, "Carbon nanotube electronics," *Proceedings of the IEEE*, vol. 91, no. 11, pp. 1772 – 1784, nov 2003. (Cited on page 138.)
- [92] J. Y.Wang, "A review of carbon nanotubes-based gas sensors," *Journal of Sensors*, May 2009. (Cited on page 138.)
- [93] K. G. Ong, K. Zeng, and C. Grimes, "A wireless, passive carbon nanotube-based gas sensor," *Sensors Journal, IEEE*, vol. 2, no. 2, pp. 82 –88, apr 2002. (Cited on pages 138, 158, 159, and 169.)
- [94] S. Chopra, S. Natarajan, and A. Rao, "Gas sensing using carbon nanotube-based resonator," in *Sensors, 2004. Proceedings of IEEE*, oct. 2004, pp. 399 – 402 vol.1. (Cited on page 138.)
- [95] P. Russer, N. Fichtner, P. Lugli, W. Porod, J. Russer, and H. Yordanov, "Nanoelectronics-based integrate antennas," *Microwave Magazine, IEEE*, vol. 11, no. 7, pp. 58 –71, dec. 2010. (Cited on page 138.)
- [96] A. C. S. A.Mehdipour, I.D.Rosca, "Advanced carbon-fiber composite materials for rfid tag antenna applications," *Applied Computational Electromagnetics Society ACES Journal, Special Issue on Computational and Experimental Techniques for RFID Systems and Applications,,* vol. 25, no. 3, pp. 218–229, March 2010. (Cited on pages 138 and 155.)
- [97] Y. Zhou, Y. Bayram, F. Du, L. Dai, and J. Volakis, "Polymer-carbon nanotube sheets for conformal load bearing antennas," *Antennas and Propagation, IEEE Transactions on*, vol. 58, no. 7, pp. 2169 –2175, july 2010. (Cited on pages 138 and 155.)
- [98] M. J. J. Kamil, "Flexible temperature sensor integrated with rfid tag," in *XIII International PhD Workshop OWD*, October 2011. (Cited on pages 141 and 143.)
- [99] N. Kirsch, N. Vacirca, T. Kurzweg, A. Fontecchio, and K. Dandekar, "Performance of transparent conductive polymer antennas in a mimo ad-hoc network," in *Wireless and*

- Mobile Computing, Networking and Communications (WiMob), 2010 IEEE 6th International Conference on*, oct. 2010, pp. 9–14. (Cited on page 141.)
- [100] N. Kirsch, N. Vacirca, E. Plowman, T. Kurzweg, A. Fontecchio, and K. Dandekar, “Optically transparent conductive polymer rfid meandering dipole antenna,” in *RFID, 2009 IEEE International Conference on*, april 2009, pp. 278–282. (Cited on page 141.)
- [101] M. Meyyappan, Ed., *Carbon Nanotubes: Science and Applications*, 1st ed. CRC Press, July 2004. (Cited on page 155.)
- [102] A. Mehdipour, I. Rosca, A.-R. Sebak, C. Trueman, and S. Hoa, “Full-composite fractal antenna using carbon nanotubes for multiband wireless applications,” *Antennas and Wireless Propagation Letters, IEEE*, vol. 9, pp. 891–894, 2010. (Cited on page 155.)
- [103] S. Orfanidis, *Electromagnetic Waves and Antennas*. New Jersey: Rutgers University, August 2010. (Cited on page 159.)
- [104] Y. Lee, “Antenna circuit design for rfid applications,” Microchip Technology Inc, <http://ww1.microchip.com/downloads/en/AppNotes/00710c.pdf>, AP7 10, 2003. (Cited on pages 163 and 164.)
- [105] R.E.Collin, *Antennas and Radiowave Propagation*, ser. Electrical and Computer Engineering. Mcgraw Hill, February 1985. (Cited on page 163.)
- [106] A. Sani, M. Rajab, R. Foster, and Y. Hao, “Antennas and propagation of implanted rfids for pervasive healthcare applications,” *Proceedings of the IEEE*, vol. 98, no. 9, pp. 1648–1655, sept. 2010. (Cited on page 179.)
- [107] A. Alomainy and Y. Hao, “Modeling and characterization of biotelemetric radio channel from ingested implants considering organ contents,” *Antennas and Propagation, IEEE Transactions on*, vol. 57, no. 4, pp. 999–1005, april 2009. (Cited on page 179.)

- [108] F. Merli, B. Fuchs, J. Mosig, and A. Skrivervik, "The effect of insulating layers on the performance of implanted antennas," *Antennas and Propagation, IEEE Transactions on*, vol. 59, no. 1, pp. 21–31, jan. 2011. (Cited on page 179.)
- [109] W. Xia, K. Saito, M. Takahashi, and K. Ito, "Performances of an implanted cavity slot antenna embedded in the human arm," *Antennas and Propagation, IEEE Transactions on*, vol. 57, no. 4, pp. 894–899, april 2009. (Cited on page 179.)
- [110] *Verychip*, <http://www.positiveidcorp.com/>. (Cited on page 179.)
- [111] D. Valderas, C. Schmidt, and X. Chen, "Broadband implanted uhf rfid antenna," in *Antennas and Propagation Society International Symposium (APSURSI), 2010 IEEE*, july 2010, pp. 1–4. (Cited on page 180.)
- [112] H. Rajagopalan and Y. Rahmat-Samii, "Ingestible rfid biocapsule tag design for medical monitoring," in *Antennas and Propagation Society International Symposium (APSURSI), 2010 IEEE*, july 2010, pp. 1–4. (Cited on page 180.)
- [113] J. I. M. M. Fernandez, D. Semela and J. Bosch, "Angiogenesis in liver disease." *Journal of Hepatology*, vol. 50, no. 3, pp. 604–20, 2009. (Cited on pages 180 and 182.)
- [114] B.-B. U. E. M. E. K. M. Bitzer, T. Nagele, "Role of hydrodynamic processes in the pathogenesis of peritumoral brain edema in meningiomas." *J Neurosurg*, vol. 4, no. 93, pp. 594–604, October 2000. (Cited on pages 180 and 181.)
- [115] J. L. Schepps and K. R. Foster, "The uhf and microwave dielectric properties of normal and tumour tissues: variation in dielectric properties with tissue water content," *Physics in Medicine and Biology*, vol. 25, no. 6, p. 1149, 1980. [Online]. Available: <http://stacks.iop.org/0031-9155/25/i=6/a=012> (Cited on pages 181 and 186.)
- [116] A. P. O'Rourke, M. Lazebnik, J. M. Bertram, M. C. Converse, S. C. Hagness, J. G. Webster, and D. MMahvi, "Dielectric

- properties of human normal, malignant and cirrhotic liver tissue: in vivo and ex vivo measurements from 0.5 to 20 ghz using a precision open-ended coaxial probe," *Physics in Medicine and Biology*, vol. 52, no. 15, p. 4707, 2007. [Online]. Available: <http://stacks.iop.org/0031-9155/52/i=15/a=022> (Cited on pages 181 and 183.)
- [117] R. Hoffmann, G. S. Mintz, G. R. Dussaillant, J. J. Popma, A. D. Pichard, L. F. Satler, K. M. Kent, J. Griffin, and M. B. Leon, "Patterns and mechanisms of in-stent restenosis: A serial intravascular ultrasound study," *Circulation*, vol. 94, no. 6, pp. 1247–1254, 1996. (Cited on pages 181, 199, and 201.)
- [118] M. H. M. T. K. N. Y. K. E. T. Y. A. O. K. T. Suzuki, "The morphological findings of very late in-stent restenosis after bare-metal stent implant: Optical coherence tomography analysis," *Circulation*, vol. A11302, no. 122, 2010. (Cited on pages 181 and 199.)
- [119] <http://www.brooks.af.mil/AFRL/HED/hedr/reports/dielectric/home.html>, C.Gabriel, S.Gabriel, *Compilation of the Dielectric Properties of Body Tissues at RF and Microwave Frequencies*, <http://www.brooks.af.mil/AFRL/HED/hedr/reports/dielectric/home.html>. (Cited on pages 182 and 189.)
- [120] H. Kao, R. Cardoso, and E. Shwedyk, "Correlation of permittivity and water content during cerebral edema," *Biomedical Engineering, IEEE Transactions on*, vol. 46, no. 9, pp. 1121–1128, sept. 1999. (Cited on page 186.)
- [121] M. Ciattaglia and G. Marrocco, "Time domain synthesis of pulsed arrays," *Antennas and Propagation, IEEE Transactions on*, vol. 56, no. 7, pp. 1928–1938, july 2008. (Cited on page 189.)
- [122] G. Hartsgrrove, A. Kraszewski, and A. Surowiec, "Simulated biological materials for electromagnetic radiation absorption studies." *Bioelectromagnetics*, vol. 8, no. 1, pp. 29–36, 1987. [Online]. Available: <http://www.ncbi.nlm.nih.gov/pubmed/3579997> (Cited on pages 193 and 205.)

- [123] B. R. P.W. Serruys, Ed., *Handbook of Coronary Stents*, 4th ed. Informa Healthcare, November 2001. (Cited on page 199.)
- [124] B. K. Lal, E. A. Kaperonis, S. Cuadra, I. Kapadia, and R. W. H. II, "Patterns of in-stent restenosis after carotid artery stenting: Classification and implications for long-term outcome," *Journal of Vascular Surgery*, vol. 46, no. 5, pp. 833 – 840, 2007. (Cited on page 200.)
- [125] Cordis "PRECISE Nitinol Stent System", <http://www.cordislabeling.com>. (Cited on page 200.)
- [126] E. Chow, Y. Ouyang, B. Beier, W. Chappell, and P. Irazoqui, "Evaluation of cardiovascular stents as antennas for implantable wireless applications," *Microwave Theory and Techniques, IEEE Transactions on*, vol. 57, no. 10, pp. 2523 –2532, oct. 2009. (Cited on pages 200 and 202.)
- [127] L. Shedden, S. Kennedy, R. Wadsworth, and P. Connolly, "Towards a self-reporting coronary artery stent–measuring neointimal growth associated with in-stent restenosis using electrical impedance techniques," *Biosensors and Bioelectronics*, vol. 26, no. 2, pp. 661–666, 2010. [Online]. Available: <http://eprints.gla.ac.uk/47386/> (Cited on page 200.)
- [128] Boston Scientific "Carotid WALLSTENT", www.bostonscientific.com. (Cited on page 200.)

PUBLICATIONS

JOURNAL PAPERS:

1. Occhiuzzi C., Marrocco G., "RFID Technology for Neurosciences: Feasibility of Limbs Monitoring in Sleep Diseases", *IEEE Trans. on Information Technology in Biomedicine*, Vol. 14, No. 1, January 2010
2. Occhiuzzi C., Cippitelli S., Marrocco G., "Modeling, Design and Experimentation of Wearable RFID Sensor Tags", *IEEE Trans. on Antennas & Propagation*, Vol. 58, N.8, pp.2490-2498, August 2010.
3. Caizzone S., Occhiuzzi C., Marrocco G., "Temperature Sensing by Multi-Chip RFID Antenna Integrating Shape-Memory Alloys" *IEEE Trans. on Antennas & Propagation*, Vol.59, N.7, pp. 2488-2494, July 2011
4. Occhiuzzi, C.; Rida, A.; Marrocco, G.; Tentzeris, M.; , "RFID Passive Gas Sensor Integrating Carbon Nanotubes," *Microwave Theory and Techniques, IEEE Transactions on* , vol.59, no.10, pp.2674-2684, Oct. 2011
5. Occhiuzzi, C.; Paggi, C.; Marrocco, G.; , "Passive RFID Strain-Sensor Based on Meander-Line Antennas," *Antennas and Propagation, IEEE Transactions on* , to appear
6. Manzari S., Occhiuzzi S., Marrocco G. , "Feasibility of Body-centric Passive RFID Systems by Using Textile Tags", *IEEE Antennas and Propagation Magazine*, to appear
7. Occhiuzzi C., Contri G., Marrocco G., "Design of Implanted Passive RFID Tags for Sensing the Human Body", Submitted to *IEEE Transaction on Antennas and Propagation*

BOOK

1. Marrocco G., Occhiuzzi C., Amato F., "Sensor-Oriented Passive RFID", Chapter at the Book: The Internet of Things 2010, Part 4, pp. 273-282, Springer Verlag 2010

INTERNATIONAL CONFERENCES

1. C. Occhiuzzi, C. Calabrese and G. Marrocco, "Body-matched Slot Antennas for RadioFrequency Identification", Proceedings of XXIX General Assembly of the International Union of Radio Science (URSI), July 2008
2. C. Occhiuzzi, G. Marrocco, "RFID Technology for the Neuroscience: Feasibility of Sleep Disease Monitoring", Proceedings of 3rd European Conference on Antennas and Propagation EuCAP 2009, Berlin, Germany.
3. C. Occhiuzzi, G. Marrocco, "RFID detection of Human Body Movements ", Proceedings of European Microwave Week EUMW 2009, Rome
4. Occhiuzzi C., Marrocco G., "Sensing the human body by implanted RFID tags" Proc. of the 2010 EUCAP, pp.1-5, Barcelona, Spain, April 2010 **Honorable Mention Student Contest**
5. C. Occhiuzzi, G. Marrocco, "Wearable and implantable RFIDs for Human-body Sensing ", Proc. of the 2010 RFIDay, Tampere, Finland, April 2010
6. Occhiuzzi C., Marrocco G., "Pervasive body sensing: Implanted RFID tags for vascular monitoring" Proc. of the 2010 IEEE-APS-URSI Symposium, pp. 1-4, Toronto, ON, July 2010
7. Caizzzone S., Occhiuzzi C., Marrocco G., "RFID Radio-Sensors Integrating Shape-Memory Alloys", Proc. of the 2010 IEEE-APS-URSI Symposium, pp. 1-4, Toronto, ON, July 2010

8. Occhiuzzi C., Marrocco G., "Pervasive body sensing: Implanted RFID tags for vascular monitoring" Proc. of the 2010 RINEM, Benevento, September 2010
9. Caizzone S., Occhiuzzi C., Marrocco G., "RFID Radio-Sensors Integrating Shape-Memory Alloys", Proc. of the 2010 RINEM, Benevento, September 2010
10. C. Occhiuzzi, G. Marrocco, "Human Body Sensing: a Pervasive Approach by Implanted RFID Tags", Proc. of the 2010 ISABEL, Rome, November 2010
11. C. Occhiuzzi, A. Rida, G. Marrocco, M. Tetzzeris, "CNT-based RFID Passive Gas Sensor", Proc. of the 2011 IMS, Baltimore, MD, June 2011
12. S. Manzari, C. Occhiuzzi, G. Marrocco, "Reading Range of Wearable Textile RFID Tags in Real Configurations", Proc. of the 2011 EUCAP, Rome, Italy, April 2011
13. G. Contri, C. Occhiuzzi, G. Marrocco, "STENTag for passive vascular monitoring", Proc. of the 2011 EUCAP, Rome, Italy, April 2011
14. Caizzone S., Occhiuzzi C., Marrocco G., "RFID Thermal Seal: Radio-Sensor Integrating Shape-Memory Alloys", Proc. of the 2011 EUCAP, Rome, Italy, April 2011
15. C. Occhiuzzi, C. Paggi, G. Marrocco, "RFID Tag Antenna for Passive Strain Sensing", Proc. of the 2011 EUCAP, Rome, Italy, April 2011
16. C. Occhiuzzi, A. Rida, G. Marrocco, M. Tetzzeris, "Passive Ammonia Sensor: RFID Tag Integrating Carbon Nanotubes", Proc. of the 2011 AP-S, Spokane, WA, July 2011
17. S. Manzari, C. Occhiuzzi, G. Marrocco, "Experimental Characterization of Bodycentric Passive RFID Systems", Proc. of the 2011 AP-S, Spokane, WA, July 2011
18. G. Contri, C. Occhiuzzi, G. Marrocco, "Design of a Passive RFID Sensor for Vascular Monitoring", Proc. of the 2011 AP-S, Spokane, WA, July 2011

19. C.Occhiuzzi, C. Paggi, G.Marrocco, "Modeling and experimentation of an RFID Tag Antenna for Passive Strain Sensing" Proc. of the 2011 AP-S, Spokane, WA, July 2011
20. C. Occhiuzzi, G. Contri, G. Marrocco, "Implanted RFID Tags for Vascular Monitoring", Proc.of XXX URSI-GASS 2011, Istanbul, August 2011
21. S.Manzari, C.Occhiuzzi, G.Marrocco, "Body-centric RFID Systems", Proc. of the 2011 ISABEL, Barcelona, November 2011

PATENTS

- RM2010A000146: RF Device for mechanical and thermal sensing
- RM2010A000153: Implantable device for biological ducts.

ACKNOWLEDGMENTS

I would like to thank all the Engineers that during the last three years worked with me on the ideas and the results described in this Thesis: Stefano Cippitelli, Stefano Caizzone, Sabina Manzari, Corrado Paggi and Giordano Contri.

Moreover, many thanks to Prof. Fernando Bardati, Prof. Piero Tognolatti, Prof. Emidio Di Giampaolo, Prof. Giorgio Lovisolo and Prof. Manos Tentzeris for the suggestions, the valuable discussions and the help.

Finally, I am extremely thankful to my Advisor Prof. Gaetano Marrocco, for his important scientific and human support. He made my PhD experience productive and stimulating.